

# Three-Dimensional Optical Characterization of Heterogeneous Polymer Systems

A Thesis  
Presented to  
The Academic Faculty

by

Zhi Li

In Partial Fulfillment  
of the Requirements for the Degree  
Master of Science

Georgia Institute of Technology

May 2004

# Three-Dimensional Optical Characterization of Heterogeneous Polymer Systems

Approved by:

Dr. Robert J. Samuels, Advisor

Dr. Fred Cook

Dr. Rosario Gerhardt

May 13, 2004

## ACKNOWLEDGEMENTS

I would like to thanks Dr. Robert Samuels for the opportunity to study under him. Also, I thank him for the enormous amount of time, energy and thought he spent guiding me in my endeavors over the past two years;

I also would like to thank Dr. Rosario Gerhardt and Dr. Fred Cook for reading my thesis and for discussions of matters related to the thesis;

Much credit goes to Dr. Tao Liu for the development on the IRIA method;

Special thanks to Dr. Randy Pepper and Dr. Rosario Gerhardt's group for the sample fabrications;

I thank Dr. Haskell Beckham, Dr. Sankar Nair and Ms. Marilyn L. Minus for the equipments of FTIR and X-ray diffraction;

My deep appreciation to my husband Ziyang Wang for inspirations, discussion and true love;

Thanks my parents and Dr. Xuming Xie for their trust and encouragement.

## TABLE OF CONTENTS

Acknowledgements	iii
List of Tables	x
List of Figures	xii
Summary	xvi
CHAPTER I. INTRODUCTION	1
<b>PART A. OPTICAL CHARACTERISTICS OF STRETCHED ISOTACTIC POLYPROPYLENE WITH CARBON BLACK FILMS</b>	<b>4</b>
CHAPTER II. LITERATURE REVIEW AND PROBLEM DESCRIPTION	5
2.1 LITERATURE REVIEW	5
2.1.1 Percolation Threshold	5
2.1.2 Morphology	7
2.1.3 Crystallinity	9
2.1.4 Crystal Forms	13
2.1.5 Mechanical Properties	15
2.2 PROBLEM DESCRIPTION	16
CHAPTER III. TECHNIQUES AND THEORIES	18
3.1 OVERVIEW OF THREE-DIMENSIONAL STRUCTURE OF IPP-CB FILM	18
3.1.1 Three Principal Directions	18
3.1.2 Axiality	19
3.1.3 Hermans' orientation function	20
3.2 NONDESTRUCTIVE OPTICAL TECHNIQUES	21
3.2.1 Complex Refractive Index and Optical Waveguide Coupler	21
3.2.1.1 Complex Refractive Index	21

3.2.1.1.1 Definition	21
3.2.1.1.2 Importance	24
3.2.1.1.3 Optical Characteristics of Isotactic Polypropylene	25
3.2.1.1.4 Optical Constants of Carbon Black	26
3.2.1.2 Optical Waveguide Coupling Methods	28
3.2.1.2.1 Three-Dimensional Optical Measurement Concept	28
3.2.1.2.2 The Knee Method	31
3.2.1.2.3 The IRIA Method	34
3.2.1.2.4 Other Optical Constant Measurement Methods	37
3.2.2 Fourier Transform Infrared (FTIR) Spectroscopy	39
3.2.2.1 Crystalline and Average Band	39
3.2.2.2 Infrared Dichroism	41
3.2.2.3 Rolling Baseline	46
3.2.3 X-ray	48
3.2.3.1 $2\theta$	49
3.2.3.2 Crystal Forms	51
3.2.3.3 Crystallinity	55
3.2.3.4 The Orientation Function	57
CHAPTER IV. EXPERIMENT	61
4.1 SAMPLE FABRICATION AND MOUNT	61
4.1.1 Materials	61
4.1.2 Sample Fabrication	61
4.1.2.1 Casting Conditions	61
4.1.2.2 Drawing Conditions	62
4.1.3 Sample Mount	63

4.2 STRATEGY	64
4.2.1 Level I – IPP and CB Mixture	64
4.2.2 Level II – Crystalline and Noncrystalline Phases of IPP	66
4.2.3 Level III – Crystal Phase of IPP	66
4.3 OPTICAL WAVEGUIDE	67
4.3.1 The Knee Method	67
4.3.2 The IRIA Method	67
4.4 FTIR	68
4.4.1 Unpolarized FTIR	68
4.4.2 Polarized FTIR	68
4.5 X-RAY	70
CHAPTER V. RESULTS AND DISCUSSION	71
5.1 LEVEL I – WAVEGUIDE MEASUREMENT RESULTS	71
5.1.1 Extinction Coefficient	74
5.1.2 Refractive Index	74
5.1.2.1 Axiality	74
5.1.2.2 Orientation	78
5.1.2.3 Crystallinity	78
5.2 LEVEL II—FTIR MEASUREMENT RESULTS	81
5.2.1 Effect of Carbon Black on the FTIR Spectra	81
5.2.2 Unpolarized FTIR	81
5.2.3 Polarized FTIR	84
5.2.3.1 Orientation Function	84
5.2.3.2 Rolling Baseline	89
5.3 LEVEL III—X-RAY MEASUREMENT RESULTS	91

5.3.1 Crystal Form	91
5.3.2 2 $\theta$ value	98
5.3.3 Orientation Function	98
5.3.4 Crystallinity	103
5.4 RELATIONSHIP BETWEEN EACH LEVEL	104
5.4.1 Level I & Level II – Birefringence	104
5.4.2 Level II & Level III—Orientation Function of Crystalline Phase	106
5.4.3 Overall	111
CHAPTER VI. CONCLUSIONS	114
<b>Part B -- OPTICAL CHARACTERISTICS OF COMPRESSION MOLDED POLY (METHYL METHACRYLATE) WITH NANO INDIUM TIN OXIDE</b>	116
CHAPTER IIV. LITERATURE REVIEW AND PROBLEM DESCRIPTION	117
7.1 LITERATURE REVIEW OF PMMA-ITO(OR RELATED) SYSTEMS	117
7.1.1 PMMA-ITO Composites	117
7.1.2 ITO Filled Polymer Composites	119
7.1.3 Morphology of Polymer-Small Particle Composite	120
7.2 PROBLEM DESCRIPTION	123
CHAPTER IIIV. OPTICAL CONSTANTS OF PMMA AND ITO	124
8.1 OPTICAL CONSTANTS OF PMMA	124
8.1.1 General Description of PMMA	124
8.1.2 Refractive Index of PMMA	125
8.2 OPTICAL CONSTANTS OF ITO	127
8.2.1 General Description of ITO	127
8.2.2 Complex Refractive Index of ITO	128
CHAPTER IX. EXPERIMENTS	130

9.1 SAMPLE FABRICATION	130
9.2 OPTICAL MEASUREMENTS	130
9.3 MICROSCOPY STUDY	131
CHAPTER X. RESULTS AND DISCUSSIONS	132
10.1 OPTICAL CHARACTERIZATION	132
10.1.1 Refractive Index of PMMA	132
10.1.2 PMMA-ITO at 1550nm	135
10.1.3 PMMA-ITO at 543nm	138
10.2 MORPHOLOGY STUDY	151
CHAPTER XI. CONCLUSIONS	155
<b>PART C- SYSTEM OPERATIONS</b>	156
CHAPTER XII. EXPERIMENTAL UNCERTAINTY ANALYSIS: BOOTSTRAP IN IRIA	157
12.1 EXPERIMENTAL UNCERTAINTY ANALYSIS: BOOTSTRAP IN IRIA	157
12.1.1 History and Background of Bootstrap	157
12.1.2 Bootstrap in IRIA	160
12.1.3 Experimental Results and Discussions	161
12.1.4 Limitation of Bootstrap	161
12.2 THE TWO-LINE METHOD	165
12.2.1 The Two-Line Method Model	165
12.2.2 Modeling Calculation	166
12.2.3 Experimental Testing Results and Discussions	168
12.2.4 Limitation of the Two-Line method	168
12.3 THE BIG-AREA METHOD	170
12.3.1 The Big-Area Method Model	170



12.3.2 Experimental Results and Discussions	175
12.3.3 Limitation of the Big-Area Method	175
12.4 THE MODIFIED KNEE METHOD	178
12.4.1 The Modified Knee Method Modeling Calculation	178
12.4.2 Experimental Results and Discussions	185
12.4.3 The Limitation and Expectation of the Modified Knee Method	189
12.5 FUTURE MAP	190
CHAPTER XIII. OVERALL CONCLUSIONS	192
REFERENCES	194

## LIST OF TABLES

Table II-1	Literature percolation threshold values	6
Table II-2	Specification of the results of the degree of crystallinity <sup>15</sup>	13
Table III-1	The intrinsic refractive indices, $n_0$ , and birefringences, $\Delta_0$ , of IPP <sup>40, 41</sup>	26
Table III-2	The optical properties of Carbon Black	26
Table III-3	Crystalline and average bands of IPP in FTIR spectrum	39
Table III-4	The transition moment angles of 988cm-1 and 973cm-1 band of IPP <sup>76</sup>	45
Table III-5	Crystallographic data for isotactic polypropylene <sup>85</sup>	50
Table IV-1	The cast film thickness and the target draw ratio	62
Table V-1	The optical measurement results of IPP and IPP-CB samples	73
Table V-2	The average refractive index and the crystallinity of IPP and IPP CB films	77
Table V-3	The ratio of the peak height of 998 and 973 cm-1 of the IPP-CB sample measured by unpolarized FTIR	83
Table V-4	The results of dichroism calculations	87
Table V-5	The 2 $\theta$ values of 110 and 040 peaks	99
Table V-6	Orientation functions of c-axis calculated from x-ray diffraction of IPP and IPP-CB samples	103
Table V-7	Orientation functions of c-axis calculated from x-ray diffraction of IPP and IPP-CB samples after correction	113
Table VIII-1	Literatures on optical constants of ITO	129
Table X-1	Refractive index of PMMA	133
Table X-2	The refractive index and the extinction coefficients of PMMA-ITO samples change with ITO concentration	150
Table XII-1	The fitted results of the model by IRIA method	164

Table XII-2	The fitting results of PMMA-0.1 PHR ITO samples by the conventional IRIA method and the Two-Line Method	168
Table XII-3	The fitted results of PAN-SWNT (60/40) cast film by conventional and Big-Area IRIA methods	177
Table XII-4	The refractive indices of unstretched IPP-CB samples by different methods	186

## LIST OF FIGURES

Figure II-1	The TEM micrographs of an ultra thin section of 10 wt % N660-filled PP stained with RuO <sub>4</sub> vapor <sup>17</sup>	8
Figure II-2	Effect of carbon black structure on crystallinity of polypropylene in IPP-2.5% CB types <sup>2</sup>	10
Figure III-1	Definition of the three principal directions	19
Figure III-2	The schematic drawing of light refraction on the surface of two media	23
Figure III-3	The schematic pictures of MGT and EMA (shadowed: fillers; black: matrix) <sup>34</sup>	23
Figure III-4	Two polarizations	30
Figure III-5	The 0 degree and 90 degree setups for optical measurement	30
Figure III-6	Change of reflected intensity with incident angle <sup>50</sup>	33
Figure III-7	The schematic structure of the Metricon PC 2010 waveguide coupler <sup>50</sup>	33
Figure III-8	The schematic structure of the IRIA waveguide method <sup>8, 53</sup>	35
Figure III-9	The two polarization setups of FTIR measurement	42
Figure III-10	Infrared dichroism of cast uniaxially oriented polypropylene film <sup>31</sup>	42
Figure III-11	The relationship of transition moment angle and orientation angle <sup>31</sup>	44
Figure III-12	The rolling baseline in FTIR <sup>61</sup>	48
Figure III-13	Schematic picture of normal incident x-ray diffraction <sup>84</sup>	49
Figure III-14	Schematic draw of x-ray diffraction pattern of IPP fiber <sup>31</sup>	50
Figure III-15	X-ray diffraction intensity of three crystal forms for IPP <sup>91</sup>	53
Figure III-16	The x-ray diffraction intensity pattern of the IPP sample quenched at different temperature	54
Figure III-17	X-ray diffraction intensity pattern of 90% crystallinity IPP and amorphous IPP <sup>91</sup>	56

Figure III-18	Effect of isotactic polypropylene film extension on the wide-angle x-ray diffraction pattern <sup>31</sup>	58
Figure III-19	Typical 040 azimuthal intensity distribution scan from oriented isotactic polypropylene <sup>31</sup>	59
Figure IV-1	The schematic draw of the sample mounting	63
Figure IV-2	Strategy of the experiment procedure	65
Figure IV-3	The setup of unpolarized and polarized FTIR measurements	69
Figure V-1	An example of the IRIA fitting of IPP-CB samples (The example is IPP-1% CB 3X film, measured at 90° TE polarization @543nm)	72
Figure V-2	The extinction coefficients of IPP-CB samples measured by the IRIA method	75
Figure V-3	The refractive index results of IPP and IPP-CB samples	76
Figure V-4	The crystallinity of IPP and IPP-CB films changes with draw ratio	79
Figure V-5	The IRIA spectra of the IPP and IPP-2% CB unstretched samples	83
Figure V-6	The polarized FTIR spectra of IPP 5X sample at marked 0, -5 and +5 degrees	85
Figure V-7	The orientation functions of IPP and IPP-CB samples calculated from polarized FTIR results	88
Figure V-8	The rolling baselines of the IPP samples	90
Figure V-9	The diffraction images of IPP and IPP-CB samples	93
Figure V-10	The diffraction intensity curves of IPP and IPP-CB samples	94
Figure V-11	The diffraction intensity curves of unstretched IPP and IPP-CB samples	97
Figure V-12	The example of peak fitting (the sample is IPP 3X draw)	99
Figure V-13	The azimuthal curve of (110) plane of IPP films with different draw ratios	100
Figure V-14	The azimuthal curve of IPP 5X film (110) plane	102
Figure V-15	Compare the birefringence values measured by the	105

	waveguide methods and calculated from polarized FTIR results.	
Figure V-16	The orientation function of crystalline phase of IPP measured by FTIR and X-ray diffraction	107
Figure V-17	The linear fit of the orientation function of crystalline phase from X-ray against $(D-1)/(D+2)$	108
Figure V-18	The orientation function of each phase before and after correction	109
Figure V-19	The birefringence results from different method	112
Figure IIV-1	Percolation curves of PMMA composites with nano-sized ITO (31 nm) and coarse ITO ( $3.5\mu\text{m}$ ) <sup>98</sup>	118
Figure VII-2	(a) Schematic showing compaction of polymeric particles with attendant smaller particles of metal. (b) Photo micrograph of 7 volume percent of nickel ( $4-7\mu$ ) in polyvinyl chloride (400X) <sup>100</sup>	121
Figure VII-3	(a) Model morphology given by Cahn's approach: a-1. Two-dimensional cut; a-2. Three-dimensional image. (b) Model morphology given by extending Cahn's approach: b-1. Two-dimensional cut; b-2. Three-dimensional image <sup>102</sup> .	122
Figure VIII-1	Change in the refractive index of PMMA change with wavelength	126
Figure X-1	IRIA fitting (TE) of the pure PMMA sample (fitted results: $n=1.490$ ; $k=0$ )	133
Figure X-2	The reflected intensity curves obtained at different examination points of the PMMA sample at 543nm	134
Figure X-3	Refractive index of PMMA - nano ITO samples at 1550 nm as a function of ITO concentration	136
Figure X-4	IRIA fitting of the PMMA-10PHR ITO sample for TE polarization	138
Figure X-5	The reflectance curves of PMMA-ITO samples	139
Figure X-6	The slope of the reflectance curves	142
Figure X-7	The change in the refractive indices of the PMMA-ITO samples change with ITO concentrations.	144
Figure X-8	The curves of TE modeling calculation with $n=1.493$ airgap	148

=0.03 micron at 543 nm

Figure X-9	An example of finding k of the modified IRIA method (The Example is PMMA-5PHR ITO sample.)	149
Figure X-10	The extinction coefficient of PMMA- ITO sample changing with ITO concentration found by modified IRIA method	150
Figure X-11	The optical microscopy pictures of PMMA-ITO samples (10X) (scale bar = 50 microns)	152
Figure X-12	The SEM pictures of 10 PHR PMMA-ITO samples	153
Figure X-13.	Schematic drawing of the possible structure of PMMA caused the humps in reflected intensity curves.	154
Figure XII-1	The schematic drawing of the Bootstrap procedure <sup>134</sup>	159
Figure XII-2	The fitted curves of the model with relative error	164
Figure XII-3	Modeling testing of Two-Line method	167
Figure XII-4	The experimental fitting curves of PMMA-0.1 phr ITO with the conventional IRIA method and the Two-Line method	169
Figure XII-5	The PEDOT IRIA fitted curve (blue) and IRIA modeling calculated curve with reference complex refractive index value.	171
Figure XII-6	Modeling test of the Big-Area Method	174
Figure XII-7	The fitted curves of PAN-SWNT (60/40) cast film by conventional and Big-Area IRIA methods	176
Figure XII-8	The modeling calculation of the knee positions and biggest slope change positions with different extinction coefficients	179
Figure XII-9	The TE modeling calculation of the modified knee method	182
Figure XII-10	The TM modeling calculation of the modified knee method	183
Figure XII-11	The intensity, slope and differential slope changing with $\beta$ of IPP-2% CB TE intensity	187
Figure XII-12	Future map of the IRIA method	191

## SUMMARY

Nanoparticle filled polymer systems have multiphase structure and they are optical absorbing, therefore it is particularly hard to measure the optical characteristics of such materials. However, knowledge of the optical characteristics is very important for understanding the process-property behavior of these systems.

The purposes of the present research are to nondestructively identify the three-dimensional optical characteristics of heterogeneous polymer systems, such as stretched isotactic polypropylene with nano size carbon black pigment (IPP-CB) films and compression molded poly (methylmethacrylate) mixed with nano size indium tin oxide samples (PMMA-ITO), and to improve the accuracy of the optical waveguide methods.

The stretched IPP-CB film is an anisotropic uniformly distributed system. Three nondestructive optical methods: the optical waveguide coupling, Fourier Transform Infrared (FTIR) spectroscopy and x-ray diffraction were used to investigate the effect of the carbon black on the phase behavior and orientation of the films. It was found that the carbon black has little effect on the crystal form and crystallinity, but has a significant effect on the three-dimensional orientation behavior of the polypropylene in the IPP-CB systems. A multilevel procedure for obtaining structural information nondestructively was developed.

The PMMA-ITO sample is an unoriented and nonuniformly distributed system which has a grain structure. A unique Break Point Waveguide Method was proposed to deal



with this problem. It was found that both the refractive index and the extinction coefficient increased with ITO concentration and the samples were three dimensionally random.

Four methods were proposed to improve the accuracy of the waveguide methods. They are the Bootstrap Method, the Two-Line Method, the Big Area Method and the Modified Knee Method.

## CHAPTER I

### INTRODUCTION

The nano size particles have many unique properties, so they can be used as fillers to improve the properties of polymeric materials. The electrical conductivity<sup>1,2,3</sup>, mechanical properties<sup>3,4</sup> and rheology<sup>2,5</sup> etc. of the composites have been widely studied. As a consequence of this, the polymer-nano particle composites have many applications.<sup>6,7</sup> However, the structure of heterogeneous polymer systems is far from being fully understood. In the present research, the structural characteristics of the heterogeneous polymer nano-composite systems are investigated by nondestructive optical techniques.

For heterogeneous polymer systems, determination of the three-dimensional structural characteristics is particularly difficult. Such information is essential, however, if the behavior of these systems are to be understood and formalized. In the first two parts of this thesis (Part A and Part B), two heterogeneous polymer systems are experimentally investigated. In Part A, stretched isotactic polypropylene with nano size carbon black pigment (IPP-CB) film is measured. It is a uniformly mixed system. The effects of carbon black on the orientation, the crystallinity and the crystal form of isotactic polypropylene in the IPP-CB system were discussed. In Part B, the optical constants of a poorly mixed system, compression molded poly (methylmethacrylate)

mixed with nano size indium tin oxide sample (PMMA-ITO) was examined. In Part C, some methods were proposed to improve the accuracy of the Internal Refraction Intensity Analysis (IRIA) method,<sup>8</sup> which is a new technique for determining the three-dimensional complex refractive index measurement.

#### **Part A:**

Polypropylene carbon black system is a multiphase system. In this thesis, three nondestructive optical techniques: optical waveguide coupling, Fourier Transform Infrared spectroscopy (FTIR) and x-ray diffraction were used to study the stretched IPP-CB films with different carbon black concentrations (0%, 1% and 2%). The optical measurement results are used to reveal the effect of the carbon black on the crystallinity, crystal form and the orientation behavior of the isotactic polypropylene in the IPP-CB system.

The goals of Part A are:

1. To establish a routine including several nondestructive optical techniques for study of the 3-D characteristics of IPP-CB stretched films; and
2. To identify the orientation behavior of each phase in the IPP-CB system; and
3. To determine the effect of carbon black on the crystallinity and crystal structure of isotactic polypropylene in the IPP-CB system.

#### **Part B:**

The PMMA-ITO composite is a new system. It is found by optical and electron microscopy that the samples have a grain structure. Therefore a unique waveguide method, the Break Point Method, is proposed to deal with this problem in order to

obtain the refractive index and the extinction coefficient of the PMMA-ITO composites.

The goals of Part B are:

1. To identify the structure of PMMA-ITO composites; and
2. To develop an optical method to obtain the refractive index and the extinction coefficient of PMMA-ITO composites.

### **Part C:**

One of the main techniques used in the experimental part is the new IRIA waveguide method. During the research, some system operation analyses on the IRIA method were done and some useful methods were suggested:

1. The Bootstrap Method was introduced to the IRIA method to estimate the experimental uncertainty.
2. The Two-Line Method was proposed to eliminate the effect of airgap in the IRIA model fitting.
3. The Big Area Measurement was tried to expand the measurement angular region.
4. The Modified Knee Method was utilized to obtain high accurate refractive index values from moderately absorbing samples.

The goals of Part C are:

1. To understand more about the optical waveguide techniques; and
2. To develop new methods to improve the accuracy of the waveguide methods.

## **PART A**

### **OPTICAL CHARACTERISTICS OF STRETCHED ISOTACTIC POLYPROPYLENE WITH CARBON BLACK FILMS**

## CHAPTER II

### LITERATURE REVIEW AND PROBLEM DESCRIPTION

#### 2.1 LITERATURE REVIEW OF IPP-CB SYSTEM

Carbon black can be added into a polymer as a pigment or colorant, a reinforcing filler to improve dimensional stability, an ultraviolet light stabilizer and/or an antioxidant to prolong the lifetime of the polymer<sup>9</sup>. The polymer-carbon black composite materials have been widely used in cables, belts, automobile tires and hospital equipment.<sup>2</sup> In particular, the application of orientated isotactic polypropylene - carbon black composites in outdoor textiles such as geotextiles has been established for about 30 years<sup>2</sup>. This section will review and comment on some of the studies of the isotactic polypropylene filled with carbon black (IPP-CB) (or related) systems. The review will cover the percolation threshold, the morphology of IPP-CB, the effects of carbon black on the crystallinity and the crystal form of isotactic polypropylene and some mechanical properties of IPP-CB.

##### 2.1.1 Percolation Threshold

Currently, one of the attractive areas in the IPP-CB field is the determination of the percolation threshold of carbon black filled conducting polymer composites. A high level of electrical conductivity is obtained when a continuous conducting path is

formed at a critical concentration of conductive filler particles. This concentration is called the percolation threshold.<sup>9</sup> For the IPP-CB system, the percolation threshold values have been reported to range from 2 PHR (PHR: weight of filler/ weight of polymer) to 20 wt%<sup>10-15</sup>. Some of the values are listed in Table II-1.

**Table II-1.** Literature percolation threshold values

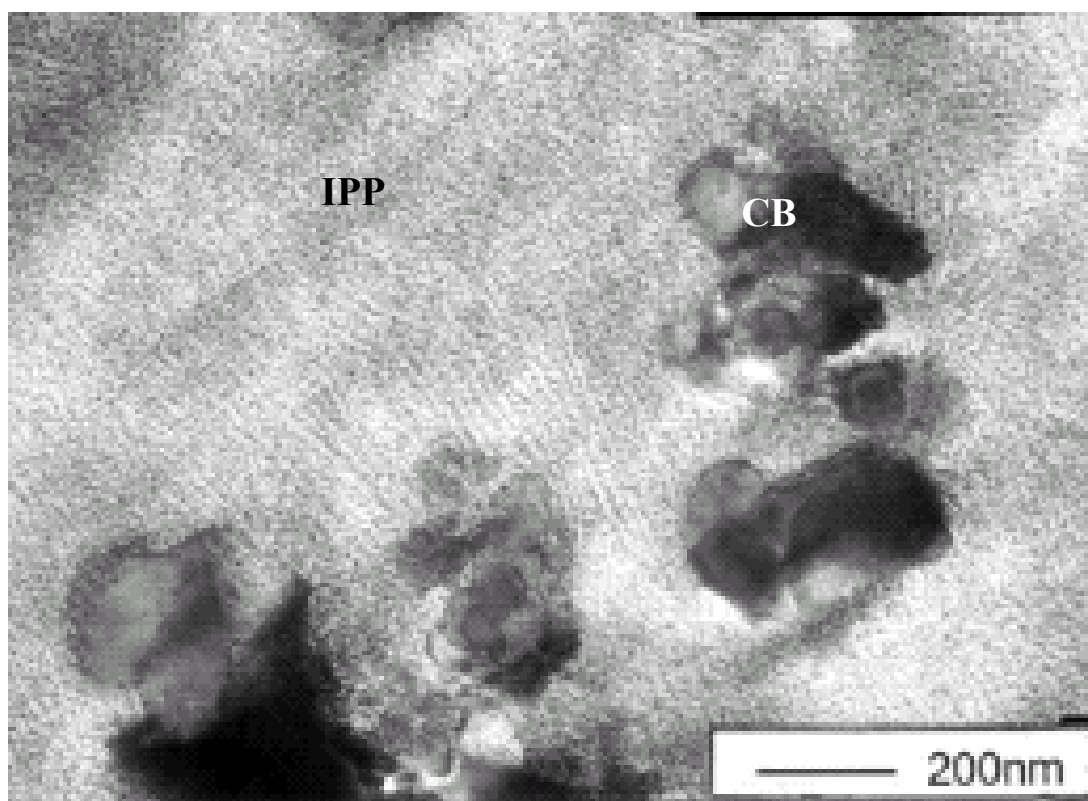
No.	Carbon black	Isotactic Polypropylene	Fabrication method	Percolation threshold	Reference
1	Ketjenblack EC	VC 15-15 P	Brabender Plastograph	2 PHR	10,11
2	VULCAN XC-72R	Tatren TF-411	Plasti-corder kneeding machine	6.2 wt%	12
3	Pearls 2000	From PEMEX, (Mw=141900, Mn=39200) a. pristine IPP b. recycled IPP	Brabender bambury type mixer	a. 15 wt% b. 10 wt%	13
4	Pearls 2000	Profax 6323	Haake Torque Rheometer with Roller Mixer	4 vol.%	14
5	a. Sakap 6 b. Carbex 330 c. Jas-220	Malen P type J-400	Formoplast 235/60 screw -injection molding machine	a. 20 wt% b. 20 wt% c. 10 wt%	15

The differences are understandable, because the percolation value depends strongly on the type of carbon black (structure, surface area, size, etc)<sup>9</sup>, polypropylene (molecular weight,<sup>13</sup> crystallinity,<sup>13, 16</sup> surface tension<sup>10, 11</sup>) and also the sample fabrication method<sup>3</sup>. Much more work is needed in this area before the fundamentals are fully understood.

### 2.1.2 Morphology of IPP-CB

The morphology of IPP-CB system was studied by Scanning Electron Microscopy (SEM), which shows that conducting carbon black is randomly distributed in the IPP matrix<sup>10, 11, 12 and 13</sup>. Since IPP is a semi-crystalline polymer, it is more important to determine the relationship between the carbon black and the crystalline and noncrystalline phases of isotactic polypropylene. Feng, et al. reported some Transmission Electron Microscopy (TEM) results which micrographs clearly showed this relationship<sup>17</sup>. They used a RuO<sub>4</sub> vapor-staining technique to dye the sample. The amorphous layers can absorb more RuO<sub>4</sub>, such that the amorphous layers and lamellae can be identified under TEM imaging.<sup>18, 19</sup> Figure II-1 is the TEM micrographs of an ultra thin section of 10 wt% N660-filled IPP stained with RuO<sub>4</sub> vapor. It provides the directly evidence of the distribution of CB in the IPP-CB system. In Figure II-1, the background is IPP which shows the amorphous layers and lamellae of IPP in black and white, respectively. The big blocks are the CB particles or aggregates. The thickness of the lamellae is much smaller than the dimensions of the CB particles, so the CB particles or aggregates can't disperse between the lamellas. All of the three carbons blacks (N660, V-XC72 and EC-300 J) used in their study showed the same morphology. The authors also mentioned that compared to the spherulite size (~100  $\mu\text{m}$ ) and the boundary dimensions between the spherulites (~4 nm), the CB is too large to locate between the spherulites, so it must be inside the spherulites. However, they didn't show any picture to prove this statement. There are no morphological studies on stretched IPP-CB composites.





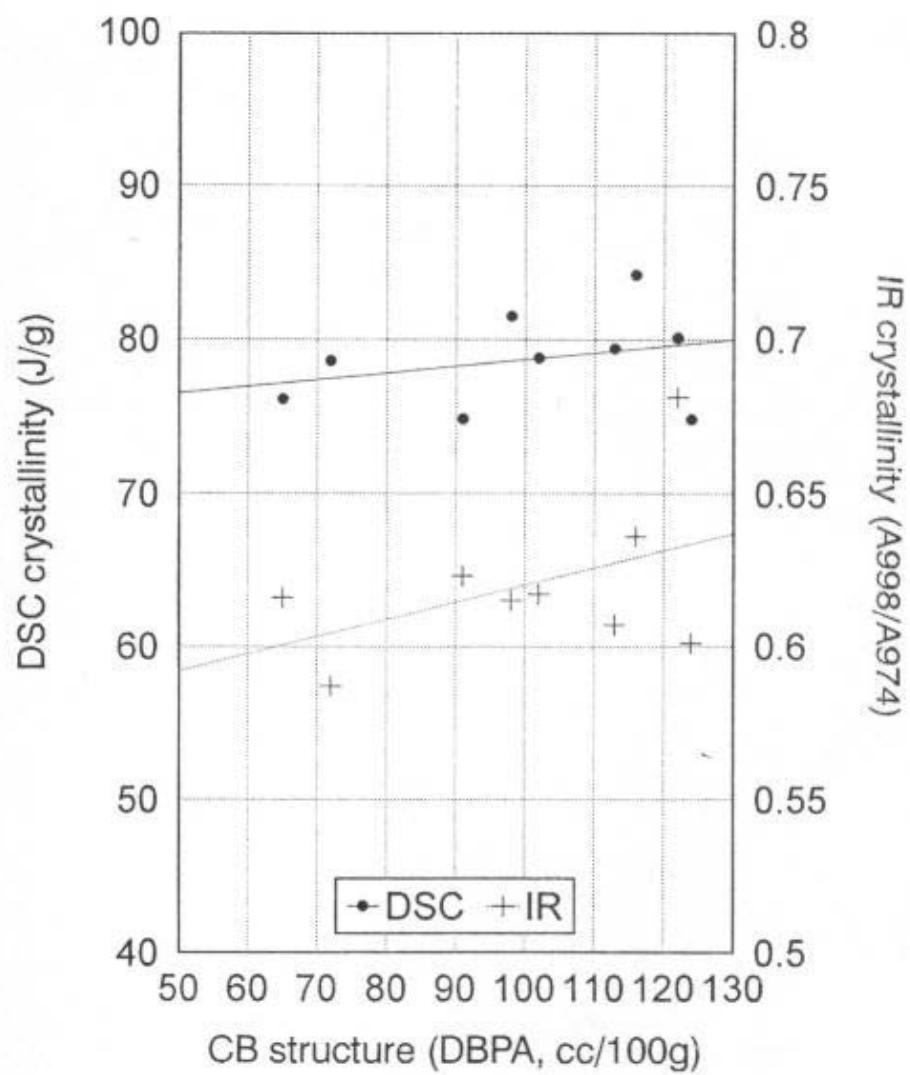
**Figure II-1.** The TEM micrographs of an ultra thin section of 10 wt % N660-filled PP stained with RuO<sub>4</sub> vapor<sup>17</sup>

### 2.1.3 Crystallinity

Horrocks et al. investigated the presence of carbon black (14 different carbon blacks were used, see details in Table 2 of reference 4) and variations in particle properties influenced the characteristics of the crystalline regions of IPP by differential scanning calorimetry (DSC) and FTIR<sup>2</sup>. Horrocks et al. found in the isotactic polypropylene-carbon black system, the crystallinity was affected by the carbon black particle size and the structure factor DBPA (dibutyl phthalate absorption) (Figure II-2). The DBPA is a standard parameter to describe the aggregate morphology of carbon black. The arrangement in the aggregates determines the bulkiness or so-called structure of the carbon black. The DBPA is measured by adding dibutyl phthalate until the void spaces in the carbon blacks are filled<sup>2</sup>. Horrocks et al. concluded that the crystallinity increased with increase in the CB structure factor DBPA. At 5% (w/w) carbon black concentration, crystallinity was lower than 2.5% (w/w) in all samples with the same carbon black structure. However, the points in Figure II-2 have considerable scatter and don't show an apparent increase with the DBPA. The author's conclusion is questionable. On the other hand, both FTIR and DSC have shortcomings. The FTIR crystallinity ratio is only a semi-quantitative method (see FTIR crystallinity ratio in 3.2.2.1) which cannot provide absolute crystallinity values. The crystallinity by DSC method was calculated by:

$$V_c = \frac{\Delta H_c}{\Delta H_c^0} \times 100\% \quad \text{Eq. II-1}$$

where  $\Delta H_c$  and  $\Delta H_c^0$  are the enthalpy of the sample and 100% crystal, respectively.



**Figure II-2.** Effect of carbon black structure on crystallinity of polypropylene in IPP-2.5% CB types<sup>2</sup>

Therefore the crystallinity from DSC depends strongly on the baseline adjustment method in the calculation of  $\Delta H_c$  and the value of  $\Delta H_c^0$  used. However, numerous values of  $\Delta H_c^0$  of IPP are reported in the literature (207 J/g<sup>20</sup>, 138 J/g<sup>21</sup>, and 236 J/g<sup>22</sup>). Koszkuł used DSC and wide-angle X-ray scattering (WAXS) to study the effect of carbon black (Sakap) on the crystallinity of IPP<sup>15</sup>. The results are shown in Table II-2 (Page 13). He concluded that high carbon black content in the composite causes an increase in degree of crystallinity, as determined by WAXS. The degree of crystallinity, however, determined by DSC, decreased. In his research, the crystallinity by DSC was also calculated by Eq. II-1:

$$V_c = \frac{\Delta H_c}{\Delta H_c^0} \times 100\% \quad \text{Eq. II-1}$$

This equation does not suit composites, especially when the components have comparable contents. In the reported research, the carbon black concentration went as high as 40%, and carbon black didn't crystallized when the isotactic polypropylene is crystallizing. If only the  $\Delta H_c^0$  of pure isotactic polypropylene is used to refer to  $\Delta H_c$ , the error of the crystallinity due to the weight percentage of the carbon black will be significant. However, in this article<sup>15</sup>, this is the method used to obtain the crystallinity. For composites with high carbon black content, the relative weight percentage of isotactic polypropylene is low. Therefore, lower enthalpy values were obtained and, hence, a lower degree of crystallinity. In the x-ray method, reflections are obtained from the crystalline structures of a composite. The author concluded that although carbon black did not give reflections from its crystalline structures, it caused an increase in the crystalline structures of a composite because small carbon black

particles can serve as nuclei of crystallization<sup>15</sup>.

There are several problems in this research:

1. Baseline: The baseline has a big effect of the results on both X-ray (see discussion of x-ray baseline in 3.2.3.3) and DSC. The author didn't show the curves and/or patterns of DSC or X-ray results, the calculation methods are not clear, especially for the baseline adjustment.
2.  $\Delta H_c^0$ : the author didn't clarify what value was used in the calculation of the crystallinity.
3. Using  $\Delta H_c^0$  of polypropylene as a reference: Indeed a simple method can correct the effect of CB: Since during the DSC measurement, the carbon black didn't crystallize, so the  $\Delta H_c$  of polypropylene can be corrected by the weight percentage of polypropylene:

$$V_c = \frac{\Delta H_{IPP,c}}{\Delta H_{IPP,c}^0} \times 100\% = \frac{\Delta H_{\text{sample},c} / W_{IPP}}{\Delta H_{IPP,c}^0} \times 100\% = \frac{\Delta H_{\text{sample},c} / (1 - W_{CB})}{\Delta H_{IPP,c}^0} \times 100\% \quad \text{Eq.II-2}$$

where  $W_{IPP}$  and  $W_{CB}$  are the weight percentage of polypropylene and carbon black, respectively.

The corrected results are also listed in Table II-2 in the "After correction" column.

The results show that the crystallinity didn't change significantly. The difference between the corrected DSC results and WAXS method may be caused by reason 1 and 2 discussed above.

4. WAXS: The author concluded that the crystallinity from x-ray increased with carbon black concentration, but the trend is not either dramatic or coherent.

**Table II-2.** Specification of the results of the degree of crystallinity<sup>15</sup>

No.	Type of sample	Average degree of crystallinity, %		
		DSC method		WAXS method
		Before correction	After correction*	
1	Polypropylene J -400	46.1	46.1	58.3
2	J -400 + 2% Sakap	47.4	48.4	60.2
3	J -400 + 5% Sakap	43.2	45.5	61.4
4	J -400 + 10% Sakap	38.5	43.7	60.9
5	J -400 + 20% Sakap	36.5	45.6	62.6
6	J -400 + 30% Sakap	32.8	47.6	64.7
7	J -400 + 40% Sakap	29.3	48.8	64.1

\*Corrected by Zhi Li based on the percentage of carbon black (Eq. II-2)

In other words, by adding CB into the system, it is hard to obtain quantitative results of crystallinity by DSC, FTIR or WAXS.

#### 2.1.4 Crystal Forms

Mucha et al. studied the effect of carbon black (Sakap 6) on the properties and kinetics of crystallization of isotactic polypropylene by DSC.<sup>23</sup> Polypropylene samples containing 2 – 30% weight fraction of carbon black were prepared by mixing the initial sample containing 40% carbon black. The analysis of melting, crystallization and kinetics of crystallization was carried out using DSC at seven stages whose aim was to melt and heat isothermally the filled samples of isotactic polypropylene. It was shown that carbon black filler caused dramatic changes of the rate of isotactic polypropylene crystallization. The carbon black was a nucleation center leading to crystal growth.<sup>24</sup> It also seems that carbon black as a filler leads to the nucleation of the  $\beta$  crystal form (see information of crystal forms of IPP in

3.2.3.2), which is not observed in pure IPP at the temperatures under study. Maximum efficiency in a change of the nucleation and crystallization rates for samples with a low content of carbon black is found. However, the change in DSC curves cannot provide adequate evidence of the presence of the  $\beta$  crystal form.<sup>25</sup> When Bhattacharyya et al. studied the IPP-SWNT (single wall carbon nanotube) composite system, they observed a similar change on the DSC curves, but WAXS indicated only the  $\alpha$  form was present in the composite.<sup>26</sup>

Therefore, compared to DSC, X-ray is a more reliable method to reveal the crystal form. For example, Broda used WAXS and small-angle X-ray scattering (SAXS) to study the nucleating ability of quinacridone pigment in isotactic polypropylene fibers<sup>27</sup>. He found that the content of different isotactic polypropylene crystal forms as well as their lamellar thickness depends on crystallization conditions, which were influenced by the fabrication parameters, such as extrusion temperature and take-up velocity. The fibers extruded at the low temperature of 210°C exhibited a crystalline structure formed almost exclusively from  $\alpha$  crystals. The fibers spun at the higher temperature of 250°C because of the higher cooling rate had a small mesophase content. At low take-up velocity in the presence of the quinacridone pigment, the structure with the high content of the  $\beta$  form is produced. But at high take-up velocity, the influence on the crystal form is hard to see. The pigment can also increase the crystallinity of isotactic polypropylene, but no difference is observed with changes of the take-up velocity<sup>27, 28, 29</sup>.

## 2. 1. 5 Mechanical Properties

Koszkul tested the mechanical properties of IPP-CB systems with three kinds of carbon black (No.5 in Table II-1)<sup>15</sup>. He found the tensile strength increased at low carbon black content (to 10%), whereas at higher content, it decreased substantially. An increase in the carbon black content of a composite also caused an increase in the modulus of elasticity, but a decrease in impact strength.<sup>15</sup>

Wu reported that the tensile strength of IPP-CB (No.4 in Table II-1) showed a small increase below 5 vol % CB, a general decreasing trend at higher concentration and the tensile elongation decreased with carbon black concentration<sup>14, 9</sup>.

Horrock et al. measured the tensile properties of IPP-CB with different CB particle size and structure DBPA<sup>2</sup>. They concluded the strength of tapes depended on both particle size and structure at 2.5% loading. Low particle sized blacks give the highest strength and higher structured blacks yield lower strength. On the effect of carbon black concentration, they found that at a constant particle size (20 nm), there is a significant drop in tenacity at the higher concentration 5%. However, this drop in tenacity is less than when higher structured carbon black are used. But all 2.5% and 5% CB loading samples have lower tenacity than pure polypropylene.

The discussions above didn't agree with each other. The problems could be the difference of carbon blacks. But they all missed a factor in their research, which was the experimental uncertainty. For mechanical property testing, however, it is important.



## 2.2 PROBLEM DESCRIPTION

Though some work has been done on the IPP-CB system, there are still several general problems.

First, the most common problem is that the properties of carbon black change dramatically with the type. Therefore it is hard to compare the results of one carbon black with another. The carbon blacks are different case by case.

Second, there little work reported on the optical characteristics. No research investigates the refractive index,  $n$ , and the extinction coefficient,  $k$ , (see  $n$  and  $k$  in 3.2.1.1) of the IPP-CB system, especially in the visible region. The reason is that the application of the regular optical constant measurement methods was forbidden by the highly optically absorbing filler, carbon black, the thickness and/or the rough surface of the sample. Though, some optical techniques, such as FTIR and x-ray, are used in the crystal study, they are only limited to unstretched samples in the literature studies.

Third, the effect of carbon black on the orientation behavior of IPP has not been studied, especially three dimensionally. It may be caused by the complicated multiphase structure of IPP-CB and a lack of experimental techniques.

Fourth, there is little reliable research which combines several nondestructive techniques or compares the results from different methods. In some research, the results were “confirmed” by some destructive techniques, such as DSC and electron microscopy. By doing this, the sample was destroyed, so the measurement can’t be repeated, and the results from different parts of sample may not be equivalent. If nondestructive methods are used, the sample can be measured at the same place with

different techniques, so that the results can be compared. Therefore nondestructive techniques are preferred.

Finally, when the data were reported, no uncertainty was provided, so sometimes it was hard to give a confident conclusion.

This thesis, attempts to avoid all of the above problems. Three nondestructive optical techniques are used to study the stretched IPP-CB systems. The research will not only study the effect on the crystallinity and crystal form, but also on the orientation changes of the isotactic polypropylene. It is a three-dimensionally multilevel investigation. The carbon black in this research is a nonconducting CB (Raven 1220 Ultra). However, as a novel way to explore the characteristics of IPP-CB systems, this routine is not limited to the IPP-nonconducting CB system. It is a model procedure for the characterization of other anisotropic well-mixed heterogeneous polymer systems, including IPP-conducting CB systems.

## CHAPTER III

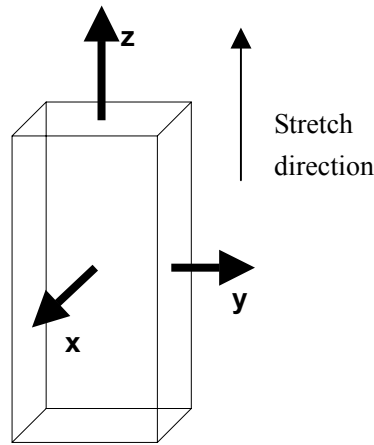
### TECHNIQUES AND THEORIES

In this chapter, first the general anisotropic structure of IPP-CB is described, and then the principals and application of the three nondestructive optical methods, optical waveguide coupler, Fourier Transform Infrared Spectroscopy (FTIR) and X-ray diffraction, used in the anisotropic system study are discussed.

#### 3.1 OVERVIEW OF THREE-DIMENSIONAL STRUCTURE OF IPP-CB FILM

##### 3.1.1 Three Principal Directions

A randomly oriented sample when stretched will become anisotropic. Anisotropic means the sample exhibit properties with different values when measured in different directions. Therefore in order to discuss the anisotropic system, it is important to define the principal directions. In this study the three principal directions are defined as shown in Figure III-1: the stretch direction is the z axis, and the y and x axes are perpendicular to z in the plane and through the plane, respectively.



**Figure III-1.** Definition of the three principal directions

### 3.1.2 Axiality

During the stretching, the sample is elongated along the z axis and shrinks in the y and x directions. As a result, the orientation of polymer chain is changed three dimensionally. The polymer chain tends to be aligned along the z axis and therefore the sample gets stronger along the z axis and weaker along the y and x directions. For a stretched sample, if the properties are the same in the y and x directions, it is called a uniaxial stretching; otherwise, it is called biaxial stretching. The axiality can be identified by comparing the optical properties, such as the refractive index (See refractive index in 3.2.1.1) along the axes (random:  $n_z = n_y = n_x$  ; uniaxial:  $n_z \neq n_y = n_x$ ; biaxial:  $n_z \neq n_y \neq n_x$  )and the birefringence (See birefringence in 3.2.1.1.2) between different planes of the sample.

### 3.1.3 Hermans' orientation function

The Hermans' orientation function is a useful parameter to describe the orientation degree of an anisotropic sample. The Hermans' orientation function is defined as<sup>30</sup>:

$$f = \frac{1}{2}(3 \langle \cos^2 \varphi \rangle - 1) \quad \text{Eq. III-1}$$

where  $\varphi$  is the average angle between the polymer chain axis and stretching direction.

When all the chains are perfectly oriented along the optical symmetry axis,  $f = 1$ . If the chains are oriented perfectly perpendicular to the optical symmetry axis,  $f = -1/2$ .

If the chain orientation is random, then  $f = 0$ .

In a multiphase system, the orientation function of each phase may not be the same. For semi-crystalline polymers, the relationship between the orientation functions of crystalline and non-crystalline phases is:

$$f_{ave} = V_c f_c + (1 - V_c) f_{nc} \quad \text{Eq. III-2}$$

Where  $f$  is the Hermans' orientation function,  $V_c$  is the crystallinity; the subscripts, ave, c and nc are average phase (overall of crystalline and non-crystalline phase), crystalline phase and non-crystalline phase, respectively<sup>31</sup>.

The orientation function can be calculated by birefringence (for single phase materials) (see 3.2.1.1.2), FTIR (see 3.2.2.2) or x-ray diffraction (crystalline phase only) (see 3.2.2.4).

## 3.2 NONDESTRUCTIVE OPTICAL TECHNIQUES

### 3.2.1 Complex Refractive Index and Optical Waveguide Coupler

#### 3.2.1.1 Complex Refractive Index

##### 3.2.1.1.1 Definition

The complex refractive index,  $n^*$ , is

$$n^* = \sqrt{\varepsilon} = n + ik \quad \text{Eq. III-3}$$

where  $\varepsilon$  is the complex dielectric constant of the medium,  $n$  is the refractive index and  $k$  is the extinction coefficient<sup>32</sup>.

The refractive index,  $n$ , is defined as the ratio of the speed of light in one medium (as a vacuum) to that in another medium. Light refraction is schematically shown in Figure III-2. The refractive index follows Snell's law<sup>33</sup>:

$$n_1 \sin(\theta_1) = n_2 \sin(\theta_2) \quad \text{Eq. III-4}$$

where  $n$  is the refractive index of the medium,  $\theta$  is the incident angle; the subscripts 1 and 2 indicate medium 1 and 2, respectively.

The extinction coefficient,  $k$ , is a measure of the rate of diminution of transmitted light via absorption and scattering for a medium<sup>32</sup>. When light travels through a solid sample, the ratio of transmitted and incident intensity is governed by<sup>32</sup>:

$$I_t = I_0 \exp(-4\pi\lambda kx) \quad \text{Eq. III-5}$$

where  $I_0$  and  $I_t$  are the intensity of incident light and transmitted light, respectively;  $\lambda$  is the wavelength;  $k$  is the extinction coefficient and  $x$  is the propagation distance.

There are some models dealing with the heterogeneous systems. The two most popular models are Maxwell-Garnett theory (MGT) and the effective medium

approximation (EMA). Schematics are shown in Figure III-3.

The main difference between these two models is the way in which the medium surrounds the grain. In the MGT model it is assumed that the medium surrounding the grains is one of the constituents of the mixture (for example, the one with the largest volume fraction), whereas in the EMA model the surrounding medium is assumed to be characterized by the effective properties of the inhomogeneous medium<sup>34</sup>. The equation of MGT is:

$$\epsilon_{\text{MGT}} = \epsilon_b + \epsilon_b \frac{3V_p(\epsilon_a - \epsilon_b)}{(1 - V_p)(\epsilon_a - \epsilon_b) + 3\epsilon_b} \quad \text{Eq. III-6}$$

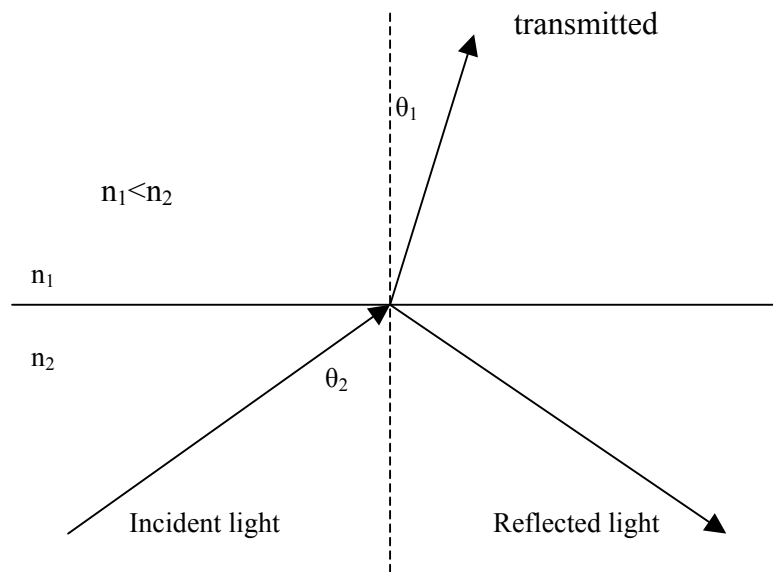
The equation of EMA is:

$$V_p \frac{\epsilon_a - \epsilon_{\text{EMA}}}{\epsilon_a + 2\epsilon_{\text{EMA}}} + (1 - V_p) \frac{\epsilon_b - \epsilon_{\text{EMA}}}{\epsilon_b + 2\epsilon_{\text{EMA}}} = 0 \quad \text{Eq. III-7}$$

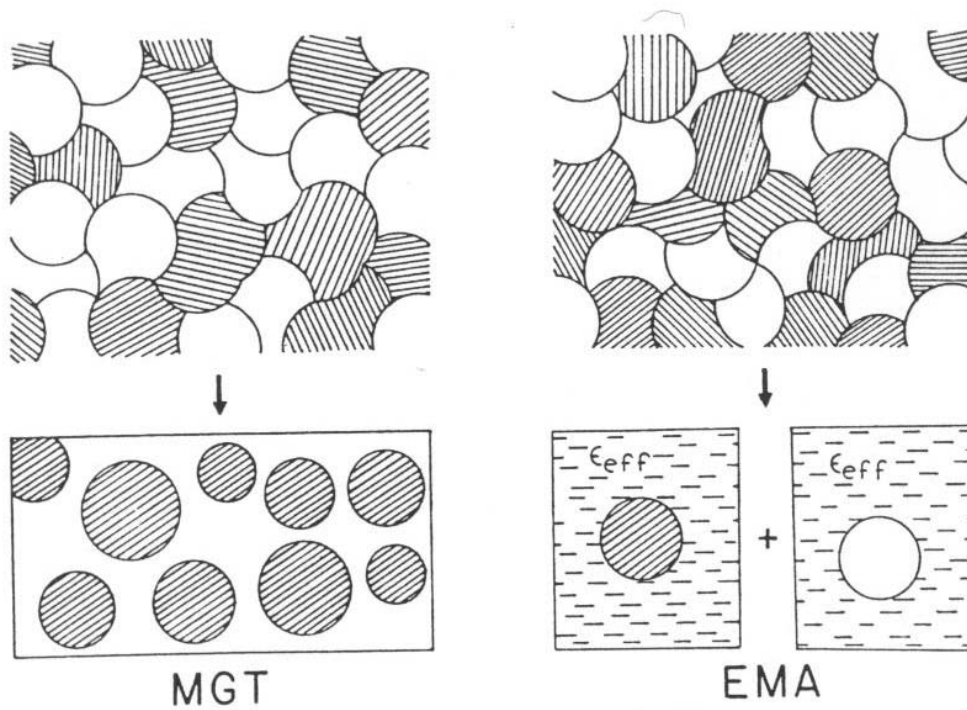
where  $\epsilon$  is the dielectric function, which [ $\epsilon = (n^*)^2$ ] and the subscripts a, b are for the matrix and grain, respectively. The  $\epsilon$ 's with subscripts MGT and EMA indicate the properties are calculated by the MGT and EMA models, respectively.  $V_p$  is the volume fraction of the grain.

Compared with MGT, the EMA model is a symmetric model, which treats the two components of the composites the same way.

The models are limited to a system with small filler particle size and good particle dispersion. They fit some of the experimental results of low concentration filler systems.<sup>35, 36, 37</sup>



**Figure III-2.** Schematic drawing of light refraction at the surface of two media



**Figure III-3.** The schematic pictures of the MGT and the EMA models (shadowed: fillers; black: matrix)<sup>34</sup>



### 3.2.1.1.2 Importance

The complex refractive index not only presents the optical constant of a medium, but can also be used to identify the structure of the sample, such as crystallinity, axiality, and orientation function, etc.

Since in the crystalline phase the polymer chain packs tighter than in the noncrystalline phase, the density of the crystalline phase is higher than noncrystalline phase. Therefore the system density is generally used to calculate the crystallinity. On the other hand, the refractive index,  $n$ , also changes with density<sup>32</sup>, so the refractive index can be described as a function of crystallinity.

The axiality can be directly identified from the relationship between the complex refractive index values ( $n_y^*$  and  $n_x^*$ ) or from the birefringence. The birefringence,  $\Delta$ , is defined as the difference between the refractive indices of two principal directions:

$$\begin{aligned}\Delta_{zx} &= n_z - n_x \\ \Delta_{zy} &= n_z - n_y \\ \Delta_{yx} &= n_y - n_x\end{aligned}\quad \text{Eq. III-8}$$

For a sample oriented along  $z$  axis, if  $\Delta_{yx} = 0$ , the sample is uniaxial, otherwise, it is biaxial.

For single-phase materials, the birefringence can also be used to calculate the orientation function.<sup>30</sup> The equation is:

$$f = \frac{\Delta}{\Delta^0} \quad \text{Eq. III-9}$$

where the  $\Delta^0$  is the intrinsic birefringence, which is the birefringence value for a sample which is perfectly oriented along the  $z$  axis .

However, it must be noticed that for a multiphase system it is more complicated than

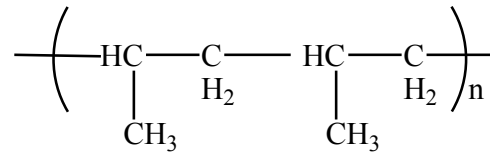
this. Samuels provided the function for semicrystalline polymer system<sup>38</sup>:

$$\Delta zy = V_c f_c \Delta_c^0 + (1 - V_c) f_{nc} \Delta_{nc}^0 \quad \text{Eq.III-10}$$

where subscripts c and nc indicate crystalline and noncrystalline phases, respectively.

### 3.2.1.1.3 Optical Characteristics Of Isotactic Polypropylene

The chemical structure of IPP is:



IPP is a semi-crystalline polymer. In this part, the characteristics obtained from the refractive index are reviewed. The measurement methods of the orientation, crystal form, etc. by FTIR and x-ray diffraction will be discussed in 3.2.2 and 3.2.3.

The IPP films are transparent, so the extinction coefficient, k, value is not significant. Based on the refractive index, the axiality (see axiality in 3.1.2), crystallinity and birefringence of isotactic polypropylene can be obtained.

As mentioned in 3.2.1.1.2, the crystallinity of the IPP sample can be calculated from the refractive index,  $n$ , <sup>39</sup>(Eq. III-11):

$$V_c = \frac{\bar{n} - n_{nc}}{n_c - n_{nc}} = \frac{(n_x + n_y + n_z)/3 - 1.4707}{1.5245 - 1.4707} \quad \text{Eq. III-11}$$

Samuels obtained the intrinsic refractive indices parallel and perpendicular to the orientation directions and the intrinsic birefringences of the crystalline and noncrystalline phases of IPP<sup>40, 41</sup>(Table III-1).

**Table III-1.** The intrinsic refractive indices,  $n^0$ , and birefringences,  $\Delta^0$ , of IPP<sup>40, 41</sup>

	Intrinsic Refractive index		Intrinsic Birefringence
	Parallel	Perpendicular	
Crystal	1.5436	1.5145	0.0291
Non-crystal	1.5151	1.4551	0.0600

For a given IPP sample with certain crystallinity,  $V_c$ , the intrinsic birefringences at parallel and perpendicular directions are<sup>40, 41</sup>:

$$n_{//}^0 = V_c n_{//c}^0 + (1 - V_c) n_{//nc}^0 \quad \text{Eq. III-12}$$

$$n_{\perp}^0 = V_c n_{\perp c}^0 + (1 - V_c) n_{\perp nc}^0 \quad \text{Eq. III-13}$$

where subscripts  $//$  and  $\perp$  indicate parallel and perpendicular directions to the stretch direction.

#### 3.2.1.1.4 Optical Constants of Carbon Black

The properties of CB depend strongly on the type of carbon black used.

The complex refractive indices reported by different references vary widely. In Table III-2, some of reported values are listed. Because, in this study, a green laser (543nm) was used, in Table III-2 only the experimental results near 543nm are shown.

**Table III-2.** The optical constants of Carbon Black

Wavelength (nm)	n	k	Reference	Carbon Black
435.8-806.5	1.57	0.56	42	soot
533	2.648	1.383	43	pyrolytic graphite
533	2.331	0.981	43	amorphous carbon
533	1.496	0.352	44	propane soot
539	$n_e=1.36$ $n_o=2.67^*$	$k_o=1.34^*$	44	amorphous carbon
540	1.96692	0.176	45	amorphous carbon
540	1.73	0.58	46	soot

\* Subscripts o and e indicate ordinary and extraordinary rays, respectively.

The wide variation in the measured complex refractive indices most likely comes from the amount of other hydrocarbons contained in the particles<sup>47</sup>. Therefore the optical constant of other carbon blacks cannot be used to in this study.

On the other hand, the measurement techniques, such as photoemission and Electron-Energy-Loss Spectroscopy (EELS), used to measure the optical constants of carbon black are based on the Kramers-Kronig (KK) transform. The general dispersion relation between the refractive index and the extinction coefficient of the KK transform are given by

$$n_2(\omega') = n_\infty + \frac{2}{\pi} P \int_0^{+\infty} \frac{\omega k(\omega)}{\omega'^2 - \omega^2} d\omega \quad \text{Eq. III-14}$$

$$k_2(\omega') = -\frac{2\omega}{\pi} P \int_0^{+\infty} \frac{n_2(\omega)}{\omega'^2 - \omega^2} d\omega \quad \text{Eq. III-15}$$

where  $n_2$  and  $k_2$  are the refractive index and extinction coefficient of the medium, respectively;  $P$  is the principal value of the integral and  $\omega$  is the angular frequency;  $n_\infty$  is the refractive index at infinite frequency.<sup>48</sup>

Eq. III-14 and Eq. III-15 show that the KK transform needs to know or at least to assume the refractive index at infinite frequency and measure from 0 to infinite frequency. However, the real  $n_\infty$  is difficult to obtain and with the current measurement methods it is impossible to cover all frequencies. So these two factors will introduce errors in the results. Especially, it is rather unreliable for the extinction coefficient values below 0.1<sup>49</sup> or higher than 0.5<sup>48</sup>.

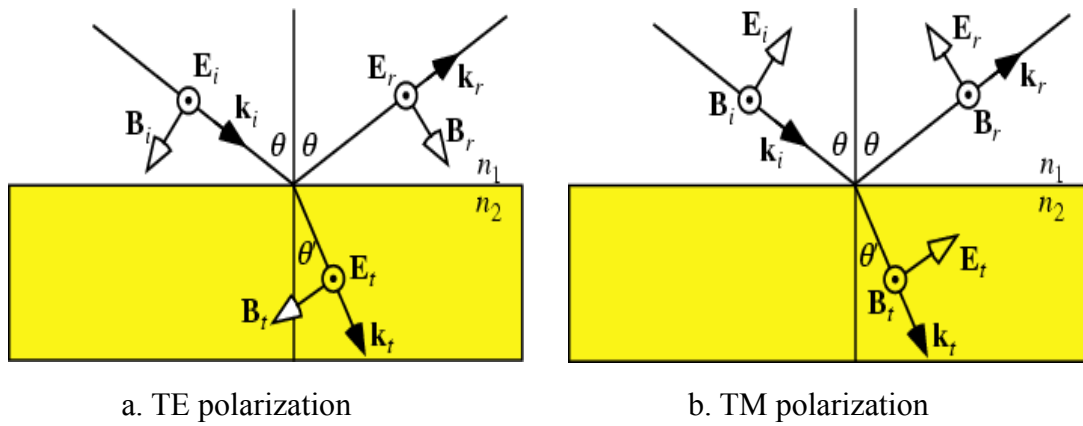
### 3.2.1.2 Optical Waveguide Coupling Methods

The prism waveguide coupling techniques have advantages over other refractive index measurement techniques in that no immersion fluid is needed and higher accuracy is attained. The only commercial prism waveguide coupling equipment for measuring the refractive index of polymer films is manufactured by Metricon Corporation<sup>50</sup>. It has two work functions: the mode method and the knee method, for thin film and thick film/bulk, respectively. In the present research, the knee method was used to measure the refractive index of the pure IPP film. However, it is limited to transparent samples. It can't be used to measure the IPP-CB films which are optically absorbing. Therefore a new technique was designed to deal with the problem. Liu et al. modified the Metricon waveguide coupler and developed a new Internal Reflection Intensity Analysis (IRIA) method<sup>8</sup> which can measure both the refractive index and the extinction coefficient in a wide complex refractive index region.<sup>51</sup> In this section, after the description of the 3-D optical measurement concept, the knee method and the IRIA method will be introduced, followed by the discussions of other optical constant measurement techniques.

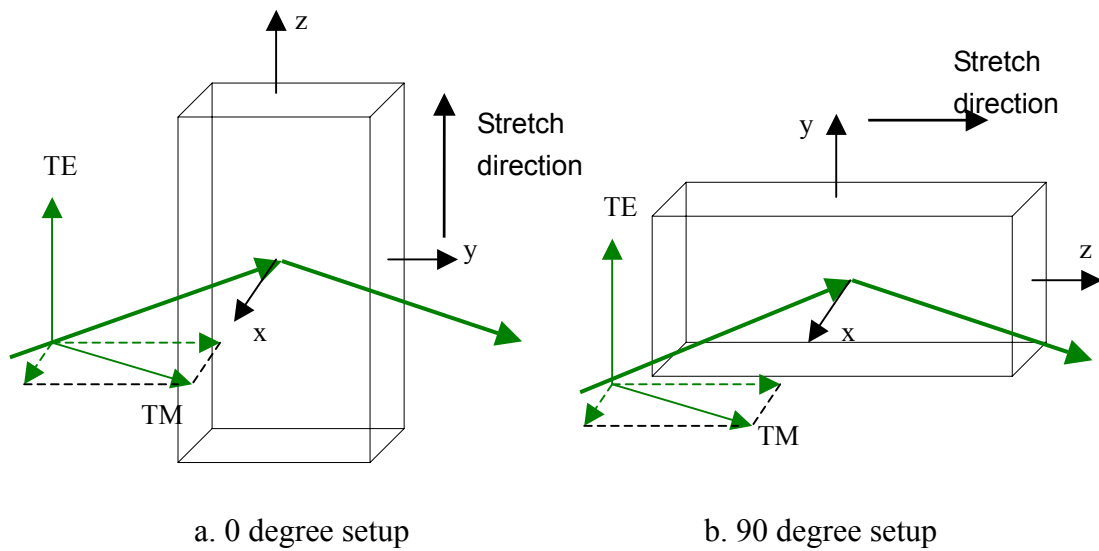
#### 3.2.1.2.1 Three-Dimensional Optical Measurement Concept

In order to get the 3-D refractive index, polarized light was used. There are two kinds of polarizations: TE and TM (Figure III-4). In Figure III-4, the  $E$  and  $B$  are the electrical field and magnetic field of the light, respectively and  $k$  is the light propagation vector. TE stands for transverse electric field and TM is short from

transverse magnetic field<sup>52</sup>. Figure III-5 shows the concept of the 3-D optical measurement. In Figure III-5, the green line indicates the light. In TE polarization, the electric field is along the z (y) direction of the sample for 0 (90) degree setup. So the TE measurements will provide the optical constants along z and y directions. For TM, the electric field can be decomposed into two directions, one is the through-plane direction, x, and another is an in-plane direction. For the 0 degree setup, the TM measurement includes the information of  $n_x^*$  and  $n_y^*$ ; at 90 degree setup, it includes the information of  $n_x^*$  and  $n_z^*$ . So in order to get the three principal refractive indices, the sample will be measured at 0 and 90 degrees under TE to get  $n_z^*$  and  $n_y^*$ , respectively, and then be measured under TM at 0 and/or 90 degrees. In order to calculate the refractive index along the through-plane direction,  $n_x^*$ , for the 0 degree TM measurement, the 90 degree TE result,  $n_y^*$ , needs to be substituted into the waveguide model equation of TM measurement; similarly, for 90 degree, the 0 degree TE result,  $n_z^*$ , needs to be substituted into the waveguide model equation of TM measurement. Whatever the setup angle used, the through-plane direction result should be the same.<sup>55</sup>



**Figure III-4.** Two polarizations (a. TE; b. TM)



**Figure III-5.** The 0 degree and 90 degree setups for optical measurement (The TM incident light is decomposed along the dashed lines.)

### 3.2.1.2.2 The Knee Method

The principal behind the knee method is Snell's Law (See Snell's Law in 3.2.1.1.1):

$$n_1 \sin(\theta_1) = n_2 \sin(\theta_2) \quad \text{Eq. III-4}$$

Because the sine function cannot have a value greater than one, when  $n_1 < n_2$  there is no value of  $\theta_1$  that will satisfy the expression for some values of  $\theta_2$ . Thus, for light passing from a medium with a higher refractive index to a medium with a lower refractive index there is a critical angle of incidence, above which there is total reflection rather than refraction<sup>33</sup>. At the critical angle between transmission and total reflection, the relationship between the refractive indices of the two media becomes:

$$n_2 = n_1 \sin(\theta_c) \quad \text{Eq. III-16}$$

where  $\theta_c$  is the critical angle.

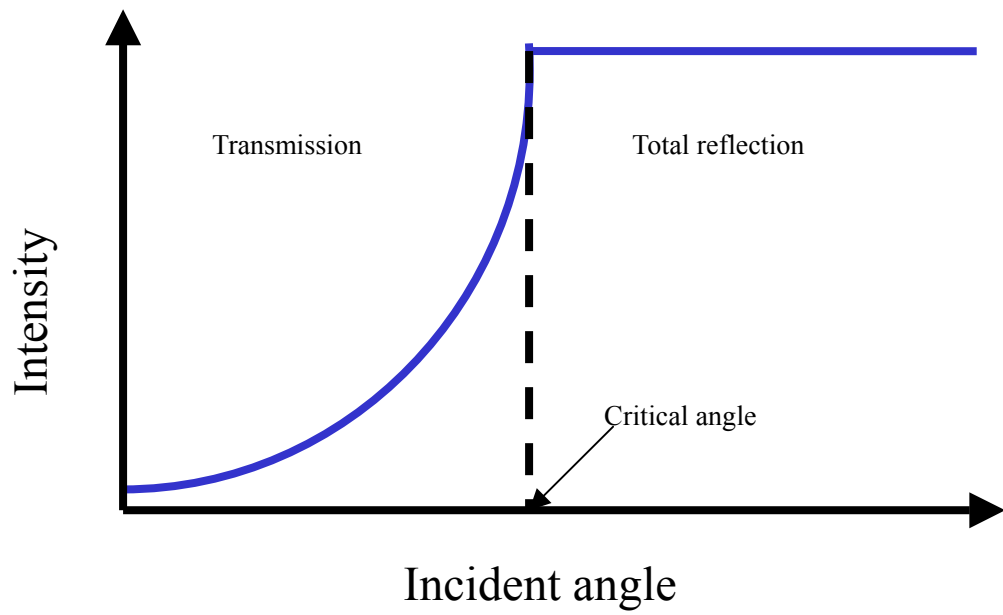
If a constant intensity is incident from the higher refractive index medium, the intensity of the reflected beam will show a sharp drop at the critical angle (Figure III-6). This is the basic principal of the knee method. The setup of Metricon PC-2010 waveguide coupler is schematically shown in Figure III-7. The main components of the coupling system are a laser source, a polarizer, a prism, a detector and a pneumatically controlled coupling head. The sample was pushed against the high refractive index prism by compressed air. A laser sends light through a polarizer and travels toward the interface between the prism and the sample. The reflected intensity is recorded by the detector. With the table rotating, initially, the light is totally internally reflected from the prism base, and then, at a certain discrete angle,  $\theta_c$ , the light tunnels into the sample, resulting in a decrease in the intensity measured by the



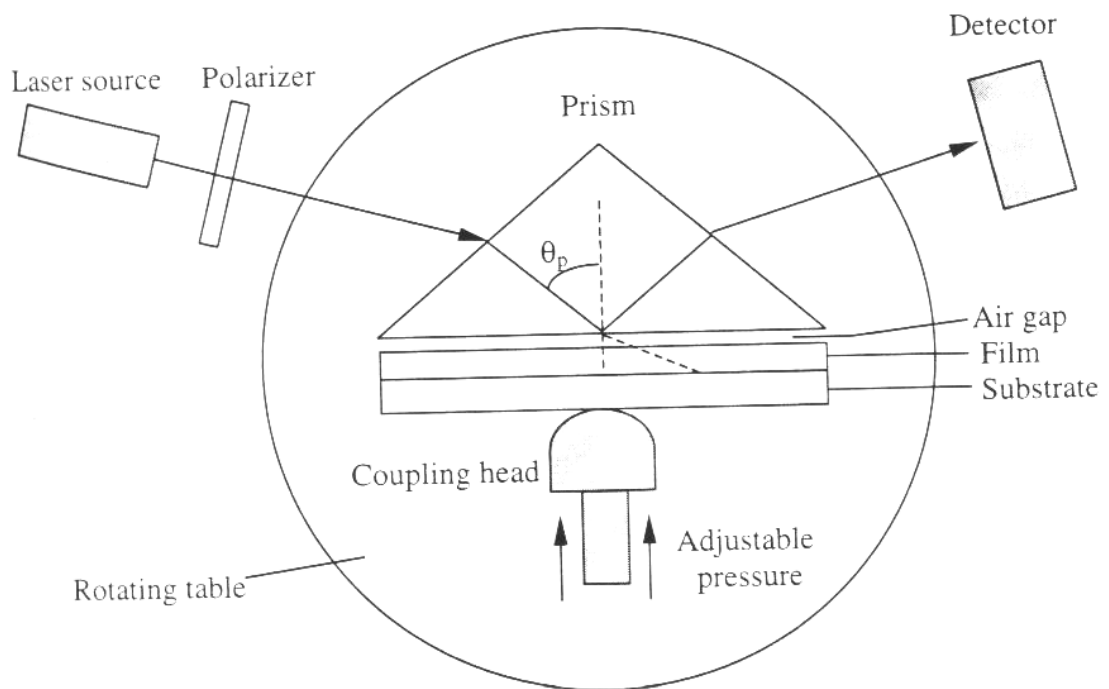
detector. This sharp drop is the so-called knee<sup>50</sup>. Since the refractive index of the prism is known, the refractive indices of the film can be calculated from Eq. III-16. In the measurement, the sample will be measured under different polarizations and setup angles, so that the 3-D refractive index can be obtained (see 3-D optical measurement concept in 3.2.1.2.1).

In the Metricon PC-2010, the intensity was measured every 0.015 degree and the knee is found by the biggest slope point in the reflected intensity curve. Manufacture's specifications claim that the error in the measured index is less than .004 for a film thickness of 3 microns, less than .001 at 5 microns, and less than .0003 at 10 microns<sup>50</sup>.

This method is only good for transparent samples, so that the extinction coefficient can be ignored. When the extinction coefficient is high, the knee is not sharp, so the error from the knee method is large. This error will be discussed in details in 12.4.



**Figure III-6.** Change of reflected intensity with incident angle<sup>50</sup>



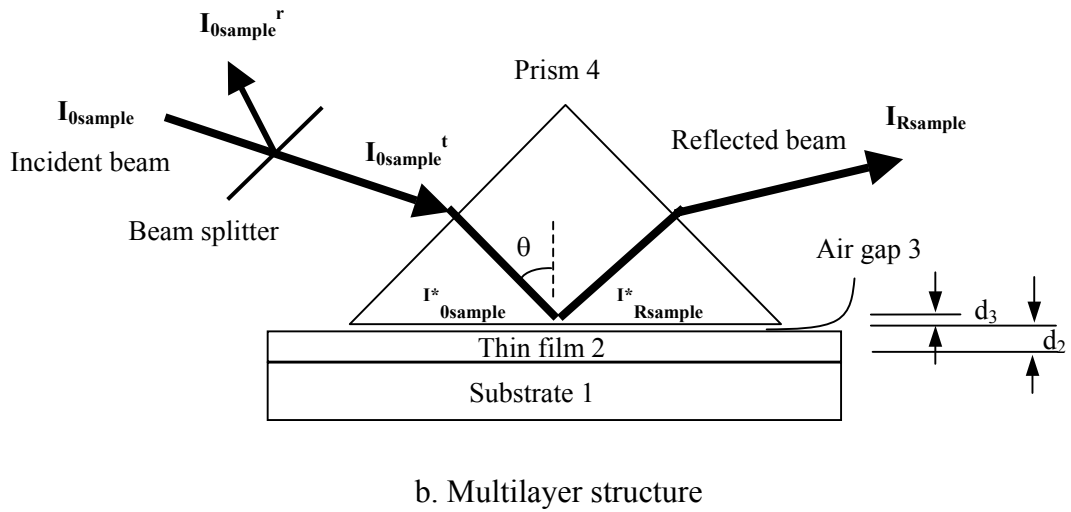
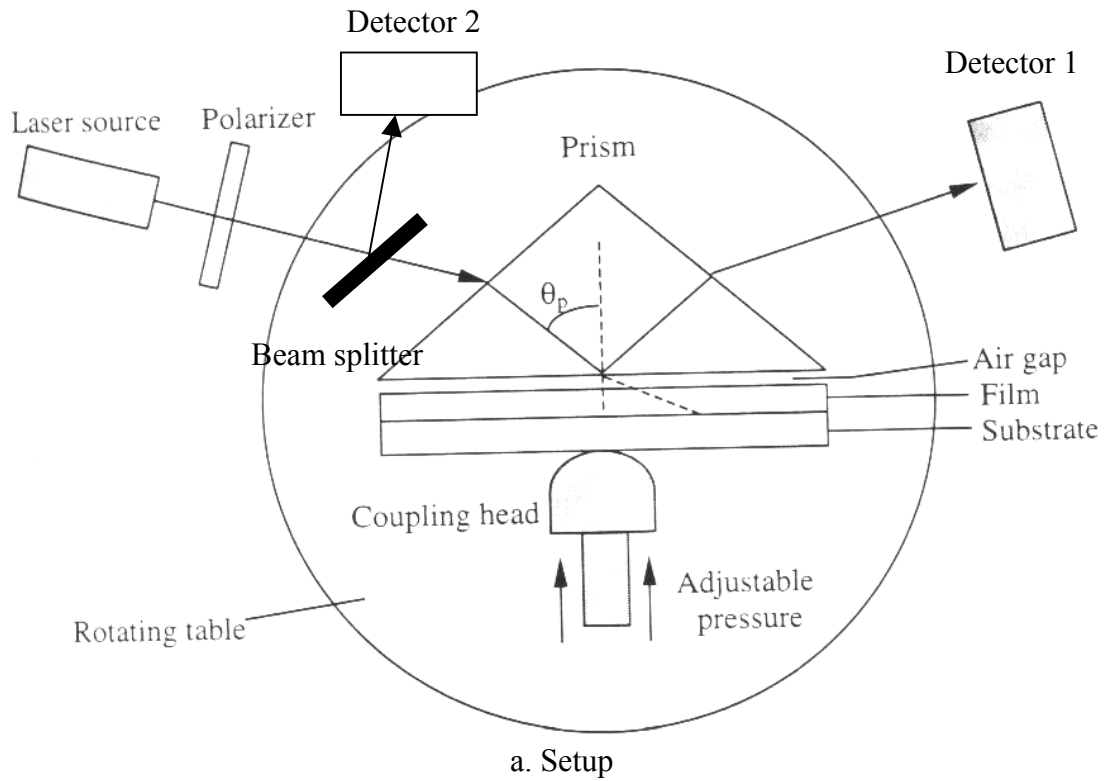
**Figure III-7.** The schematic structure of the Metricon PC 2010 waveguide coupler<sup>50</sup>

### 3.2.1.2.3 The IRIA Method

The method used to measure the 3-D optical constants of IPP-CB films is the IRIA method. The IRIA method is a new nondestructive method which can be used to measure the 3-D complex refractive index. It is obtained by modifying the Metricon PC-2010. Figure III-8 shows the schematic diagram for the IRIA method.<sup>8, 51</sup> The IRIA method is setup by adding a beam splitter and a detector in the Metricon PC-2010 to measure the intensity of the incident light and using multimeters instead of the Metricon data card to read the light intensities. The multimeter has a higher resolution than the Metricon data card.

The principal behind the IRIA method is thin film optics. In thin film optics, the reflection can be written as a function of the complex refractive index and the thickness of each layer. Figure III-8 shows that the IRIA method can be seen as a multilayer optical systems.<sup>8, 51</sup>

For a free-standing polymer film, there are three layers: the prism, the airgap and the film. The phase and intensities of the light will change at the interface between each two layers with the properties of the media. The reflectance,  $R = I_{R, \text{sample}}^* / I_{O, \text{sample}}^*$ , the ratio of the incident light and the reflected light at the base of the prism, includes the information of all the interactions in the three layers. Therefore the reflectance is a function of the complex refractive index and the thickness of each layer. In the IRIA method, the refractive index of the prism and air is known, so the reflectance is a function of the complex refractive index of the sample and the thickness of the airgap. Liu gave the equations of the IRIA model for both TE and TM polarization.<sup>8, 51</sup>



**Figure III-8** The schematic structure of the IRIA waveguide method<sup>8, 53</sup>

In order to fit the complex refractive index and the thickness of the airgap, the reflectance curve that changes with incident angles was fitted to the IRIA model by the least square method.<sup>8, 51</sup> The measurement covers the incident angle region from total reflection to transmission. The reflectance,  $R$ , can be obtained from two separate measurements, one of the sample and the other of the air (without sample), respectively<sup>8, 51</sup>, by

$$R = \frac{I_{R, \text{sample}} / I_{O, \text{sample}}^r}{I_{R, \text{air}} / I_{O, \text{air}}^r} \quad \text{Eq. III-17}$$

where the subscript  $R$  and  $O$  indicate the reflected and incident laser beams, respectively; the subscript *sample* and *air* are the measurement of the sample and air, respectively; the superscript  $r$  means the reflected beam of the incident light from the beam splitter.

In Eq. III-17, the  $I_R$  and  $I_O$  are the intensity measured from Detector 1 and Detector 2, respectively [Figure III-8 (a)]. In the IRIA method, the intensities are recorded every 0.15 degree. Typically, the error is in the third place after the decimal point for both the refractive index and the extinction coefficient. The error will be discussed in 12.1.

The accuracy of the IRIA method has been confirmed by comparing the results of solvent blue 59 dyed polystyrene films from the IRIA method with other techniques, such as ellipsometry (see ellipsometry in 3.2.1.2.4) and KK transform based ultraviolet-visible/near-infrared (UV/Vis/IR) reflectometry.<sup>53</sup> The IRIA method has been successfully used on optical property studies of hydrogen chloride (HCl) doped polyaniline (PANI) and 3M vinyl electrical tape. It shows that the IRIA method works well on isotropic and anisotropic uniformly optically absorbing samples<sup>8, 51, 53</sup>.

#### 3.2.1.2.4 Other Optical Constant Measurement Methods

For transparent samples, the optical constants and birefringence can also be measured by some other techniques, such as the polarized refractometer<sup>54</sup> and the polarized optical microscope.<sup>55</sup> Recently, there are some new techniques based on the interference concept.<sup>56, 57</sup> Horn et al. used conoscopy to determine the optical orientation and birefringences of stretched polymer films<sup>56</sup>. In this method, the average refractive index was assumed in the model fitting. As a result, the in-plane birefringences are almost completely insensitive to the average refractive index used for numerical fit routine. The results were approximately 0.005 less than the compensator measurement. The author mentioned it might be due to miscalibration of the compensator. The out-of-plane birefringence, however, shows a more significant dependence on the choice of average refractive index. So an accurate determination of the out-plane birefringence does require at least an approximate value of the average refractive index. Hamza et al. setup a micro-strain device attached to the optical system for producing multiple-beam Fizeau fringes in transmission to determine the refractive index and the birefringence of IPP fibers at different stresses<sup>57</sup>. This is a two-dimensional method. It is only good for fibers or uniaxial stretched films. Therefore these new methods didn't provide higher accuracy or more information. The knee method may be the best choice for the measurement of the refractive index of a thick transparent film.

The two main methods for the complex refractive index measurement of optically absorbing samples are ellipsometry and ultraviolet-visible/near-infrared reflectometry

based on the KK transformation. In 3.2.1.1.4, the limitation of KK transformation has already been discussed. In the present research, since the carbon black concentration is only 1% or 2%, the extinction coefficient of IPP-CB is less than 0.1 which is not high enough to obtain accurate extinction coefficient value from the KK transform technique ( $k$  needs to be larger than 0.1) (See KK transform in 3.2.1.1.4). Ellipsometry is an experimental technique that studies the changes of the state of polarization when an incident light transmits through or reflects from a layered media structure<sup>58,59</sup>. This technique requires that the sample to be measured must have a very smooth surface. Otherwise, the surface roughness can introduce depolarization for the reflected light so that erroneous optical constants can be obtained.<sup>60</sup> However, the IPP-CB samples are not smooth, especially the stretched films. The IRIA has no requirement on the sample thickness or a very smooth surface, so the IRIA waveguide method may be the only choice for the complex refractive index measurement of IPP-CB system.

### 3.2.2 Fourier Transform Infrared (FTIR) Spectroscopy

FTIR is widely used in chemical structure studies. It is found that the absorbance bands in FTIR also relate to the physical structure of the samples. The method for revealing the crystallinity and orientation function of isotactic polypropylene by FTIR will be introduced in this section.

#### 3.2.2.1 Crystalline and Average Band

It has been found that in the FTIR spectrum of IPP, there are several peaks for the crystalline phase and some others for the average phase, where the average phase is the overall of crystalline and non-crystalline phase. Some of them are listed in Table III-3.

**Table III-3** Crystalline and average bands of IPP in FTIR spectrum

<b>Band (cm<sup>-1</sup>)</b>	<b>Phase</b>	<b>References</b>
1256	Average	61, 62, 63, 64, 65, 66, 67
1220	Crystalline	61, 62, 63, 67
1045	Crystalline	63, 64, 65
998	Crystalline	43, 63, 64, 65, 68, 69,
973	Average	43, 63, 64, 68, 69
898	Crystalline	61, 62, 66
840	Average	61, 62, 66
809	Crystalline	61, 62, 66

It was also found about 40 years ago that the ratio of the absorbance of crystalline band and average band has a linearly relationship with the density.<sup>70, 71</sup> The density also linearly relates the crystallinity of IPP, so the band ratio can be used to calculate the crystallinity.<sup>69, 70</sup> The principal behind this method is Beer-Lambert Law (Eq.



III-18):

$$A = \ln\left(\frac{I_0}{I}\right) = t\varepsilon Vd \quad \text{Eq. III-18}$$

where  $A$  is the absorbance,  $I_0$  is the incident intensity of phase absorption frequency,  $I$  is the transmitted intensity of phase absorption frequency,  $t$  is the thickness of the sample,  $\varepsilon$  is the absorptivity of the unique phase material,  $V$  is the volume fraction of the phase and  $d$  is the density of the phase.

So the ratio of the absorbance of crystalline and average phase could be written as

$$\frac{A_c}{A_{ave}} = \frac{\varepsilon_c d_c}{\varepsilon_{ave} d_{ave}} V_c = \frac{\varepsilon_c d_c V_c}{\varepsilon_{ave} [V_c d_c + (1 - V_c) d_{nc}]} = \frac{\varepsilon_c}{\varepsilon_{ave}} \frac{d_c V_c}{(d_c - d_{nc}) V_c + d_{nc}} \quad \text{Eq. III-19}$$

The densities of the crystalline and noncrystalline phases of IPP are 0.936 and 0.857 g/cm<sup>3</sup>, respectively<sup>72, 73</sup>, so Eq. III-19 can be written as:

$$\frac{A_c}{A_{ave}} = \frac{\varepsilon_c}{\varepsilon_{ave}} \frac{0.936 V_c}{0.079 V_c + 0.857} \approx \frac{\varepsilon_c}{\varepsilon_{ave}} \frac{0.936 V_c}{0.857} = 1.09 \frac{\varepsilon_c}{\varepsilon_{ave}} V_c \quad \text{Eq. III-20}$$

Therefore the ratio of the crystalline and average phase has a linear relationship to the crystallinity. Currently, this method is still used in some research in both pure isotactic polypropylene and IPP-CB system.<sup>4, 74</sup>

In other crystallinity measurement methods, such as the density method and the refractive index method, the effect of carbon black is very hard to be separated from the system, so error may be introduced. Compared to these methods, the FTIR method has a big advantage in the IPP-CB system study. If the CB has no peaks overlapping with the IPP crystalline and average phase bands, the ratio will directly present the crystallinity of IPP in the system, because the effect of CB can be easily eliminated from the baseline adjustment. However, indeed, this is only a semi-quantitative

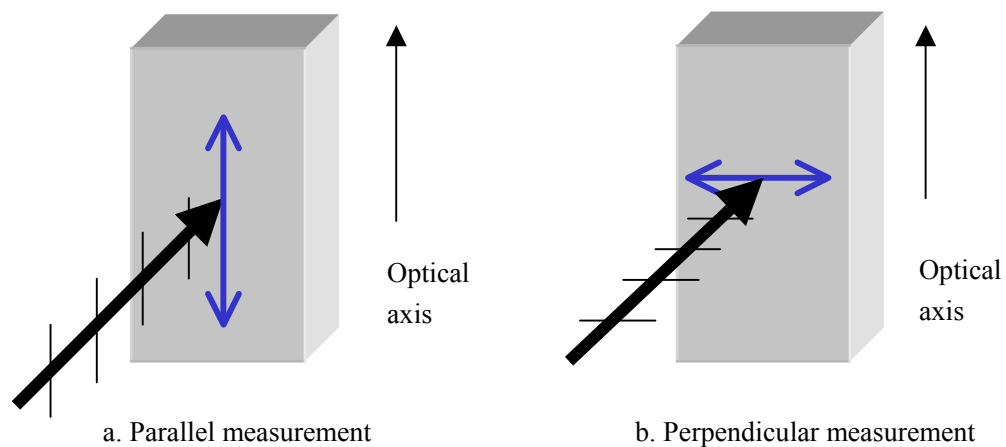
method. The relationship between the absorbance ratio and the crystallinity of IPP depends on the peaks chosen and also the equipment parameters, such as the resolution and the scan times.

In this study, this method will be used as a secondary method to confirm the crystallinity of isotactic polypropylene in the IPP-CB system.

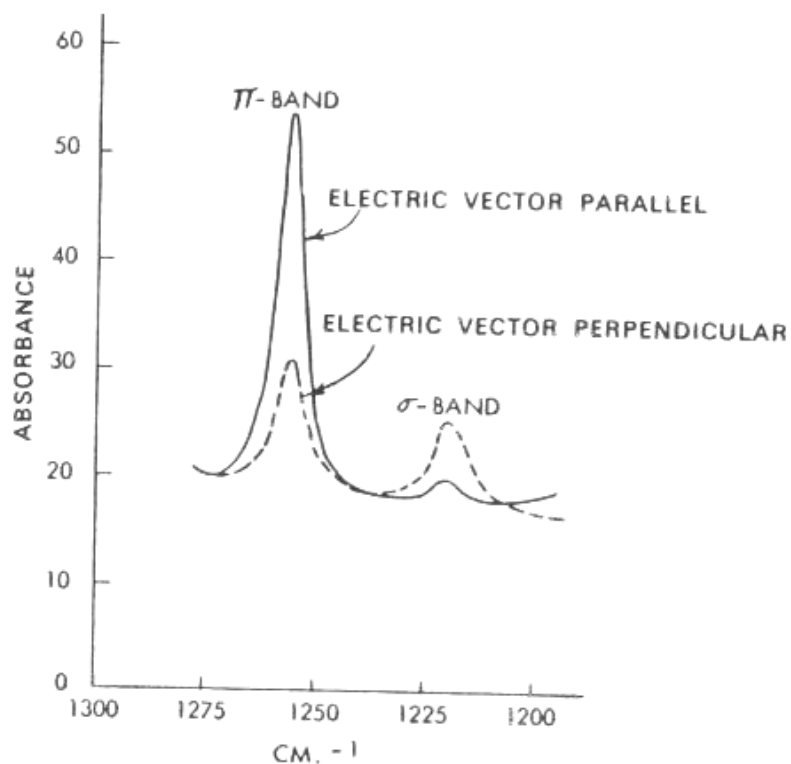
### 3.2.2.2 Infrared Dichroism

FTIR dichroism measurement is one of the methods used to obtain the Hermans' orientation function of each phase of a semi-crystalline polymer. In the dichroism measurement, a polarized infrared beam is used. Similar to the optical measurement, the FTIR can also be observed using two kinds of polarization. However, since in the FTIR transmission mode measurement, the laser beam is perpendicular to the sample surface, the electric vector is always in the sample plane, so only the in-plane information can be obtained. If the polarization direction is along the sample orientation direction, it is called the parallel, //, setup; if it is perpendicular to the sample orientation direction, it is called the perpendicular,  $\perp$ , setup (Figure III-9).

For a randomly oriented sample, the FTIR spectra at different polarizations are the same; however, for orientated samples, at some wavenumbers, the peak heights are different under different polarization. This difference is described by the types of band. There are two kinds of bands, a  $\pi$  band and a  $\sigma$  band. A  $\pi$  band means the height of the peak measured with parallel polarization is bigger than that measured with perpendicular polarization; oppositely, it is called a  $\sigma$  band (Figure III-10)<sup>31</sup>.



**Figure III-9.** The two polarization setups of FTIR measurement



**Figure III-10.** Infrared dichroism of cast uniaxially oriented polypropylene film<sup>31</sup>.

The ratio of the peak height of the  $\pi$  band or  $\sigma$  band is the dichroic ratio,  $D$ <sup>31</sup>(Eq. III-21):

$$D = \frac{A_{\parallel}}{A_{\perp}} \quad \text{Eq. III-21}$$

where  $A$  is the absorbance of the peak.

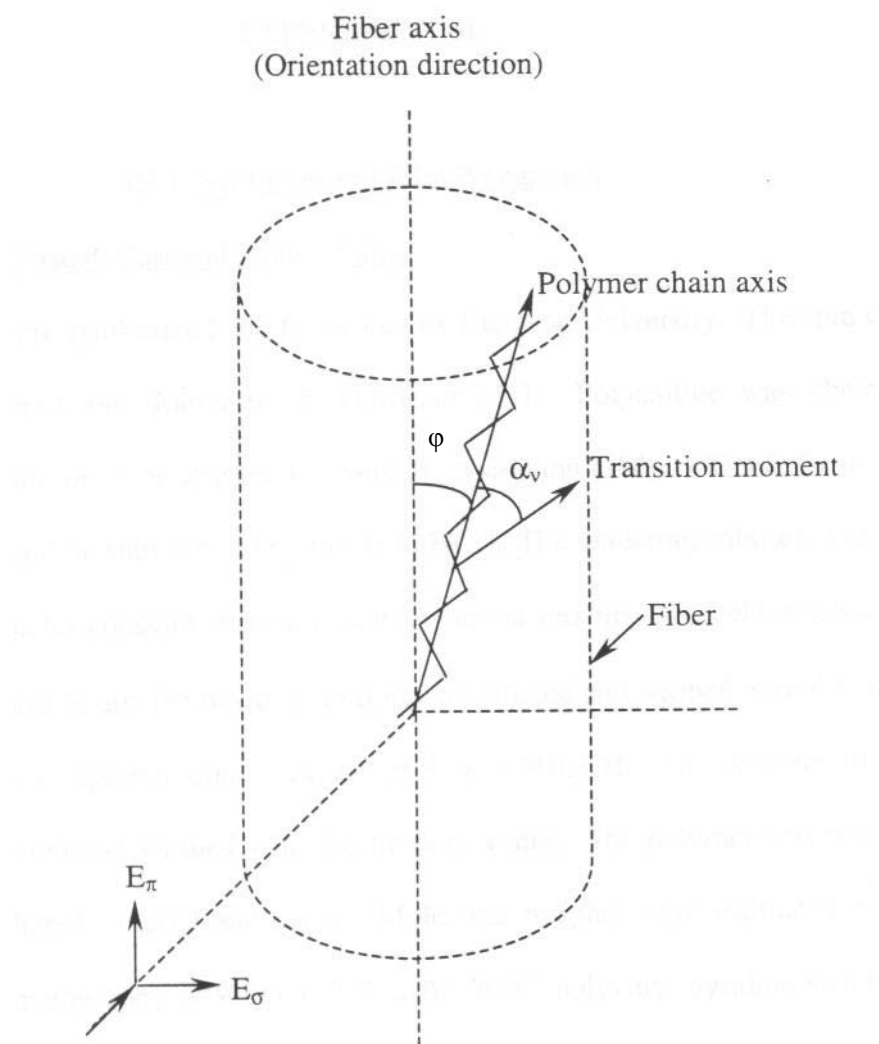
Fraser solved the relationship between the infrared dichroism,  $D$ , the orientation function,  $f$ , and the transition moment angle,  $\alpha_v$ <sup>75</sup>. The transition moment angle is the angle between the dipole vibration and the polymer chain orientation. The relationship of the transition moment angle,  $\alpha_v$ , and the orientation angle,  $\phi$ , is shown in Figure III-11. The FTIR dichroic ratio includes both angles. In order to determine the orientation function, which is a function of  $\phi$  only, the effect of the transition moment angle must be eliminated. For a given peak, the orientation function of the indicated phase is (Eq. III-22)<sup>75</sup>:

$$f = \frac{(D-1)(D_0+2)}{(D+2)(D_0-1)} = \frac{3 \langle \cos^2 \phi \rangle - 1}{2} \quad \text{Eq III-22}$$

where  $D_0$  is the dichroic ratio of an ideally orientated polymer, which is related to the transition moment angle,  $\alpha_v$ , (Eq. III-23):

$$D_0 = 2 \cot^2(\alpha_v) \quad \text{Eq. III-23}$$

Therefore, once the transition moment angle of a crystalline (average) band is known, the orientation function of the crystalline (average) phase could be calculated by Eq III-22 and Eq. III-23.



**Figure III-11.** The relationship of transition moment angle and orientation angle<sup>31</sup>

In the present study, the  $988\text{cm}^{-1}$  band and  $973\text{cm}^{-1}$  band will be used to obtain the orientation function of crystalline and average phase, respectively. Pepper provided the transition moment angle of these two bands. The values on different resolutions of FTIR are shown in Table III-4<sup>76</sup>.

**Table III-4.** The transition moment angles of  $988\text{cm}^{-1}$  and  $973\text{cm}^{-1}$  band of IPP<sup>76</sup>

Resolution ( $\text{cm}^{-1}$ )	1		2		4		8	
Band ( $\text{cm}^{-1}$ )	988	973	988	973	988	973	988	973
$\alpha_v$ ( $^\circ$ )	15	14	15	14	16	17	18	22

The dichroism method is a well-established method. With the development of the FTIR techniques, it was also used in Infrared Microscopy<sup>74</sup>, Attenuated Total Reflectance infrared Spectroscopy (ATR-IR)<sup>77, 78, 79, 80</sup> and FTIR photoacoustic spectroscopy (FTIR-PAS)<sup>81</sup>.

Song et al. used microscopic infrared dichroism measurements of a quenched IPP thin film during stepwise elongation to obtain the molecular orientation function of the crystalline and noncrystalline phases.<sup>74</sup> The results not only provided the orientation function along the draw direction, but also showed a correlation between  $f_c$  and  $f_{nc}$ , namely  $f_c=1.85f_{nc}$ . The problem in the results is that they used the peak ratio of  $998\text{cm}^{-1}$  and  $973\text{cm}^{-1}$  as the crystallinity and hence determined  $f_{nc}$ . As was discussed in 3.2.2.1, the ratio is not accurate. On the other hand, in the calculation, they used the old reported data of the transition moment angle<sup>63</sup>, which was updated later by Pepper<sup>76</sup> (see Table III-4). Therefore, this relationship needs to be tested by other independent research results.

Since in the ATR-IR measurement, the beam is not normally incident to the sample surface, the same applies as the concept discussed in 3.2.1.2.1, the ATR-IR can provide 3-D information. Mirabella developed an ATR-IR measurement method which used the  $841\text{cm}^{-1}$  band with a parallel transition moment vector and the  $809\text{cm}^{-1}$  band with a perpendicular transition moment vector for isotactic polypropylene surface characterization.<sup>77</sup> Samuels used this method to study the orientation of thick sheets and thin films of isotactic polypropylene. The orientation of IPP evaluated by polarized ATR spectroscopy matched the results from polarized refractometry very well<sup>78</sup>. Recently, Kirov et al. used ATR-IR to obtain the 3-D optical constants of stretched polypropylene in the infrared region<sup>79</sup>. This method is based on the KK transform (see KK transform in 3.2.1.1.4). Because of the limitation of the KK transform, more information is needed to test this method. Everall et al. also used the polarized ATR-IR to quantify biaxial orientation in commercially manufactured poly(ethylene terephthalate) (PET) film and stretch-blow molded bottles<sup>80</sup>. However, there are no reports on the application of ATR-IR to polymer-nano composite stretched films.

### 3.2.2.3 Rolling Baseline

When the sample is not very thick, the baseline in the FTIR spectrum is not a straight line, but a “rolling baseline”<sup>62, 82</sup> (Figure III-11<sup>62</sup>). In Figure III-12, P is the period of the rolling baseline which is the distance between the two peaks. The rolling is due to the interference of the IR light between the two surfaces of the film<sup>57</sup>. If it is assumed

the refractive index does not change with the wavelength, the period of the rolling baseline is a function of the refractive index and the thickness of the sample<sup>83</sup> (Eq. III-24)

$$t = \frac{1}{2} n P \quad \text{Eq. III-24}$$

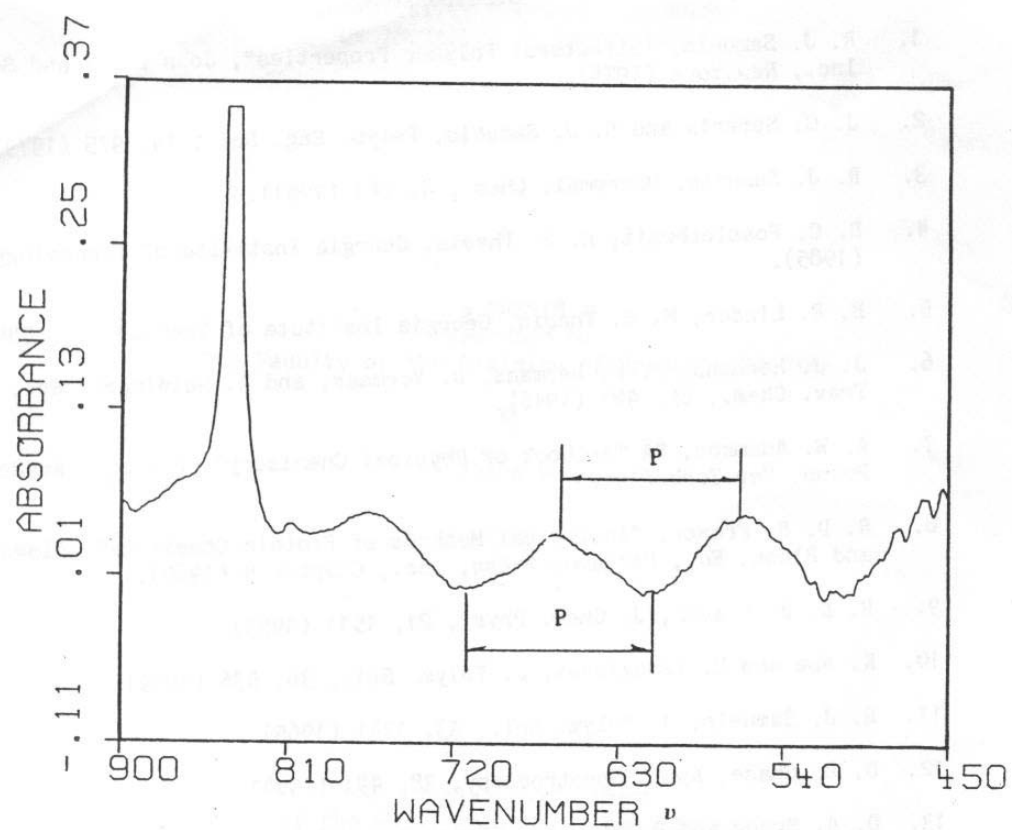
where  $t$  is the thickness of the sample; And  $P$  is the period of the rolling baseline

In the dichroism measurement, the sample is measured in parallel and perpendicular directions. These two directions relate to the two in-plane directions of the sample,  $z$  and  $y$ , respectively. For a stretched sample, the refractive indices at the two in-plane directions are different, so the periods of the rolling baselines in the parallel and perpendicular spectra are not the same. Eq. III-24 can be used to deduce the relationship of birefringence and the period of the rolling baseline:

$$\Delta_{zy} = n_z - n_y = 2t \left( \frac{1}{P_{//}} - \frac{1}{P_{\perp}} \right) \quad \text{Eq. III-25}$$

In the spectra, the difference of the period is presented as a shift of the phase of the rolling baseline. So the bigger the shift, the larger the birefringence and the higher the orientation.





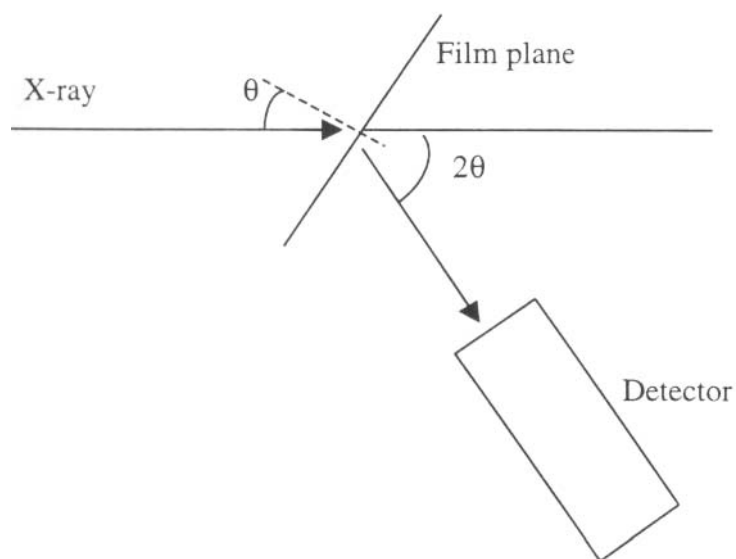
**Figure III-12.** The rolling baseline in FTIR<sup>61</sup>

### 3.2.3 X-ray

The orientation function of the crystalline phase in polycrystalline polymers can be studied by X-ray diffraction. If a monochromatic X-ray beam impinges on the crystal, and the crystal is rotated, a diffraction pattern will be obtained that is characteristic of the size and the shape of the unit cell<sup>31</sup>.

#### 3.2.3.1 $2\theta$

The angle between the incident ray and the reflecting plane is defined as angle  $\theta$ . When the beam incidents perpendicular to the sample, it will be diffracted along  $2\theta$  to the detector (Figure III-13)<sup>84</sup>.



**Figure III-13.** Schematic picture of normal incident x-ray diffraction<sup>84</sup>

Since in the experiment, the distance between the x-ray tube and the sample is fixed, the distance between the center of the pattern and the diffraction ring (or arc) presents the value of  $2\theta$ <sup>84</sup>. The  $\alpha$ -form crystal is the most stable and the most common form to

arise from the isotactic polypropylene melt. The crystal unit cell structure of the  $\alpha$ -form crystal is monoclinic. The unit cell parameters are listed in Table III-5<sup>85</sup>.

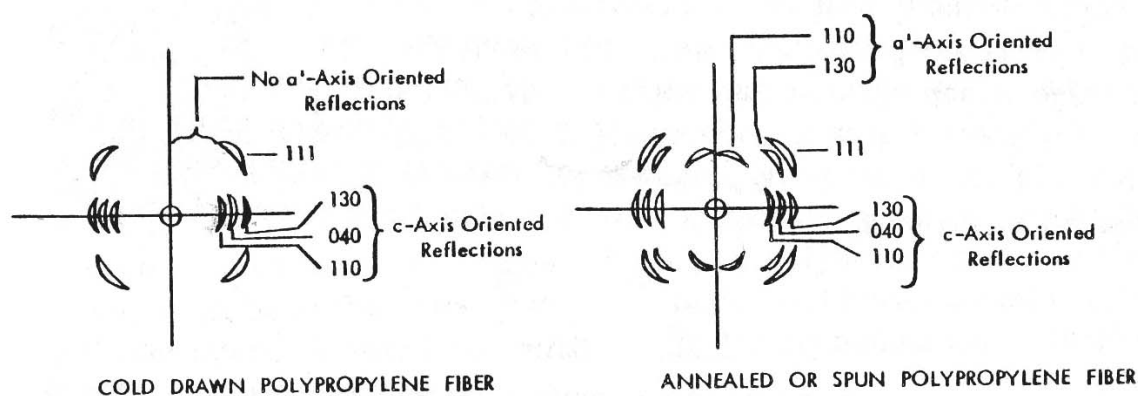
**Table III-5** Crystallographic data for isotactic polypropylene<sup>85</sup>

Unit cell parameters*				Monomer units in cell	Density, g/cc.		Ref.
a, Å	b, Å	c, Å	$\beta$ , °		Cryst.	Amorph.	
6.65	20.96	6.50	99.3	12	0.936	0.85	86, 87
6.666	20.87	6.488	99.8		0.937		88
6.64	20.88	6.51	98.7				89
6.69	20.98	6.504	99.5	12	0.9323	0.8538	90

\* a, b and c are the crystal axes;  $\beta$  is the monoclinic angle

Figure III-14 shows the schematic diffraction pattern of the  $\alpha$ -form of the IPP crystal<sup>31</sup>.

In Figure III-14, there are no strong reflections of the type  $(00l)$ , but the patterns for  $(110)$ ,  $(130)$  and  $(040)$ , etc. planes are clear<sup>31</sup>.



**Figure III-14.** Schematic drawing of x-ray diffraction pattern of IPP fiber<sup>31</sup>

Based on the crystal unit structure, the  $2\theta$  of each plane can be calculated by<sup>84</sup>

$$d = \left[ \frac{\left(\frac{h}{a}\right)^2 + \left(\frac{l}{c}\right)^2 - \frac{2hl\cos(\beta)}{ac}}{\sin^2(\beta)} + \left(\frac{k}{b}\right)^2 \right]^{-0.5} \quad \text{Eq. III-26}$$

and

$$n\lambda = 2d \sin \theta \quad \text{Eq. III-27}$$

where  $h$ ,  $k$  and  $l$  are the Miller indices; and  $a$ ,  $b$  and  $c$  are the crystal axes;  $\beta$  is the monoclinic angle;  $n = 0, 1, 2, 3$ , and so on,  $\lambda$  is the wavelength, and  $d$  is the interplanar spacing.

For IPP, the  $2\theta$  values of (110) and (040) planes are 14.1 and 16.9 degrees, respectively.

### 3.2.3.2 Crystal Forms

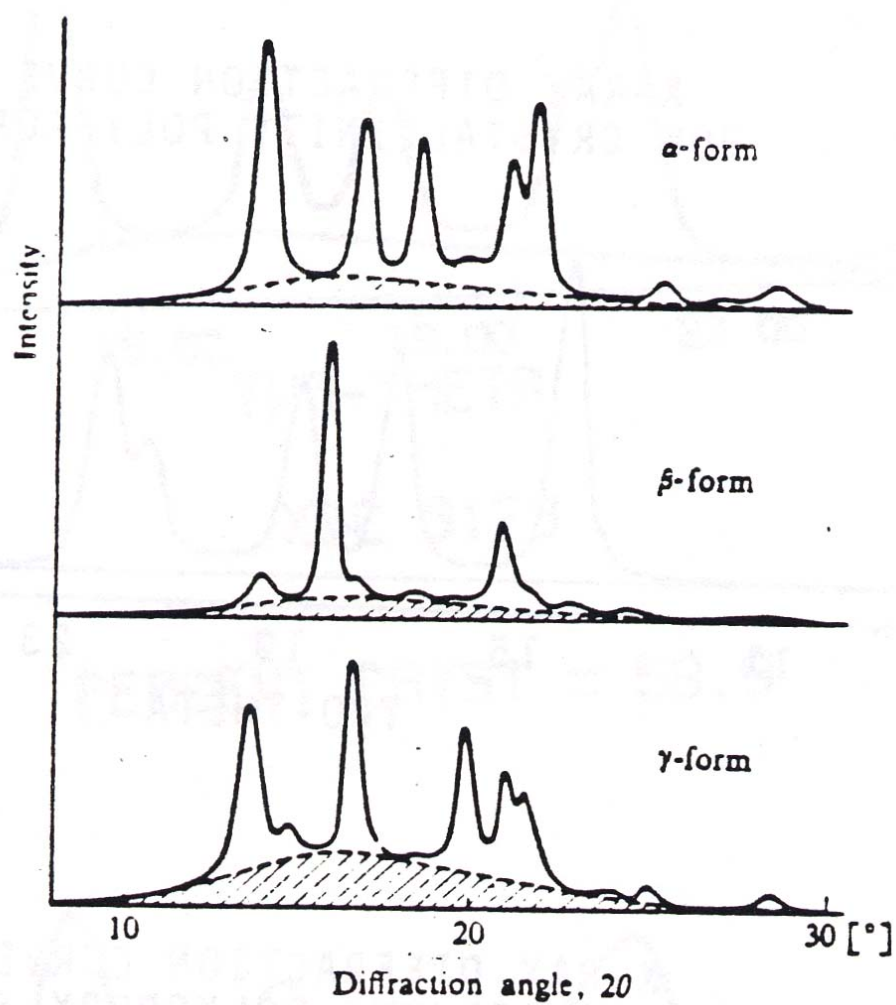
IPP has three crystal forms,  $\alpha$ -,  $\beta$ - and  $\gamma$ -form. By integrating the intensity around the azimuthal angles and plotting against  $2\theta$ , the diffraction intensity curves can identify the crystal forms. The intensity curves of the three crystalline forms of IPP are shown in Figure III-15<sup>91</sup>.

Figure III-15 clearly shows that the different crystal forms have diffraction peaks at different  $2\theta$  angles. For example, the strong (300) peak characterizes the  $\beta$  form crystal.

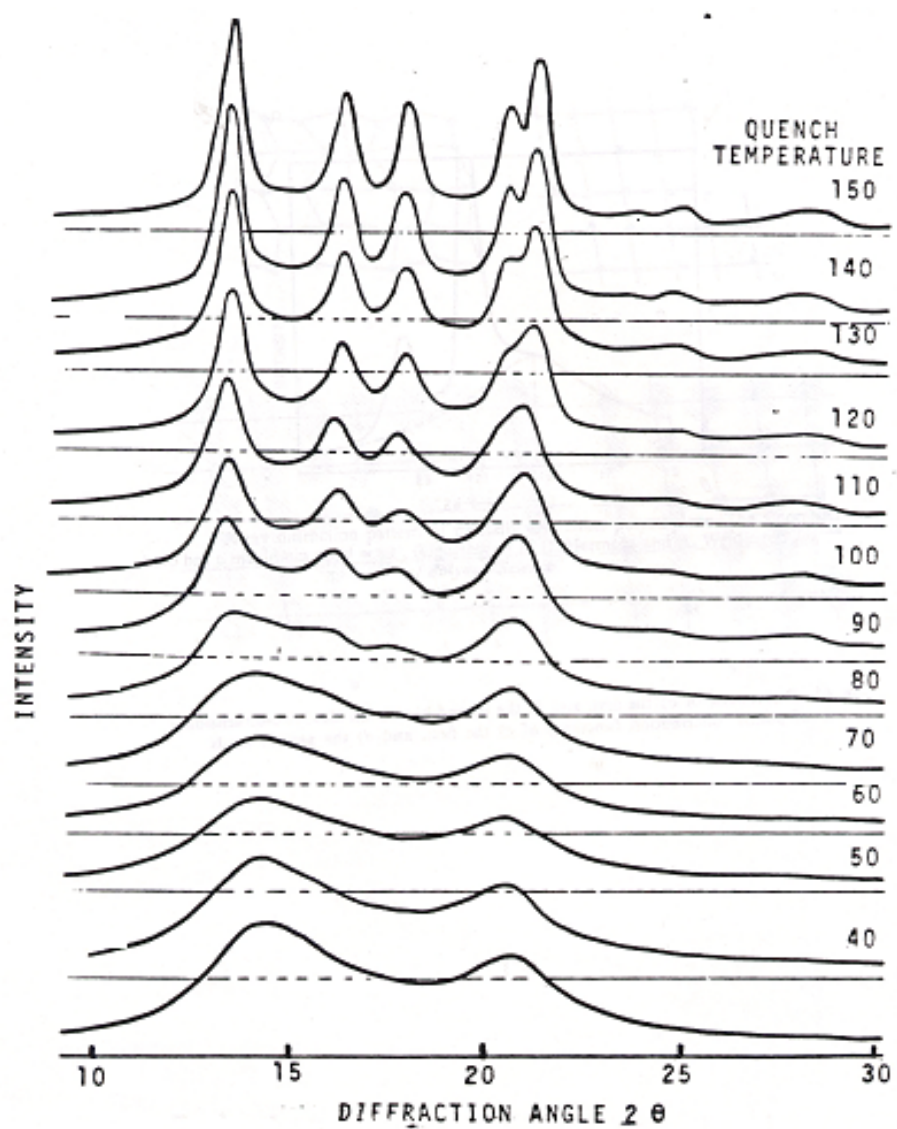
Sobue et al. reported a new crystalline structure for IPP, called the “smectic” mesophase<sup>92</sup>. The characteristic is that the diffraction from the (100), (010) and (110) planes gradually merge and become one peak<sup>92</sup>. Miyamoto et al. studied the structure

formation process of isotactic polypropylene from the glass into the "smectic" mesophase by small-angle x-ray scattering, wide-angle x-ray scattering and differential scanning calorimetry<sup>93</sup>. The structure of the smectic phase was unaltered during the transition process, which indicates no spinodal decomposition process is present in the formation of the smectic phase from the supercooled melt in IPP. The long period of the nodular structure was 5 nm to 6 nm independent of annealing temperature lower than -15 °C. The glass transition temperature increased from -30 °C to +1 °C by the formation of the smectic phase.

Samuels found that the "smectic" structure is only due to the poor perfection of the  $\alpha$ -crystal of isotactic polypropylene<sup>91</sup>. In Figure III-16, the same kind of IPP films, when quenched at the different temperatures indicated, had different diffraction patterns. When the film was quenched at room temperature, the characteristic "smectic" structure is produced. The well formed  $\alpha$ -crystal diffraction peaks of the film quenched at 150°C can be seen to broaden and merge as the quench temperature is decreased. Even at a quench temperature of 70°C, the presence of all four peaks can be identified, although their  $2\theta$  position has shifted due to peak broadening and overlap as the crystal perfection decreases. Thus the  $\alpha$ -crystal remains but crystal size and defects have produced a change in the observed x-ray diffraction patterns. Only by presenting the diffraction patterns in the systematic manner shown in Figure III-16 can the obvious continuity of the  $\alpha$ -form structure be observed.



**Figure III-15.** X-ray diffraction intensity of three crystal forms for IPP<sup>91</sup>



**Figure III-16.** The x-ray diffraction intensity pattern of the IPP sample quenched at different temperatures<sup>91</sup>

### 3.2.3.3 Crystallinity

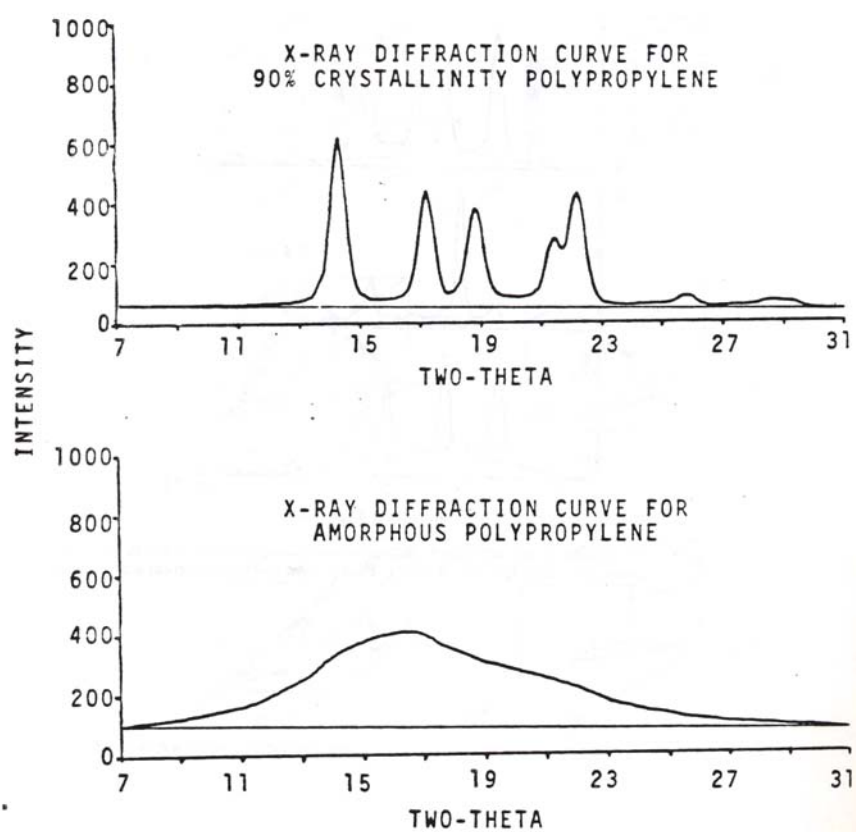
The crystallinity can be calculated by integrating the intensity with angles by Eq. III-28<sup>31</sup>:

$$V_c = \frac{\int_0^\infty \sin^2(\theta) I_c(\theta) d\theta}{\int_0^\infty \sin^2(\theta) I(\theta) d\theta} \quad \text{Eq. III-28}$$

Where  $I_c$  and  $I$  are the intensities of the crystalline phase and whole sample, respectively.  $I_c$  is calculated by subtracting the amorphous background from the overall intensity curve.

Figure III-17 shows x-ray intensity patterns of an amorphous IPP sample and a highly crystallized IPP sample. For a general IPP sample, the x-ray diffraction intensity includes both the crystalline phase and the amorphous phase. In order to calculate the crystallinity, the amorphous phase must be subtracted as a background. The best way to do that is using the shape of the curve of the amorphous IPP to match the baseline at the low and high  $2\theta$  regions, where no crystalline diffraction peaks are observed. In Figure III-15, the shadowed area shows the background based on the amorphous phase<sup>91</sup>.

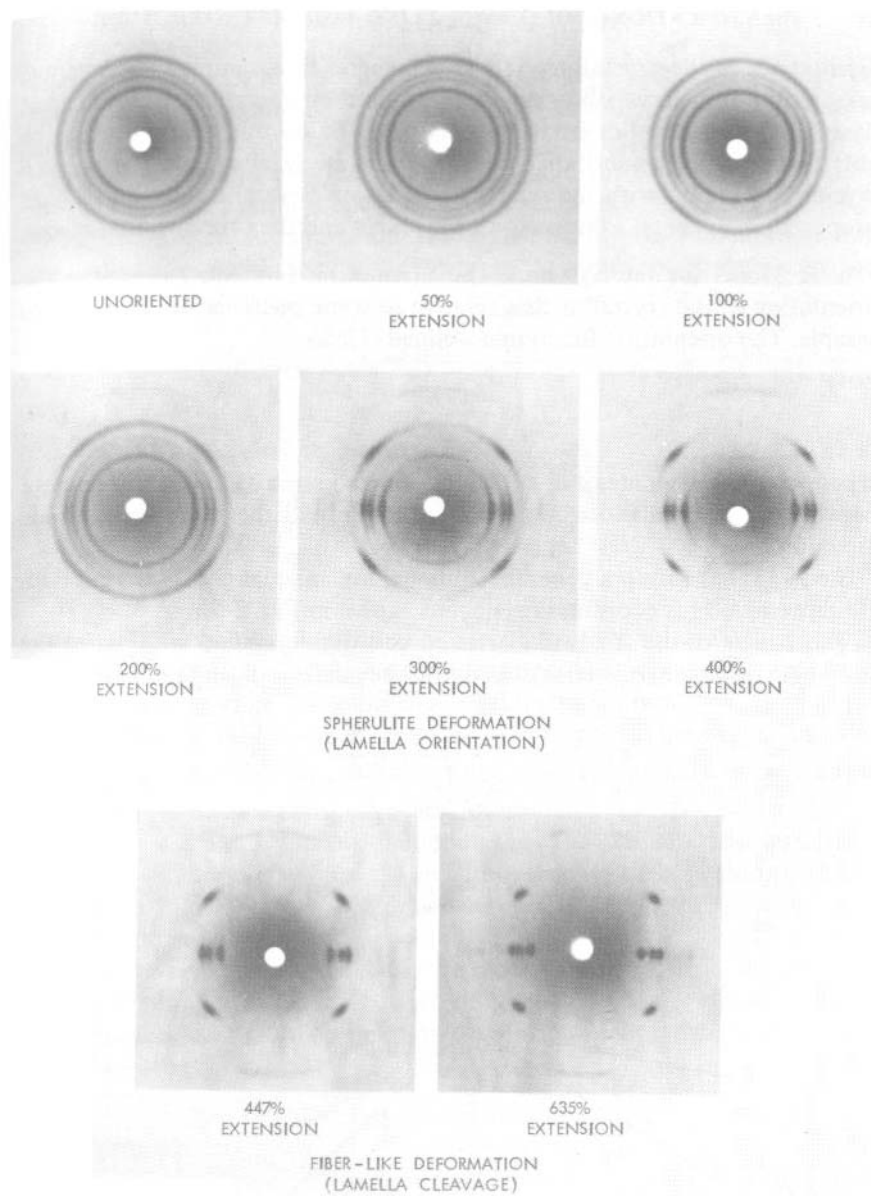




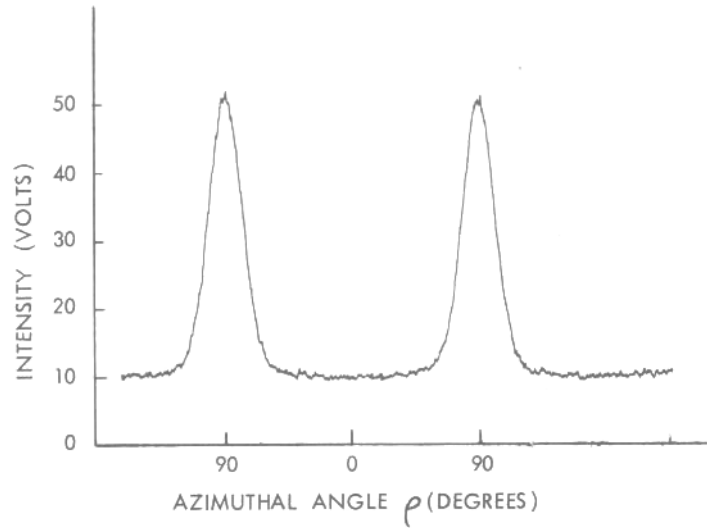
**Figure III-17.** X-ray diffraction intensity pattern of 90% crystallinity IPP and amorphous IPP<sup>91</sup>

#### 3.2.3.4 The Orientation Function

Figure III-17 shows the x-ray diffraction pattern obtained from IPP films stretched to different draw ratios<sup>31</sup>. In the pattern of an unstretched sample, the intensity of each plane is uniformly distributed around the azimuthal angles. However once it is stretched, the polymer chains tend to be parallel to the stretch direction, with the result that  $\langle \cos^2 \varphi_{c,z} \rangle$  ( $\varphi_{c,z}$  is the average angle between the  $c$  axis of the crystal unit and the stretch direction) is a direct measure of the molecular orientation relative to some reference direction  $z$  in the sample<sup>94</sup>. The diffraction rings in the pattern are broken into arcs<sup>31</sup> (Figure III-18). In order to calculate the  $\langle \cos^2 \varphi \rangle$  of each axis, which relates to the Herman's orientation function,  $f$ , the intensity at  $2\theta$  of the given plane around the azimuthal angles is collected. Figure III-19 is a typical (040) azimuthal intensity scan from an oriented isotactic polypropylene.



**Figure III-18.** Effect of isotactic polypropylene film extension on the wide-angle x-ray diffraction pattern<sup>31</sup>



**Figure III-19.** Typical 040 azimuthal intensity distribution scan from oriented isotactic polypropylene<sup>31</sup>

For normal incidence of the x-ray beam, the relationship of the orientation angle of the polymer chain,  $\phi$ , and the orientation angle of the  $(hkl)$  plane,  $\chi$ , is<sup>95</sup>

$$\langle \cos^2 \phi_{hkl} \rangle = \langle \cos^2 \chi_{hkl} \rangle \langle \cos^2 \theta_{hkl} \rangle \quad \text{Eq. III-29}$$

Where the value of  $\theta$  for (110) and (040) diffraction planes were calculated to be  $7.06^\circ$  and  $8.46^\circ$ , respectively<sup>96</sup>.

The equation to solve  $\langle \cos^2 \chi \rangle$  of the  $(hkl)$  plane is

$$\langle \cos^2 \chi_{hkl} \rangle = \frac{\int_0^{\pi/2} I(\chi) \sin \chi \cos^2 \chi d\chi}{\int_0^{\pi/2} I(\chi) \sin \chi d\chi} = \frac{\int_0^{\pi/2} (I_{\text{meas}} - I_{\text{back}}) \sin \chi \cos^2 \chi d\chi}{\int_0^{\pi/2} (I_{\text{meas}} - I_{\text{back}}) \sin \chi d\chi} \quad \text{Eq. III-30}$$

where  $\chi$  is the azimuthal angle,  $I_{\text{meas}}$  and  $I_{\text{back}}$  are the measured and background intensities, respectively<sup>31</sup>.

Therefore the method of choosing baseline is very important to get accurate orientation function. Huber discussed the effect of the baseline in the x-ray diffraction<sup>66</sup>. He indicated that at high orientation, the peak was sharper, more narrowly distributed; in that region the minimum value of the reflection did

correspond to the amorphous curve. But for low oriented sample, the real baseline should be lower than the minimum value of the reflection. Therefore in the present research, the baseline of a highly oriented sample is chosen as the minimum value of the reflection and a low orientation sample uses the same baseline as the high draw ratio (5X) sample with the same CB concentration (see details in 5.3.3).

Since IPP has no strong reflection at  $(00l)$  plane, in order to calculate the orientation along stretch direction, the geometry of the unit cell and the orientation of two other different plane directions need to be known. The general equation dealing with this problem is provided by Wilchinsky<sup>96</sup>:

$$\langle \cos^2 \varphi \rangle = 1 - \frac{(1 - 2\sin^2 \rho_2) \langle \cos^2 \varphi_1 \rangle - (1 - 2\sin^2 \rho_1) \langle \cos^2 \varphi_2 \rangle}{\sin \rho_1 - \sin \rho_2} \quad \text{Eq. III-31}$$

where the subscripts refer to the respective planes,  $\rho$  is the angle between the plane normal and the b axis and is calculated from the unit cell dimensions, and  $\varphi$  is the angle between the reference direction and the c axis. Thus, the orientation function for the c axis of isotactic polypropylene could be calculated once  $\langle \cos^2 \varphi_{hkl} \rangle$  had been determined for two reflecting crystal planes.

If the  $(110)$  and  $(040)$  are used to calculate the orientation function along stretch direction,  $\rho_1 = \rho_{110} = 72.5^\circ$  and  $\rho_2 = \rho_{040} = 0^\circ$ <sup>97</sup>. Then Eq. III-31 becomes<sup>97</sup>

$$\langle \cos^2 \varphi_{c,z} \rangle = 1 - 1.099 \langle \cos^2 \varphi_{110,z} \rangle - 0.901 \langle \cos^2 \varphi_{040,z} \rangle \quad \text{Eq. III-32}$$

Therefore x-ray diffraction can tell the crystal form, crystallinity and also the orientation function.

## CHAPTER IV

### EXPERIMENTS

#### 4.1 SAMPLE FABRICATION AND MOUNTING

##### 4.1.1 Materials

The films were made by the DOW Chemical Company. The films were cast by mixing isotactic polypropylene [5E40, Dow Chemical Company, 9.5 MFI (melting flow index), MW=190,000-200,000] with IPP-40%CB masterbatch (SCC Code 24000, Standridge Color Corporation). In the masterbatch, IPP is 12MFI and the particle size of CB (Raven 1220 Ultra, Columbian Chemicals Co.) is ~21nm.

##### 4.1.2 Sample Fabrication

###### 4.1.2.1 Casting Conditions

The films were cast at around 220 °C with a 25 mm Haake twin-screw extruder (co-rotating, intermeshing), with L/D (ratio of length and diameter) > 30. The film die is 6” wide, but the films tended to neck down during casting to about 4”. The film was cast onto a single chill roll cooled by recirculating water at 38 °C.

Three sets of films were produced, all designed to be drawn at a specific draw ratio to the same final thickness of 1.5 mils (38 microns); thus, their cast film thicknesses (Table IV-1) are targeted at the following for their respective future draw ratios:

**Table IV-1.** The cast film thickness and the target draw ratio

Film Thickness Target (mils)	Future Targeted Draw Ratio
1.50	1.0X
1.85	1.5X
2.60	3.0X
3.20	4.5X
3.50	5.0X and 5.5X

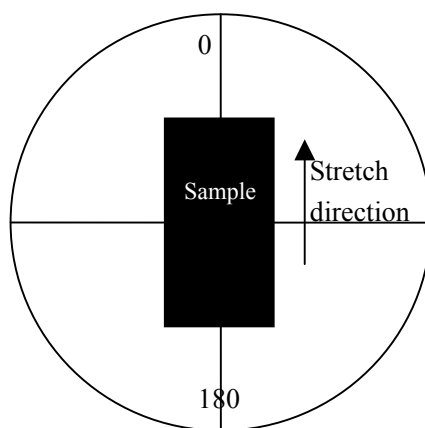
“Neat” films (no pigment) were comprised of all 5E40. The “translucent” films had 2.5 wt% of the masterbatch from SCC (effective 1% carbon black) tumble blended with the 5E40 and added to the extruder. The opaque films had 5% wt. of masterbatch (2% carbon black). Extrusion melt temperature for all films was around 220 °C.

#### 4.1.2.2 Drawing Conditions

The films were drawn (except for the 1.5 mil films, which were already at the desired final thickness) uniaxially through a 12-foot hot air oven between two unheated roll stands. Air set point was 140 °C, with an effective surface temperature (checked roughly with a roll surface pyrometer) of 100 – 110 °C. Roll stand 1 speed was 15 ft/min (with about a  $\pm 0.5$  ft/min variation). Variability of the second roll stand after the oven was  $< 0.2$  ft/min. The film was rolled up under low tension onto a Leesona tape winder. Draw ratios reported for each film were the roll stand speed ratios across the oven.

#### 4.1.3 Sample Mounting

The sample (about 2 cm by 1 cm) was cut from the center of the film, where it is uniformly stretched. Each cut sample was mounted on an individual 360° protractor. A hole about the sample size was cut at the center of the protractor. The 0° of the protractor is along the stretch direction which was judged by eye (Figure IV-1). All sample measurements will be at the center of the protractor.



**Figure IV-1.** A schematic draw of the sample mounting



## 4.2 STRATEGY

Since the IPP-CB film is a multiphase and multilevel system, in the present research, three nondestructive optical techniques, waveguide coupler, FTIR and x-ray diffraction, were applied to reveal the characteristics at the different structure levels. Subsequently, the relationship between the levels was used to check the results and unified the whole research. The strategy of the experiments is schematically shown in Figure IV-2. In Figure IV-2, the IPP-CB system was separated into the three levels: Level I — IPP and CB mixture, Level II — the crystalline and noncrystalline phases of IPP and Level III-- the crystal form of IPP.

### 4.2.1 Level I — IPP and CB Mixture

In the first level, the system was looked at as a mixture of IPP and CB. The optical waveguide methods, such as the knee method and the IRIA method, were used at this level to measure the three- dimensional optical constants ( $n$  and  $k$ ) of the stretched IPP and IPP-CB films. In the IPP-CB system, carbon black is optically absorbing, so the extinction coefficient relates to the distribution of carbon black in the film. Since the carbon black concentration is very low (1% or 2%), carbon black has little effect on the system refractive index. Therefore the refractive index presents the characteristics of IPP in the IPP-CB film. The refractive index can tell the sample axiality, crystallinity and also the birefringence (see 3.2.1.1.2).

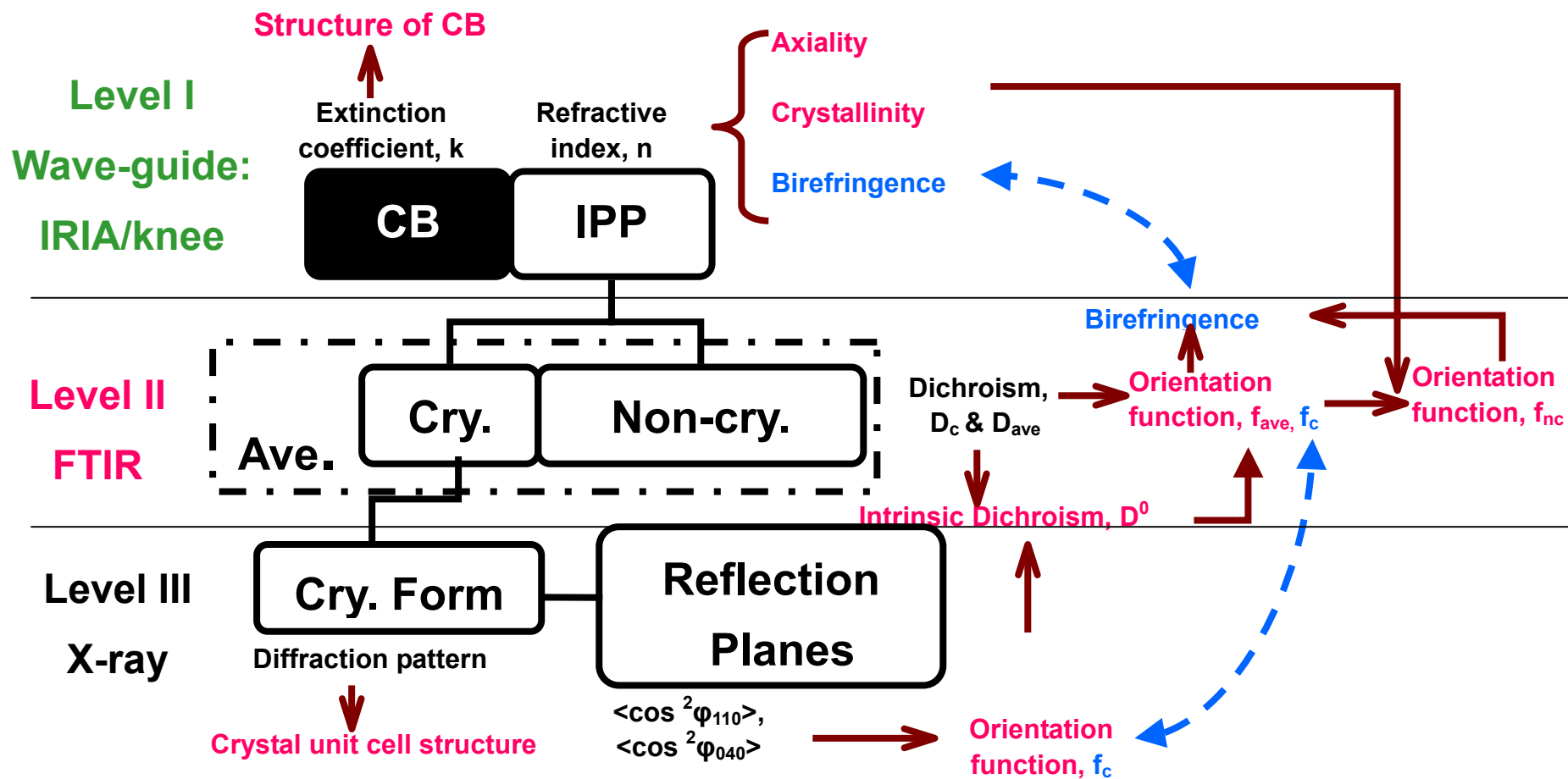


Figure IV-2. Strategy of the experimental procedure

#### 4.2.2 Level II – Crystalline and Noncrystalline Phases of IPP

However, staying in Level I is not enough. The IPP is not a single-phase material. It contains crystalline and non-crystalline phases. So in the second level, the FTIR was used to tell the behavior of each phase of IPP. In 3.2.2.2, the method of evaluation of the orientation functions of the crystalline, noncrystalline and average phases by the polarized FTIR was introduced. Eq. III-10 shows the equation used for calculation of the birefringence from the orientation functions of crystalline and noncrystalline phases. The birefringence from this method should match the birefringence from the refractive index from the waveguide. So the birefringence is the channel connecting the first two levels. On the other hand, as discussed in 3.2.2.1, the unpolarized FTIR will also be used to confirm the crystallinity of IPP in the IPP-CB system.

#### 4.2.3 Level III – Crystal Phase Of IPP

The third level is the detailed structure of the crystal form of IPP. In this level, X-ray diffraction will be used to tell the IPP crystal form (see IPP crystal form in 3.2.3.3) and calculate the orientation function of the crystalline phase (see  $f_c$  calculation by x-ray in 3.2.3.3). The orientation function of the crystalline phase from X-ray should agree with the result from FTIR. So this is the channel connecting the third level to the second level. The other relationship between x-ray and FTIR is the intrinsic dichroism, which is the dichroism value for a perfectly orientated film.

This is the whole map of how to obtain the information from the IPP-CB system.

Next, the experimental conditions of each method will be listed.

### 4.3 OPTICAL WAVEGUIDE

All the samples were measured at the center of the protractor at both 0 and 90 degrees under TE and TM polarizations (see 3-D optical measurement concept in 3.2.1.2.1) at room temperature (24 - 25°C). A green laser, whose wavelength is 543nm, was used in the optical waveguide measurements. The prism is triangular with the refractive indices of 2.184 for both the TE and TM measurements. The Metricon control software references the system. The neat IPP and the IPP-CB films were measured by the knee method and the IRIA method, respectively.

#### 4.3.1 The Knee Method

In the knee method (see knee method in 3.2.1.2.2), the intensity of the reflected beam was recorded by the Metricon control card every 0.015°. The incident intensity is assumed constant and the effect of the airgap between the prism and the sample is ignored. The Metricon control software located the knee position at the biggest intensity drop (slope) automatically<sup>50</sup>.

#### 4.3.2 The IRIA Method

For the IRIA method (see IRIA method in 3.2.1.2.3), the intensities of the incident and reflected beam were recorded by multimeters every 0.15°. The samples were measured with 300-400 different incident angles covering the total reflection to transmission regions. The intensity data were fitted by the IRIA fitting software written in Matlab<sup>8</sup>.

#### 4.4 FTIR

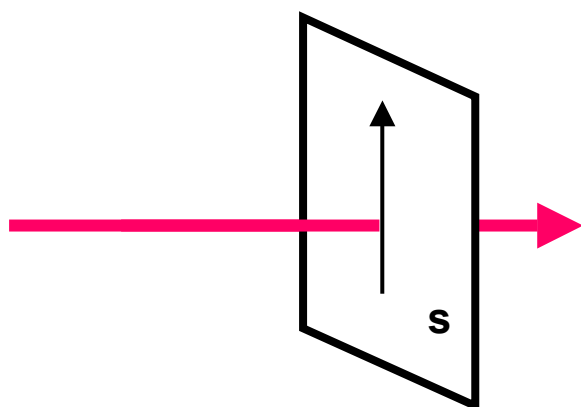
A BRUKER VECTOR 22 FTIR was used to measure the samples at room temperature by both polarized and unpolarized beams. The resolution was  $2\text{ cm}^{-1}$  and each measurement took 128 scans. The background was collected before every measurement. The FTIR software automatically adjusted the baseline of the whole spectrum. The absorbance was measured based on the peak baseline which connects the two minimums nearby the peak

##### 4.4.1 Unpolarized FTIR

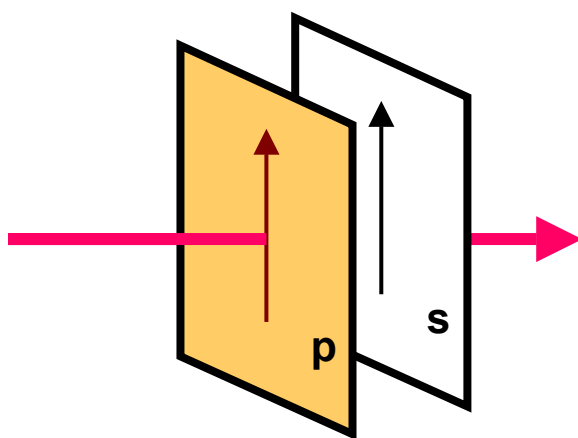
In the unpolarized FTIR measurement (see 3.2.2.1), the sample was inserted into the sample holder with the stretch direction in the vertical direction of the sample holder [Figure IV-3 (a)]. In Figure IV-3, the s and p indicate sample and polarizer, respectively. The arrows in the sample and polarizer refer the stretch direction and the polarization direction, respectively. The bigger arrow across the sample is the beam incident direction.

##### 4.4.2 Polarized FTIR

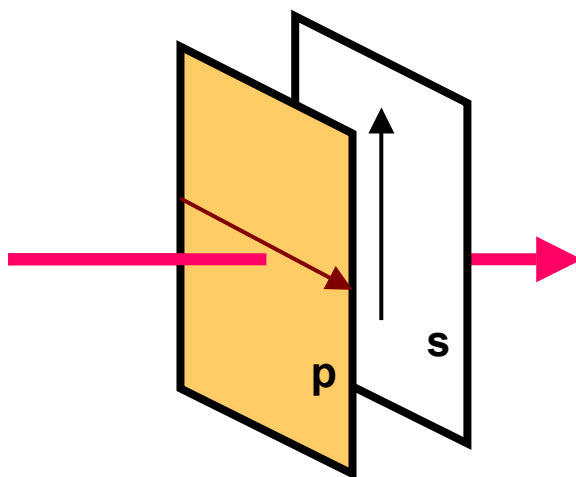
In the polarized FTIR (see 3.2.2.2), an IR polarizer with a sample holder was inserted into the sample holder of the FTIR. The sample was put into the sample holder of the polarizer. The stretch direction was kept in the vertical direction, but the polarizer direction will change from 0 degree for parallel measurement to 90 degree for perpendicular measurement (see 3.2.2.2) [Figure IV-3 (b)].



a. Unpolarized



b-1. Parallel



b-2. Perpendicular

**Figure IV-3.** The setup of unpolarized and polarized FTIR measurements

#### 4.5 X-RAY

The RIGAKU MICRO MAX 002 system with a MICROSOURCE X-ray generator and a RIGAKU R-AXIS IV++ detector was used to study the crystal form and the orientation function of the crystalline phase of IPP in the IPP-CB samples (see 3.2.3). The wavelength of the x-ray source used is 1.54056Å and the X-ray power is 44kV, 0.66mA. A 0.3mm collimator with no rear aperture controlled the beam size. The beam was incident perpendicularly to the sample. The system was calibrated by using corundum for  $2\theta$  and  $k_{\beta}$ . All unstretched samples were exposed two hours, but one hour for stretched samples.

## CHAPTER V

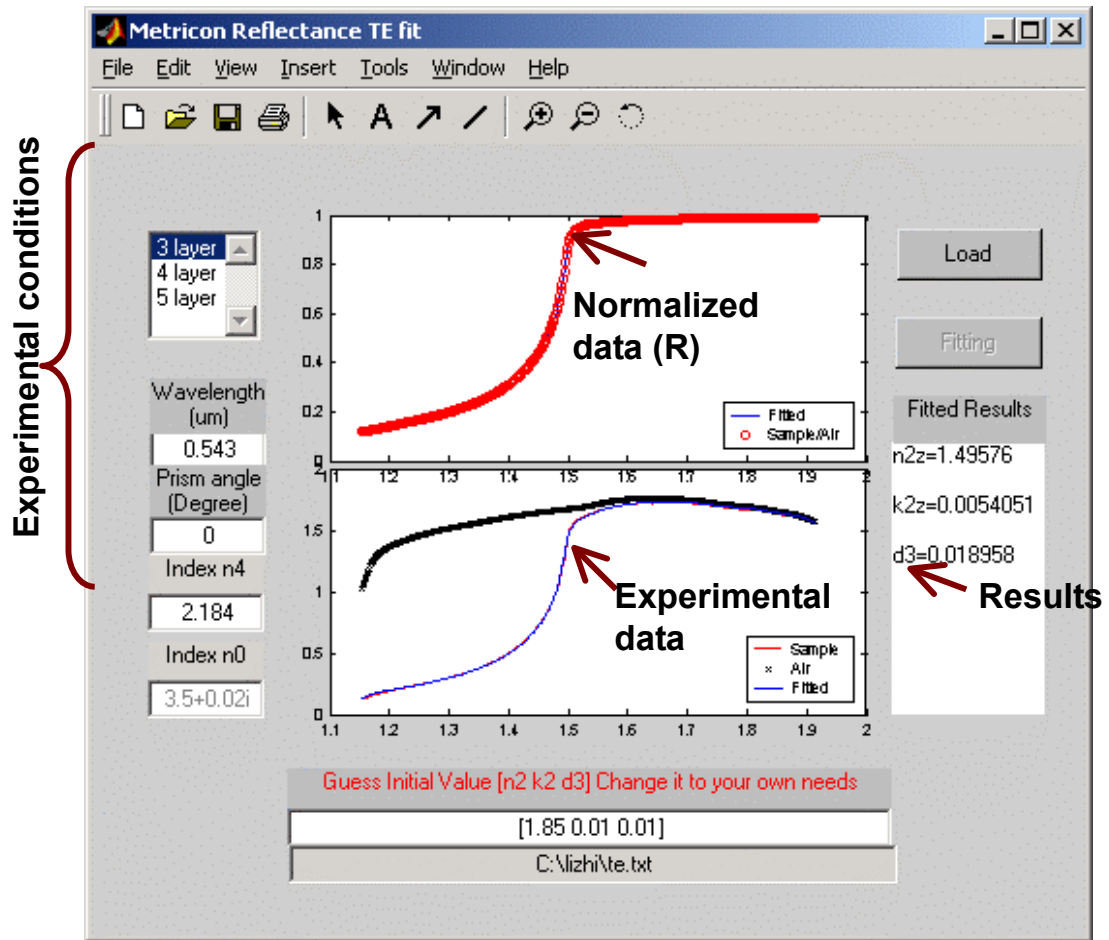
### RESULTS AND DISCUSSIONS

In Chapter IV, the experiment strategy was introduced. Therefore, in this chapter, the results of each level will be discussed. Finally, the relationship between each level will be used to check the results and to unify the whole research.

#### 5.1 LEVEL I – WAVEGUIDE MEASUREMENT RESULTS

The refractive index of IPP film was measured by the knee method and the refractive index and the extinction coefficient of IPP-CB films were obtained by the IRIA method. The experimental data of the IPP-CB samples fit the IRIA model very well. Figure V-1 gives an example of the IRIA fitting. The fitted curve (blue line) and the experimental curve (red line) are overlapping each other. All the experimental results are listed in Table V-1. In Table V-1, 0% CB indicates the neat IPP film and DR stands for draw ratio. The “error” is the experimental uncertainty. For the in-plane directions,  $z$  and  $y$ , the errors were provided by the Bootstrap Method (see Bootstrap Method in 12.1) with 99% confidence limit, but the error in  $x$  direction is the difference between the 0 and 90 degree TM measurements.





**Figure V-1.** An example of the IRIA fitting of IPP-CB samples (The example is IPP-1% CB 3X film, measured at 90° TE polarization @543nm)

**Table V-1.** The optical measurement results of IPP and IPP-CB samples

<b>3-D</b>			<b>z</b>				<b>y</b>				<b>x</b>			
		<b>n</b>	<b>n</b>		<b>k</b>		<b>n</b>		<b>k</b>		<b>n</b>		<b>k</b>	
<b>[C] %</b>	<b>DR</b>	<b>Ave</b>	<b>value</b>	<b>error</b>	<b>value</b>	<b>error</b>	<b>value</b>	<b>error</b>	<b>value</b>	<b>error</b>	<b>value</b>	<b>error</b>	<b>value</b>	<b>error</b>
0	1	1.4955	1.4955	--	--	--	1.4955	--	--	--	1.4956	0	--	--
	1.5	1.5062	1.5112	--	--	--	1.5037	--	--	--	1.5036	0.00034	--	--
	3	1.5067	1.5238	--	--	--	1.4984	--	--	--	1.4980	0.00020	--	--
	4.5	1.5064	1.5255	--	--	--	1.4969	--	--	--	1.4969	0	--	--
	5	1.5063	1.5266	--	--	--	1.4958	--	--	--	1.4966	0.00034	--	--
1	1	1.4956	1.4932	0.00140	0.0055	0.00088	--	--	--	--	1.4968	--	0.0060	--
	1.5	1.5067	1.5102	0.00056	0.0039	0.00020	1.5043	0.00108	0.0056	0.00052	1.5056	0.00240	0.0063	0.00245
	3	1.5053	1.5209	0.00108	0.0042	0.00028	1.4958	0.00068	0.0054	0.00039	1.4992	0.00259	0.0059	0.00035
	4.5	1.5056	1.5255	0.00052	0.0057	0.00024	1.4935	0.00116	0.0058	0.00039	1.4978	0.00305	0.0052	0.00015
	5	1.5056	1.5249	0.00032	0.0061	0.00032	1.4949	0.00048	0.0058	0.00036	1.4970	0.00107	0.0058	0.00025
	5.5	1.5033	1.5227	0.00140	0.0066	0.00108	1.4896	0.00208	0.0071	0.00108	1.4976	0.00368	0.0058	0.00160
2	1	1.4955	1.4937	0.00152	0.0109	0.00064	--	--	--	--	1.4964	--	0.0164	--
	1.5	1.5043	1.5077	0.00136	0.0119	0.00084	1.4994	0.00140	0.0123	0.00076	1.5058	0.00297	0.0133	0.00050
	3	1.5065	1.5149	0.00160	0.0120	0.00056	1.4995	0.00040	0.0098	0.00020	1.5051	0.00245	0.0128	0.00010
	4.5	1.5097	1.5243	0.00128	0.0160	0.00064	1.4990	0.00096	0.0140	0.00068	1.5058	0.00308	0.0125	0.00150
	5	1.5075	1.5235	0.00124	0.0137	0.00064	1.4954	0.00092	0.0139	0.00060	1.5036	0.00382	0.0153	0.00250
	5.5	1.5072	1.5268	0.00152	0.0158	0.00160	1.4938	0.00124	0.0117	0.00064	1.5010	0.00337	0.0114	0.00010

### 5.1.1 Extinction Coefficient

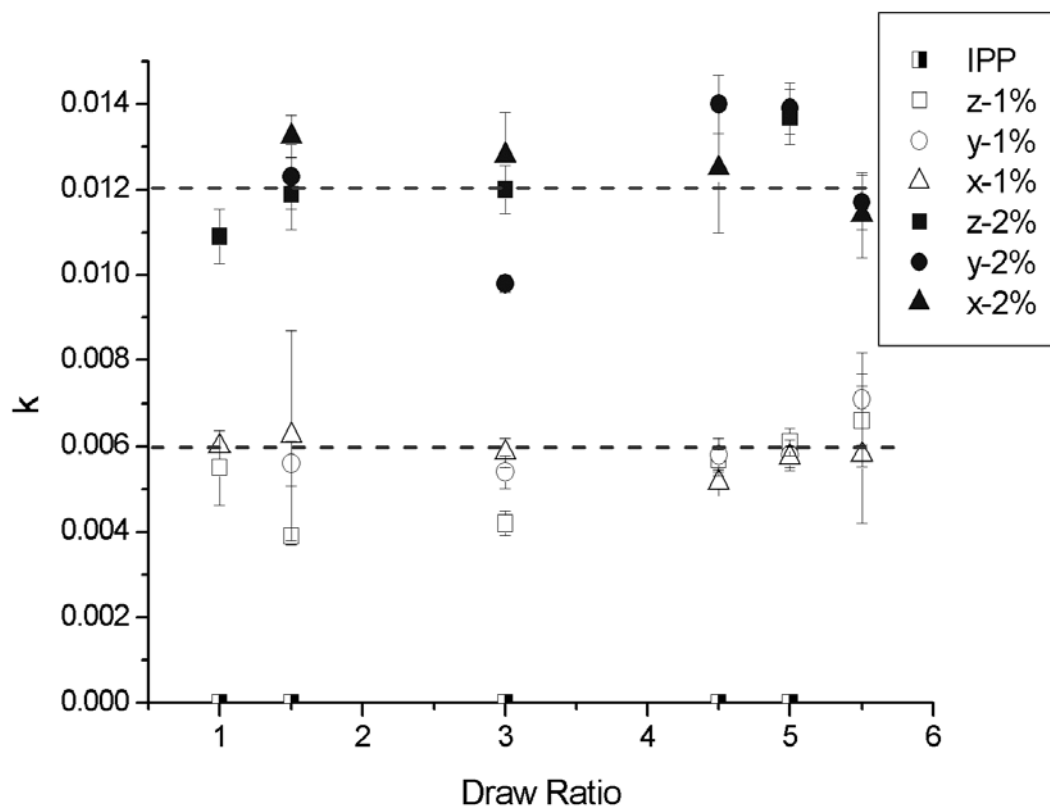
The pure IPP samples are transparent, so the extinction coefficient is very low (close to zero). However, the IPP-CB samples are black, such that the extinction coefficient matters. The three-dimensional extinction coefficients of the IPP-CB films were measured by the IRIA method. The results are plotted in Figure V-2. From Figure V-2, the extinction coefficients of the 2% carbon black films are twice the value of the 1% carbon black samples. This indicates that the extinction coefficient does relate to the carbon black distribution in the film. On the other hand, the extinction coefficients had no significant difference in all three dimensions, nor changes in value with draw ratio, so the carbon black remains random during the draw.

### 5.1.2 Refractive Index

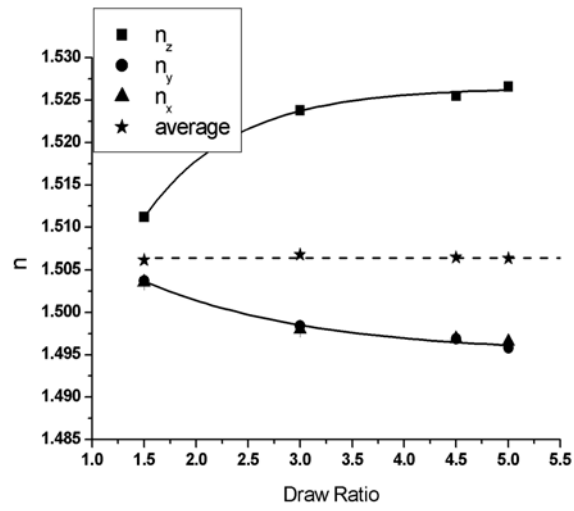
The three-dimensional refractive indices of the stretched IPP and IPP-CB films are plotted in Figure V-3. The refractive index can indicate axially, orientation and crystallinity. It will also be used in the discussion of birefringence in 5.4.1.

#### 5.1.2.1 Axiality

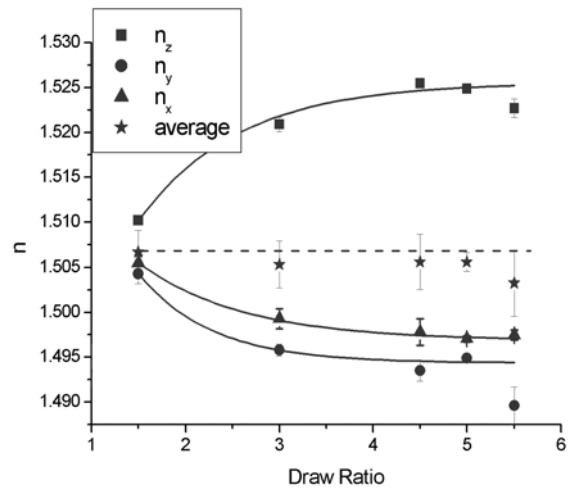
For all three series of stretched samples, the refractive index increases with draw ratio along the  $z$  direction (stretch direction), but decreases along the  $y$  and  $x$  directions. For IPP films, the refractive indices in the  $y$  and  $x$  directions overlap each other, so the films are uniaxial. However, for the IPP-CB samples, the refractive indices in the  $y$  direction and  $x$  direction film differ.



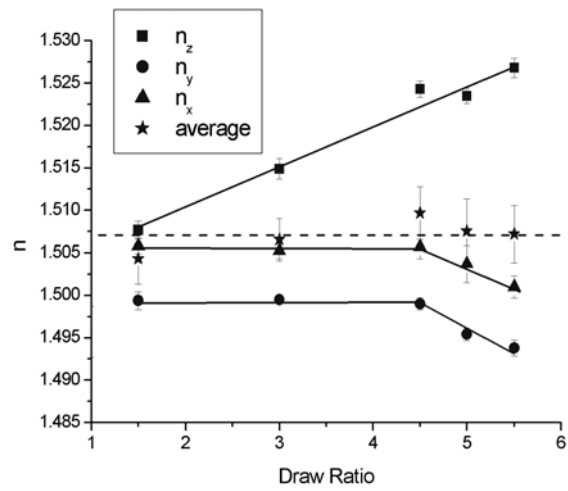
**Figure V-2.** The extinction coefficients of IPP-CB samples measured by the IRIA method (half-filled symbols -- pure IPP; unfilled symbols – IPP-1%CB; filled symbols – IPP-2% CB; z, y and x indicate three principal directions)



a. IPP



b. IPP-1% CB



c. IPP-2% CB

**Figure V-3.** The refractive index results of IPP and IPP-CB samples

**Table V-2.** The average refractive index and the crystallinity of IPP and IPP-CB films

DR	Average refractive index, $n_{ave}$					Crystallinity, $V_c$ (%)				
	IPP	1% CB	error	2% CB	error	IPP	1% CB	error	2% CB	error
1	1.4955	1.4940	0.0024	1.4957	0.0030	46.1	43.3	4.5	46.5	5.6
1.5	1.5062	1.5066	0.0024	1.5043	0.0030	65.9	66.9	4.5	62.4	5.5
3	1.5067	1.5053	0.0026	1.5066	0.0025	67.0	64.4	4.8	66.6	4.6
4.5	1.5064	1.5056	0.0031	1.5097	0.0031	66.4	64.9	5.7	72.4	5.7
5	1.5063	1.5056	0.0011	1.5075	0.0038	66.2	64.9	2.0	68.4	7.1
5.5		1.5033	0.0037	1.5072	0.0034	--	60.5	6.8	67.8	6.3

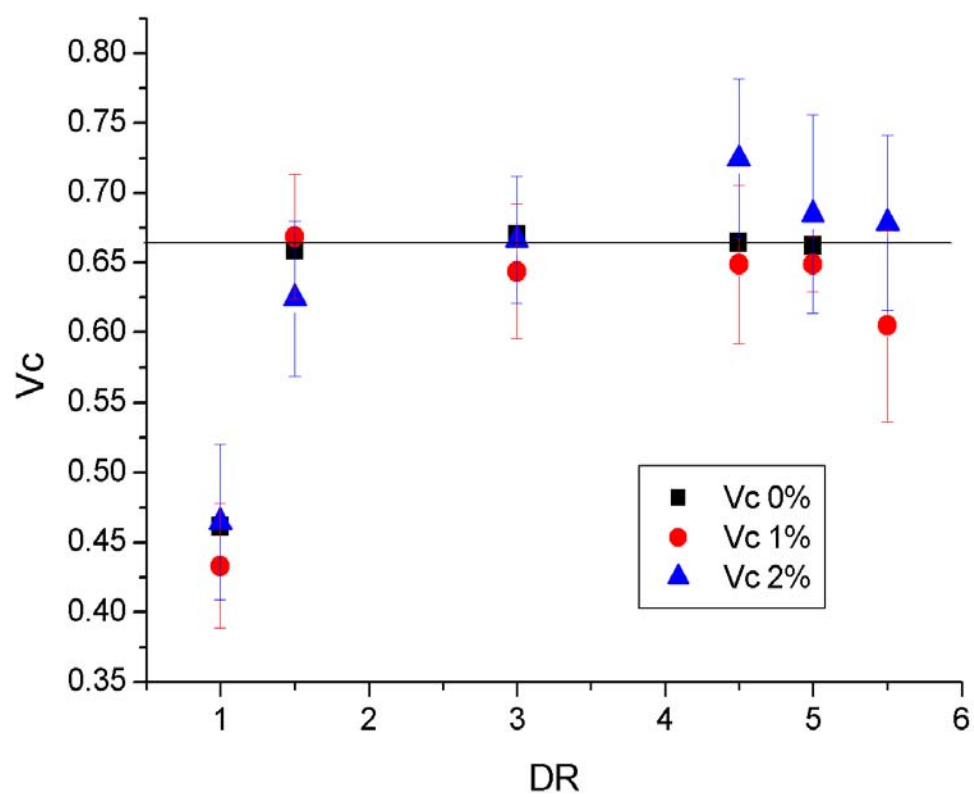
The gap between the refractive indices in the x and y direction increases with the carbon black concentration. This indicates that the presence of carbon black in the film influences deformation, so that the higher the carbon black content the greater the biaxial. In the IPP-CB sample, the refractive index in the y direction changed faster than in the x direction, so the film is easier to be oriented in the plane than through the plane.

#### 5.1.2.2 Orientation

The trends of the refractive index against the draw ratio also changed with the carbon black concentration. The more carbon black added into IPP, the higher the draw ratio required to reach a high orientation level. The biggest difference in the refractive index – draw ratio trend is at the 3X draw point. At this point, compared to the 1% CB and the neat IPP films, the refractive index in the z direction of the 2% carbon black sample is lower and also the changes in the y and x directions are smaller. Therefore the carbon black also delays the orientation of IPP.

#### 5.1.2.3 Crystallinity

Ignoring the effect of the low concentration of carbon black in the IPP-CB system, the crystallinity of polypropylene can be evaluated from the average refractive index. The results are shown in Table V-2 and Figure V-4. The error bars are based on the experimental uncertainties of the average refractive indices, which are the sum of the uncertainties in the three principal directions.



**Figure V-4.** The crystallinity of IPP and IPP-CB films changes with draw ratio



The results show that, at a given draw ratio, the crystallinity values of the IPP and the different carbon black concentration samples overlap each other within the error bars. This indicates that by adding carbon black, the crystallinity of IPP doesn't change in the IPP-CB system.

On the other hand, the stretched films have a higher crystallinity than the unstretched films. This is due to heating to the draw temperature during fabrication, which caused a further crystallization. The unstretched samples were cast at 38°C and the draw temperature was 100-110°C, thus the crystallinity of the unstretched samples is lower than the stretched samples. During the stretch, the crystallinity doesn't change, so the polypropylene didn't crystallize during the draw, even when carbon black was added.

## 5.2 LEVEL II–FTIR MEASUREMENT RESULTS

### 5.2.1 Effect of Carbon Black on the FTIR Spectra

Figure V-5, is the spectra of unstretched IPP and IPP-2% CB films. Carbon black has no absorbing peak from 700-1200  $\text{cm}^{-1}$  in the FTIR spectra, but only a background absorption. The effect of the carbon black in the background can be simply subtracted by the baseline adjustment. After the adjustment, the FTIR spectra only represent the properties of IPP in the IPP-CB films.

### 5.2.2 Unpolarized FTIR

The unpolarized FTIR was used to confirm the crystallinity of the IPP-CB samples evaluated from the average refractive index. The ratio of the peak heights of 998 and 973  $\text{cm}^{-1}$  were chosen to indicate the change of the crystallinity. Eq. III-20

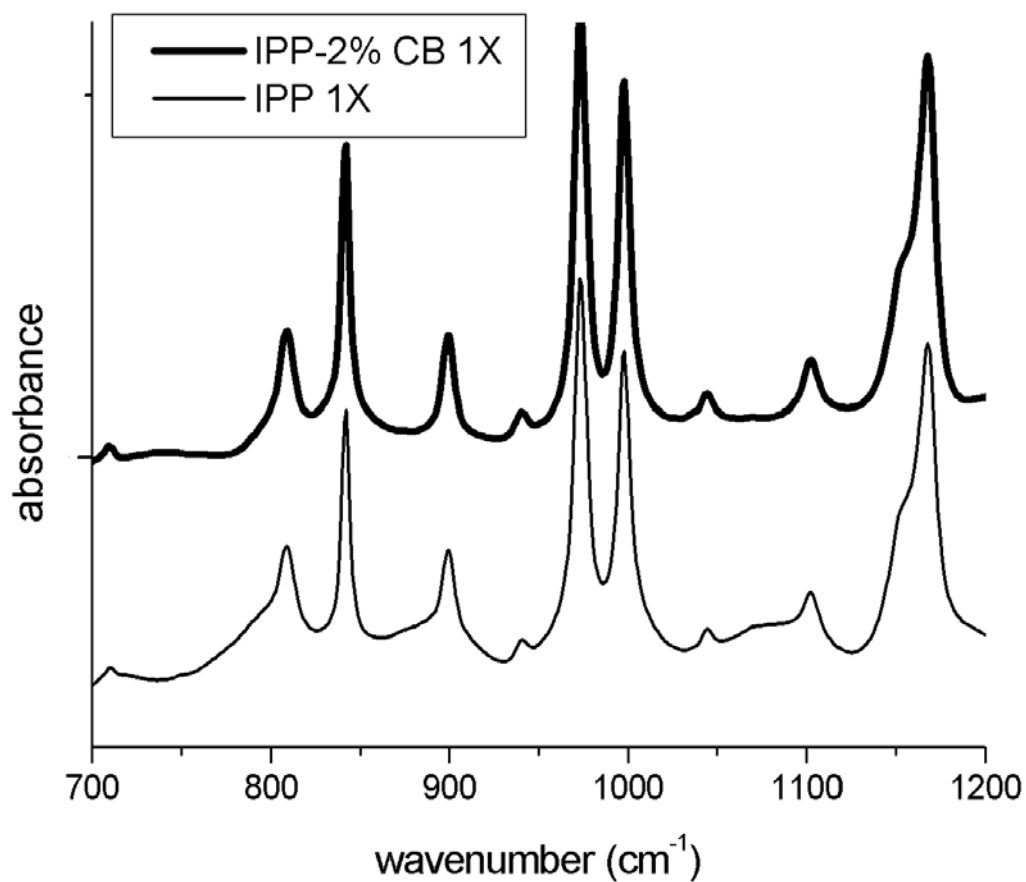
$$\left( \frac{A_c}{A_{ave}} = \frac{\epsilon_c}{\epsilon_{ave}} \frac{0.936V_c}{0.079V_c + 0.857} \approx \frac{\epsilon_c}{\epsilon_{ave}} \frac{0.936V_c}{0.857} = 1.09 \frac{\epsilon_c}{\epsilon_{ave}} V_c \right)$$

shows the ratio of absorbance bands of crystalline and average phases is a function of the crystallinity and the absorptivities of crystalline and average phases. The absorptivity of each phase is also changed with orientation three-dimensionally. When an unpolarized infrared beam was used, the absorptivity of a band is the average absorptivity around the angles. Therefore, the value of  $\epsilon_c/\epsilon_{ave}$  changes independent of the crystallinity with draw ratio. If the orientation is the same, the ratio can be used to compare the crystallinity. Table V-3 shows the ratios of the absorbance of 998 and 973  $\text{cm}^{-1}$  bands. Since for pure IPP, the crystallinity measurement from the average refractive index is a well-established method, the crystallinity of IPP from the average refractive index is

used as a reference for the crystallinity of the IPP-CB samples. Table V-2 and Figure V-4 show the crystallinity of the stretched IPP doesn't change with draw ratio. However in Table V-3, the ratios of the stretched polypropylene films decreased with draw ratio. Thus it predicts that the absorptivity ratio decreases with draw ratio.

In Table V-3, the ratio of the unstretched sample is lower than the 1.5X sample, so it indicates the crystallinity of the unstretched sample is lower than the stretched samples.

On the other hand, the Absorbance ratio doesn't significantly change with the carbon black concentration for a given draw ratio. If it is assumed that for the same draw ratio any orientation differences observed are negligible whatever the carbon black concentration then, by comparing the crystallinity of the IPP-CB samples with that of the pure IPP, it can be concluded that the carbon black has little effect on the crystallinity. This result agrees with the results from the average refractive index. Therefore, at low carbon black concentration, using the average refractive index to calculate for the crystallinity of IPP-CB samples is a reasonable method.



**Figure V-5.** The IRIA spectra of the IPP and IPP-2% CB unstretched samples

**Table V-3.** The ratio of the peak height of 998 and 973  $\text{cm}^{-1}$  of the IPP-CB sample measured by unpolarized FTIR

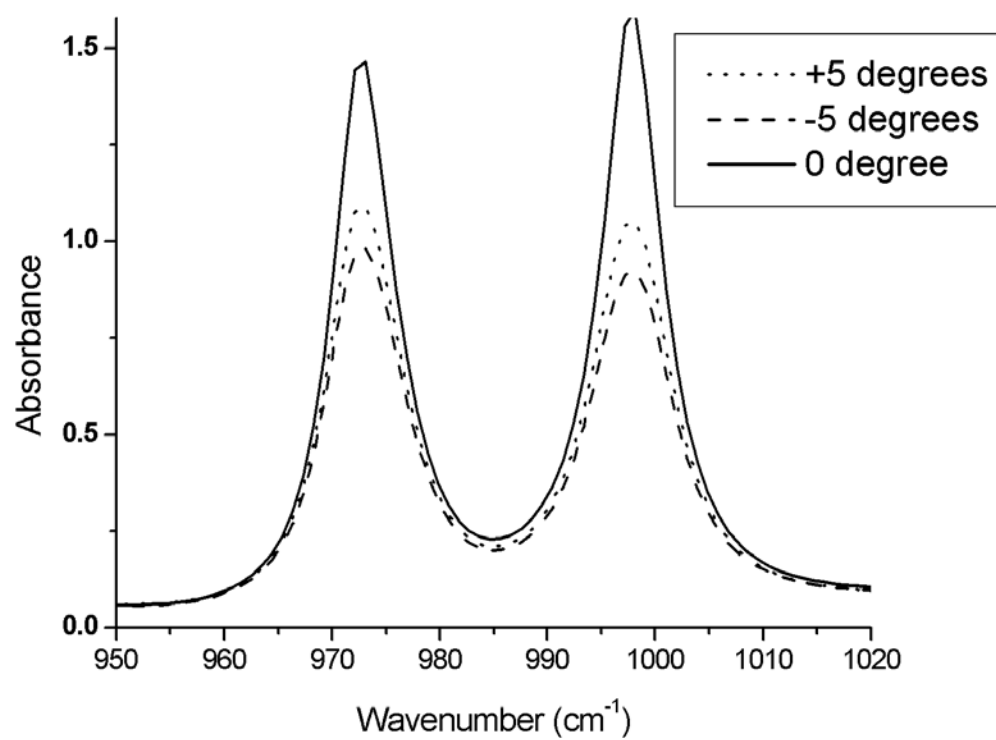
DR	IPP	IPP-1%CB	IPP-2%CB
1	0.75	0.72	0.79
1.5	0.94	0.94	0.91
3	0.84	0.85	0.85
4.5	0.79	0.79	0.73
5	0.76	0.77	0.71
5.5		0.63	0.68

### 5.2.3 Polarized FTIR

#### 5.2.3.1 Orientation Function

The polarized FTIR was used to analyze the orientation function of each phase. Before the measurements, a high draw ratio sample, IPP 5X, was measured to check the difference between the marked and real 0 degree positions. The IPP 5X draw film was measured at the marked 0, -5 and +5 degrees. The spectra were shown in Figure V-6. In Figure V-6, the absorbance at 0 degree is highest. The ratios of  $(A_0 - A_{-5}) / (A_{+5} - A_{-5})$  for 998  $\text{cm}^{-1}$  and 973  $\text{cm}^{-1}$  peaks are 5.1 and 4.9, respectively. By assuming the absorbance has a linear relationship with the angle in this small angle region, the difference of the marked 0 degree position and the real 0 degree position was found less than 1 degree.

In order to calculate the orientation functions of the crystalline and average phases of IPP, the dichroic ratios of the 998 (crystalline band) and 973  $\text{cm}^{-1}$  (average band) were evaluated by Eq. III-21. Then the orientation functions of the crystalline and average phases were obtained from Eq. III-22 and 23. In Eq. III-23, the transition moment angle is from Table III-4. For 2  $\text{cm}^{-1}$  resolution,  $\alpha_0$  for 973 and 988  $\text{cm}^{-1}$  is 14 and 15°, respectively. After knowing the orientation functions of the crystalline and average phases, the orientation function of the non-crystalline phase can be obtained by Eq. III-2. In Eq. III-2, the crystallinity is from Table V-2.



**Figure V-6.** The polarized FTIR spectra of IPP 5X sample at marked 0, -5 and +5 degrees

The results of the orientation functions of crystalline, non-crystalline and average phases are shown in Table V-4 and Figure V-7. The orientation functions of all three series of samples follow the same sequence that  $f_c > f_{ave} > f_{nc}$ . For all stretched films, the orientation function of crystalline phase increases rapidly at low draw ratios and then approached an upper limit at high draw ratios. The trends of the IPP-1% CB samples are similar to the IPP samples, but the trends of the IPP-2% CB samples are different with the other two sets of samples. For the IPP-2% CB samples, the orientation function of each phase increases more slowly than the other two series, especially at the 3X draw. It indicates that the carbon black frustrates the orientation of IPP in the IPP-CB system. This result agrees with the waveguide measurement result.

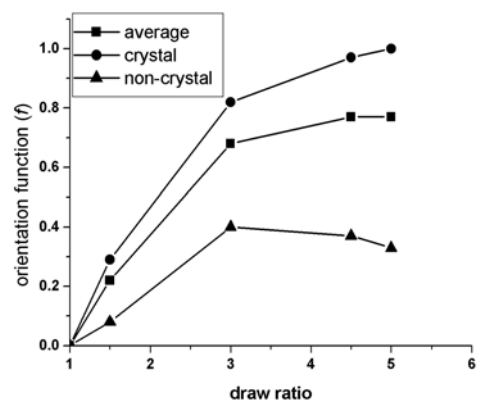
However, there are some problems in the results. First, at high draw ratios, the calculated orientation functions approach or even exceed the upper limit of the orientation function, 1. Indeed, it is very hard to make a perfectly oriented crystalline phase for polypropylene. Second, in the curve of the 2% carbon black non-crystalline phase, the orientation function keeps as a constant from 1.5 to 4.5X draw. These problems will be discussed in 5.4.2.

**Table V-4.** The results of dichroism calculations

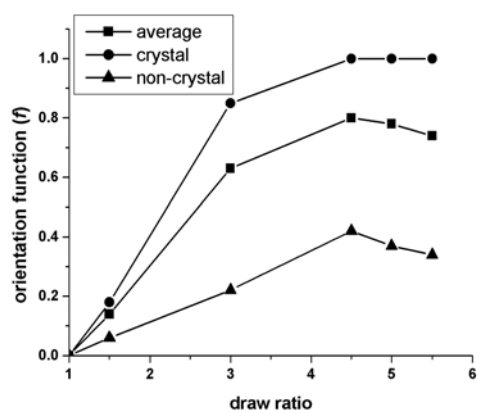
[C] %	DR	N <sub>ave</sub>	V <sub>c</sub> %	D		f		
				Ave.	Cry.	Ave.	Cry.	Amp.
0	1	1.4955	46.13	1.00	1.00	0	0	0
	1.5	1.5062	65.89	1.75	2.08	0.22	0.29	0.08
	3	1.5067	66.97	5.94	9.47	0.68	0.82	0.40
	4.5	1.5064	66.41	8.00	21.40	0.77	0.97	0.37
	5	1.5063	66.21	8.16	34.98	0.77	1*	0.33
1	1	1.4956	46.28	1.00	1.00	0	0	0
	1.5	1.5067	66.86	1.43	1.57	0.14	0.18	0.06
	3	1.5053	64.37	5.02	10.77	0.63	0.85	0.22
	4.5	1.5056	64.87	8.96	34.69	0.80	1*	0.42
	5	1.5056	64.91	8.39	28.82	0.78	1*	0.37
	5.5	1.5033	60.50	7.15	23.8	0.74	1*	0.34
2	1	1.4955	46.46	1.00	1.00	0	0	0
	1.5	1.5043	62.45	1.51	1.62	0.16	0.19	0.10
	3	1.5066	66.64	2.57	3.37	0.38	0.49	0.15
	4.5	1.5097	72.43	6.39	15.18	0.70	0.92	0.14
	5	1.5075	68.46	7.72	22.95	0.76	0.98	0.28
	5.5	1.5072	67.84	8.05	26.60	0.77	1.00	0.29

\* Calculated results are bigger than 1.

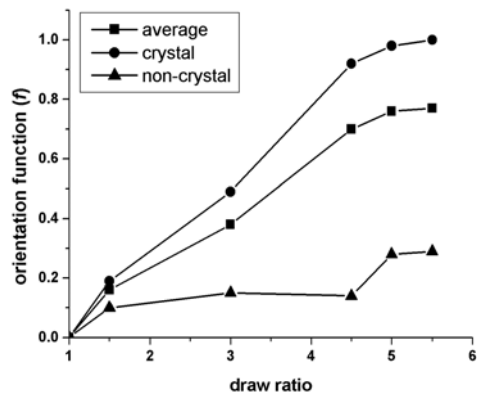




a. IPP



b. IPP-1% CB



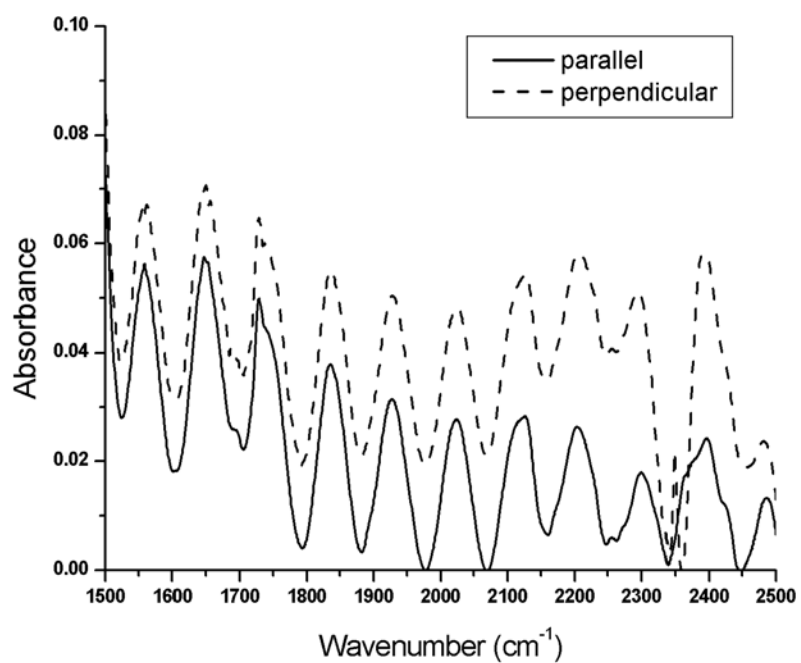
c. IPP-2% CB

**Figure V- 7.** The orientation functions of IPP and IPP-CB samples calculated from polarized FTIR results

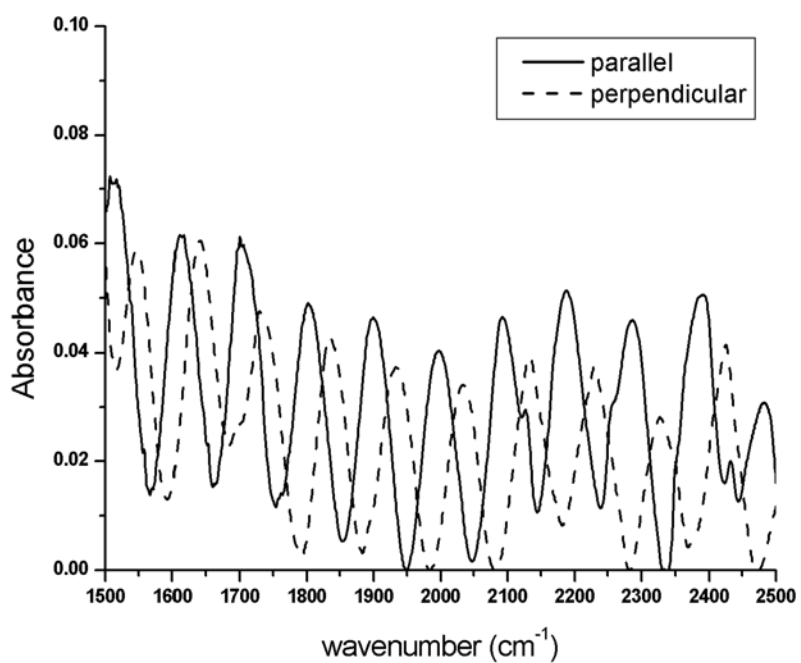
#### 5.2.3.2 Rolling Baseline

In this study, the rolling baseline is observed from the spectra of some IPP samples in the 1500-2500 wavenumber range. Figure V-8 shows two examples. One is for the unstretched film, for which the rolling baselines of parallel and perpendicular measurements are exactly in phase. The other is the 4.5X drawn film, in which the rolling baselines of the two polarized measurements are out of phase. The phase drift presents the difference in the refractive indices along the z and y axes of the film. The higher the draw ratio, the larger the difference in the refractive indices. So the rolling baseline is a qualitative method for comparing the birefringence.

In Figure V-8, the deformation of the rolling baseline curve is observed. This may be due to surface variations of the sample and/or the resolution of the FTIR equipment. The deformation makes the peak position hard to determine. Therefore the rolling baselines could not be used as a quantitative measurement in this research.



a. IPP 1X



b. IPP 4.5X

**Figure V-8.** The rolling baselines of the IPP samples

### 5.3 LEVEL III—X-RAY MEASUREMENT RESULTS

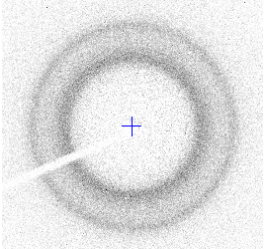
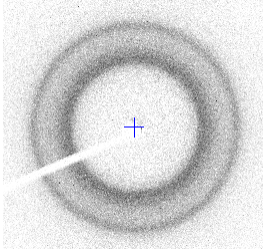
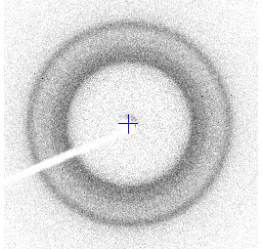
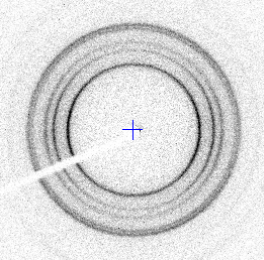
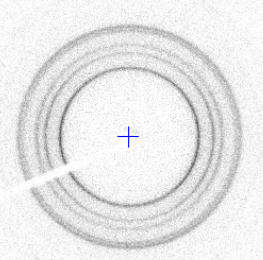
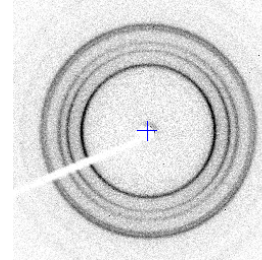
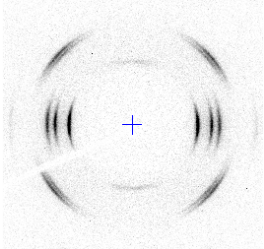
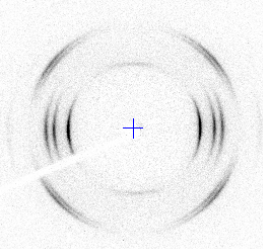
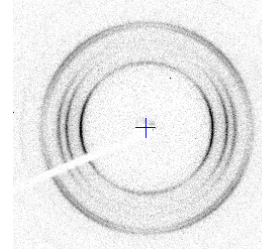
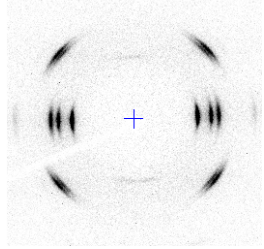
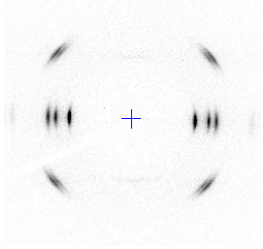
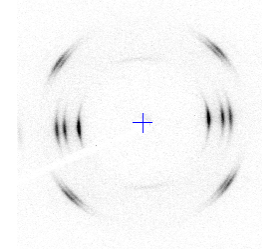
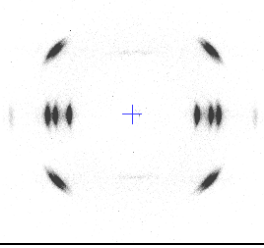
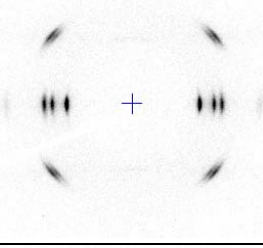
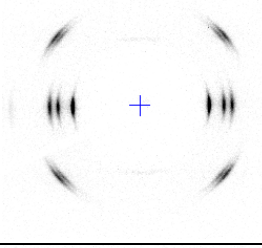

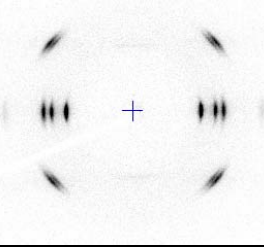
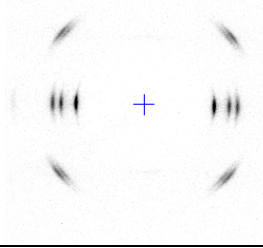
The X-ray diffraction patterns are shown in Figure V-9. The background has been subtracted by taking off the intensity from the air measurement with the same exposure time. The contrast of the images was adjusted, so some images have dim backgrounds. In Figure V-10, the intensity curves were integrated along the azimuthal angles and plotted against  $2\theta$ .

#### 5.3.1 Crystal Form

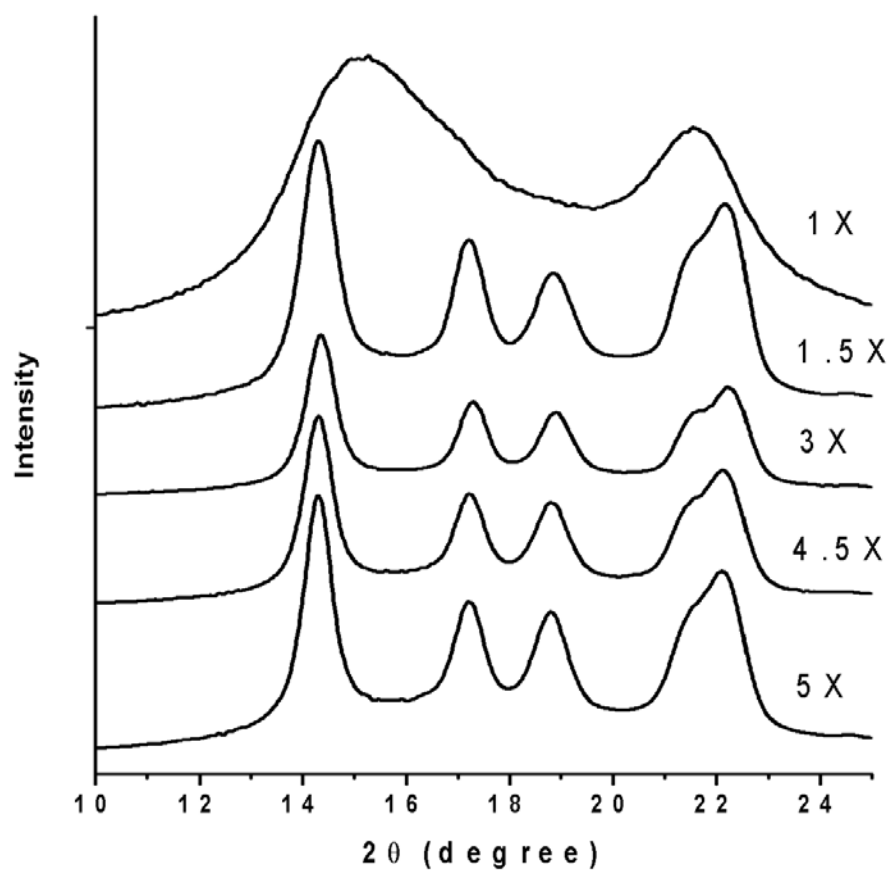
In Figure V-10, all of the stretched samples have a similar diffraction curve to the 1.5X samples, but the unstretched samples have a different curve shape. Compared to Figure III-15, the stretched samples diffraction pattern shows the typical  $\alpha$ -form crystal structure of IPP. Referring to Figure III-16, the crystals in the unstretched sample have more defects. From Figure III-16, we see that the diffraction curves for the stretched samples look like those quenched at high temperature, while the cast unstretched samples in Figure V-10 look like the low temperature cast film patterns in Figure III-16.

The intensity curves of the three unstretched films are compared in Figure V-11. A slight difference was found in the three curves. For the curve of the unstretched IPP, the two wide peaks are smooth, but by adding carbon black into IPP, there are some humps on the shoulder of the wide peaks and the peak positions of the two wide peaks also shift to both sides. These phenomena are more remarkable in the higher carbon black concentration (2%) sample than the lower carbon black concentration (1%)

sample. Compared to Figure V-11, these humps indicate more perfect crystals. Therefore the carbon black can improve the perfection of the crystals of IPP. The perfection has no significant difference in the stretched samples. The reason is that, at the high drawn temperature, the sample has enough time to achieve well-formed  $\alpha$ -crystal. For comparison, see Figure III-16.

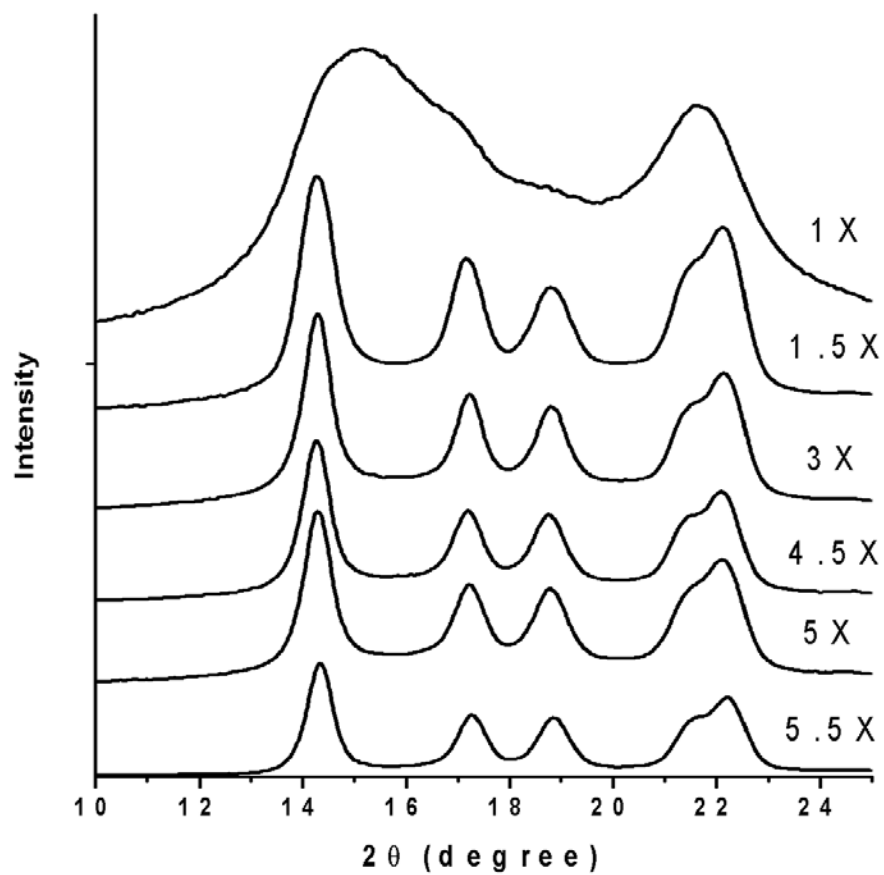
	0%	1%	2%
1X			
1.5X			
3X			
4.5X			
5X			
5.5X			

**Figure V-9.** The diffraction images of IPP and IPP-CB samples



a. IPP

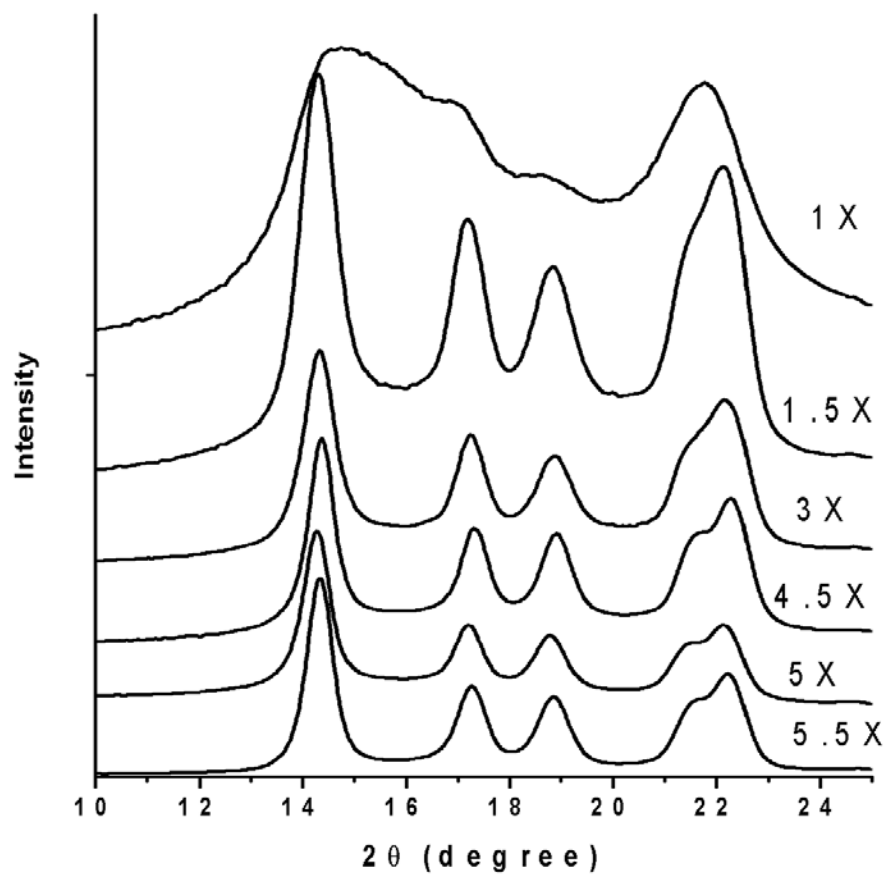
**Figure V-10.** The diffraction intensity curves of IPP and IPP-CB samples (the intensity values are not in scale)



b. IPP-1% CB

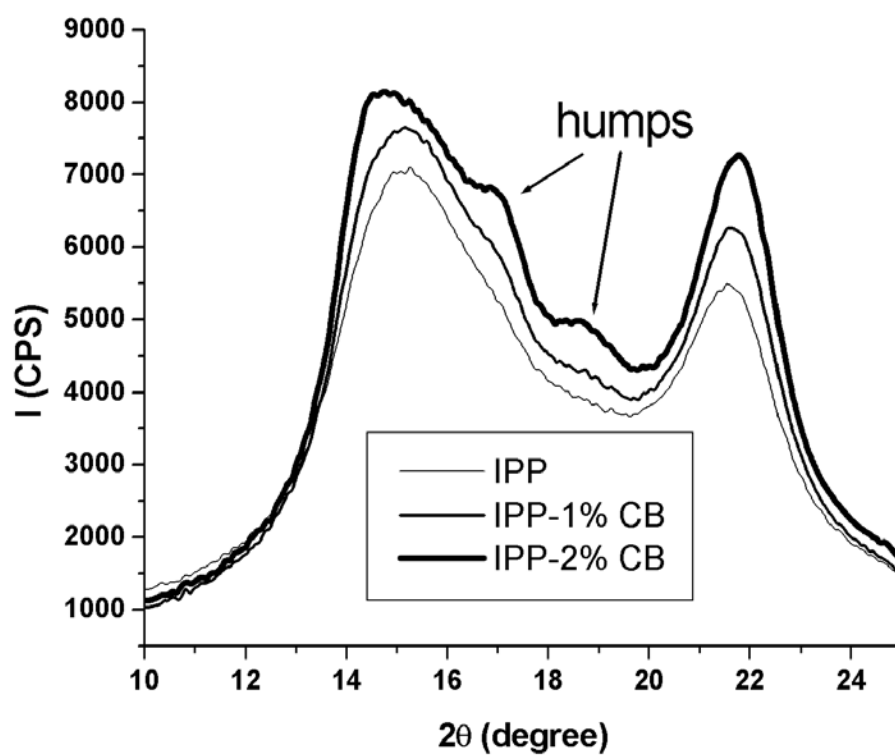
**Figure V-10 (Cont'd).** The diffraction intensity curves of IPP and IPP-CB samples (the intensity values are not in scale)





c. IPP-2% CB

**Figure V-10 (Cont'd).** The diffraction intensity curves of IPP and IPP-CB samples (the intensity values are not in scale)



**Figure V-11.** The diffraction intensity curves of unstretched IPP and IPP-CB samples

### 5.3.2 2 $\theta$ value

The 2 $\theta$  values are found by fitting the stretched sample curves. Figure V-12 shows an example of the peak fitting, using film sample IPP 3X film. The baseline is only a model equation, not the real diffraction curve of the noncrystalline phase. The 2 $\theta$  value of each peak (Table V-5) doesn't change significantly with the CB concentration or draw ratio, which also proves that carbon black has no effect on the crystal form. The experimental 2 $\theta$  values of the (040) reflection are slightly different from the literature value. The reason may be system alignment.

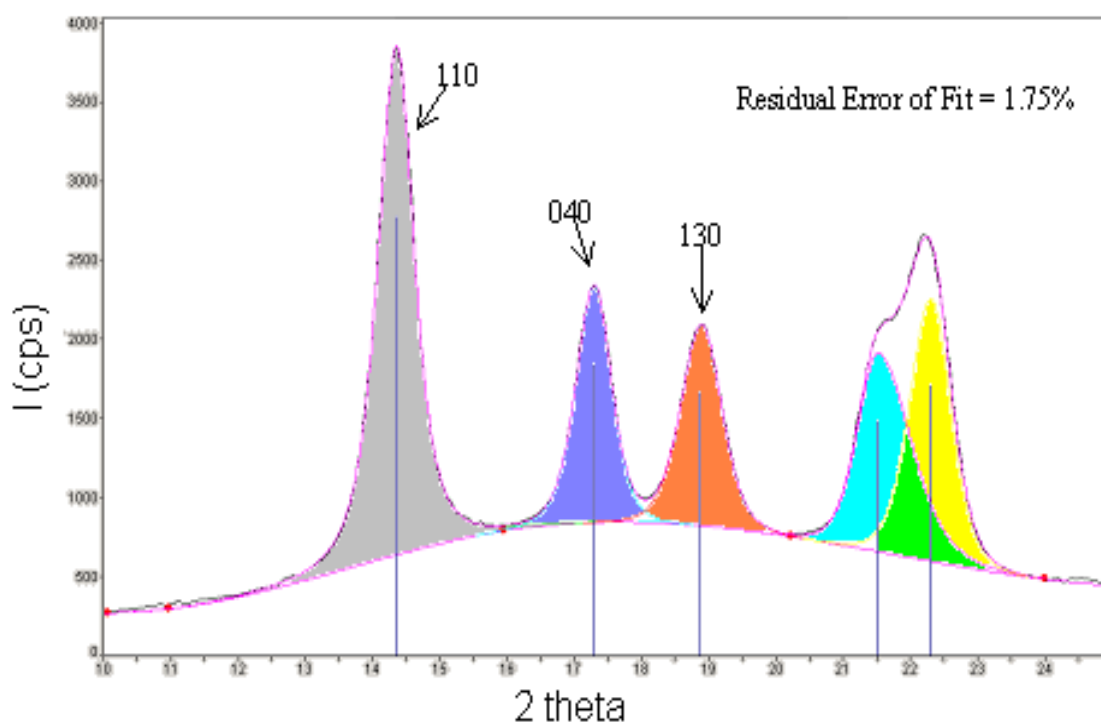
### 5.3.3 Orientation Function

Figure V-9 can be looked as snapshots of the stretching procedure. In Figure V-9, the diffraction patterns of the unstretched samples are rings which broke into arcs during stretching. The length of the arc indicates the orientation function of the IPP crystal. The shorter the arc, the higher the orientation. The images reveal the orientation processes of IPP-2% CB samples are slower than the other two series, especially at 3X. These results match the waveguide and FTIR results.

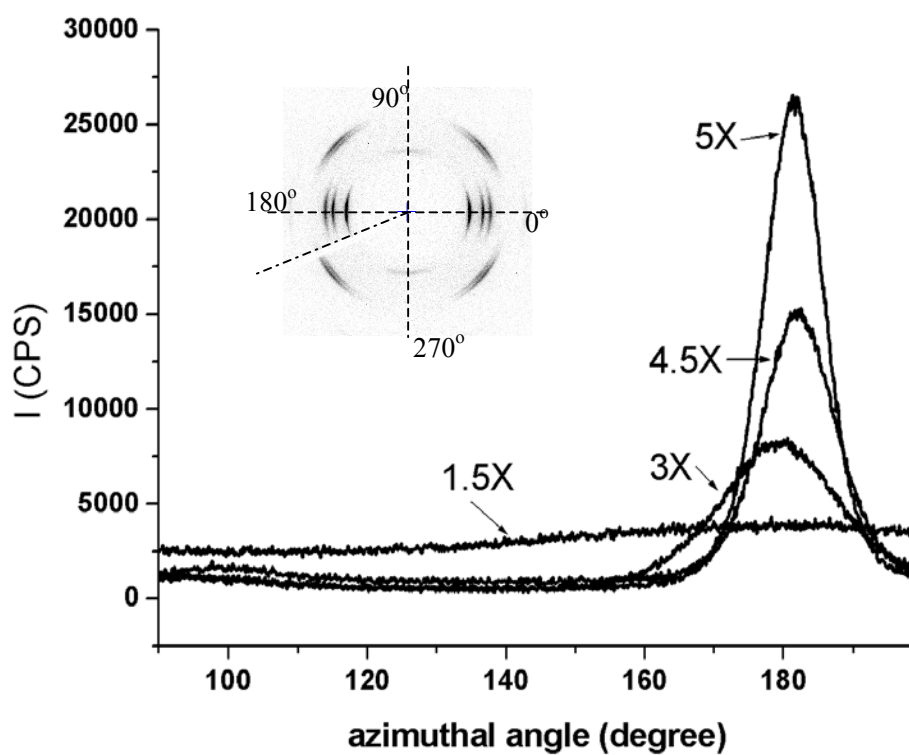
In the quantitative calculation,  $\langle \cos^2(\Phi_{110}) \rangle$  and  $\langle \cos^2(\Phi_{040}) \rangle$  were used to calculate the orientation function of the crystal along the stretch direction.  $\langle \cos^2(\Phi_{hkl}) \rangle$  was obtained from integrating the intensities at 2 $\theta$  of the (h k l) plane around the azimuthal angles by Eq. III-29 and Eq. III-30. Figure V-13 shows the intensity of the azimuthal scan curve of the (110) plane of the IPP samples as it changes with draw ratio.

**Table V-5.** The 2 $\theta$  values of 110 and 040 peaks

Plane		110			040		
[CB]		0%	1%	2%	0%	1%	2%
Literature. Value		14.13 $\pm$ 0.14			16.91 $\pm$ 0.13		
Exp. Value	1.5X	14.17	14.14	14.15	17.07	17.03	17.05
	3X	14.08	14.15	14.19	17.14	17.07	17.10
	4.5X	14.17	14.14	14.24	17.07	17.06	17.18
	5X	14.17	14.17	14.15	17.06	17.09	17.07
	5.5X		14.21	14.17		17.14	17.13

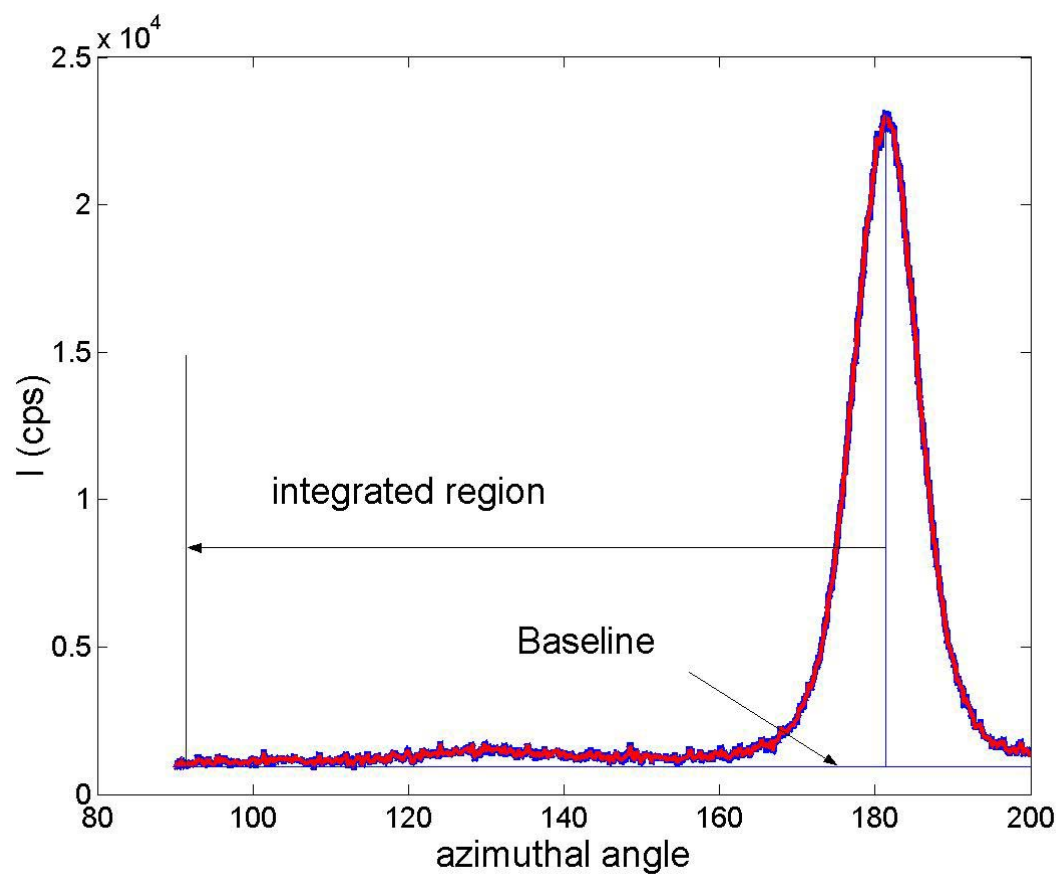


**Figure V-12.** The example of peak fitting (the sample is IPP 3X draw)



**Figure V-13.** The azimuthal curve of (110) plane of IPP films with different draw ratios

It shows that the baselines of the highly drawn samples can be taken by the lowest intensity in the curve, but for low oriented samples, the real baselines are lower than their minimum intensity. This problem has already been discussed in 3.2.3.4. In the present research, for the highly orientated samples (except all 1.5X and IPP-2% CB 3X samples), the baselines were chosen as the minimum intensity after smoothing the curves 5 times by the Adjacent Averaging Method with 5 points. For low oriented samples, all 1.5X samples and the IPP-2% CB 3X sample, the real baseline is lower than the minimum reflection intensity. Since the highly orientated sample has a more reliable baseline, the baseline of the IPP 5X film was used to estimate the baselines of these low oriented sample intensity curves. Figure V-12 shows that the peak position may be a little off from the horizontal direction, so the peak was chosen from the maximum intensity position after smoothing for all samples, except 1.5X samples. For the 1.5X sample, it is very hard to tell the peak position, so the referred horizontal direction (180 °C) was used as the peak position. Figure V-14 shows an example of the treatment of the azimuthal curves of highly oriented sample. The example is the IPP 5X sample (110) plane. The red curve is the smoothed curve and the vertical and horizontal lines indicate peak position and baseline, respectively.



**Figure V-14** The azimuthal curve of IPP 5X film (110) plane

The orientation functions of the crystal are calculated by Eq III-31. The results are listed in Table V-6.

**Table V-6.** C-axis orientation functions calculated from x-ray diffraction of the IPP and IPP-CB samples.

[CB]	$\langle \cos^2 \Phi \rangle$						$f_c$		
	0%		1%		2%		0%	1%	2%
plane	110	040	110	040	110	040			
1.5X	0.2739	0.2444	0.2893	0.2602	0.2883	0.2640	0.218	0.171	0.168
3X	0.0693	0.0654	0.0989	0.0906	0.1861	0.1604	0.797	0.714	0.476
4.5X	0.0497	0.0621	0.0416	0.0554	0.0596	0.0673	0.834	0.856	0.811
5X	0.0462	0.0564	0.0408	0.053	0.0491	0.0688	0.847	0.861	0.826
5.5X			0.0423	0.0623	0.0263	0.0354		0.846	0.909

#### 5.3.4 Crystallinity

Because of the lack of the diffraction pattern of the amorphous polypropylene, it is hard to obtain the correct baseline for crystallinity calculation. Therefore in this present research, the crystallinity was not calculated from the x-ray diffraction.



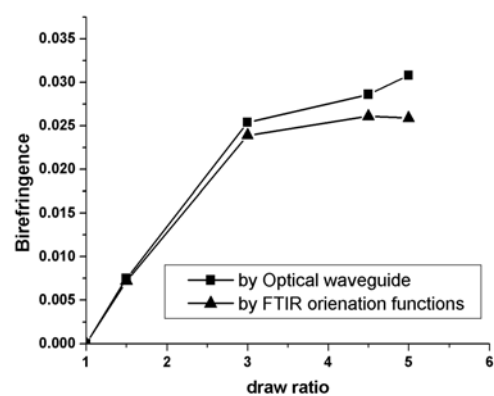
## 5.4 RELATIONSHIP BETWEEN EACH LEVEL

Figure IV-2 shows the relationship between each structure level. The birefringence is the channel between the first and the second levels and the orientation function of crystalline phase is the channel between the second and the third levels. Since the samples were measured at the same place by the nondestructive methods, the results should agree with each other.

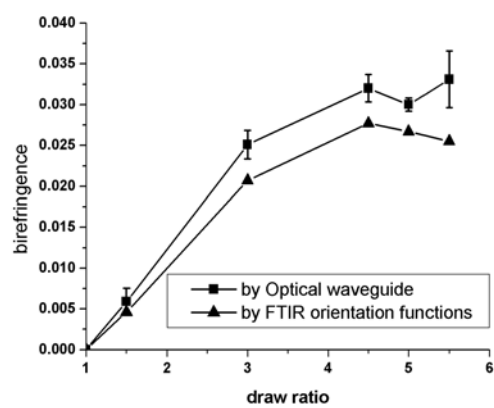
### 5.4.1 Level I & Level II – Birefringence

Birefringence can be obtained from either the experimental determined refractive index (Eq. III-8) or calculated from the orientation functions and the intrinsic birefringence of each phase (Eq. III-10). Since FTIR provides the in-plane information, when the orientation functions from FTIR are used to calculate the birefringence, the results should match the in-plane birefringence,  $\Delta_{zy}$ , from the waveguide measurements. In Eq. III-8, the refractive indices are from the waveguide measurement results (Table V-1). In Eq. III-10, the orientation function of each phase, the crystallinity and the intrinsic birefringence are from Table V-2, Table V-4 and Table III-1, respectively.

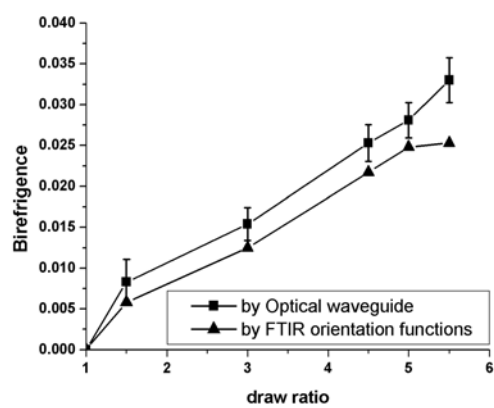
The birefringences from the two methods are plotted together in Figure V-15. For all three sets of samples, the trends of the birefringence of the two methods are same, but the values from Eq. III-10 are always lower than the results from the waveguide measurements. This problem will be discussed in 5.4.3



a. IPP



b. IPP-1% CB



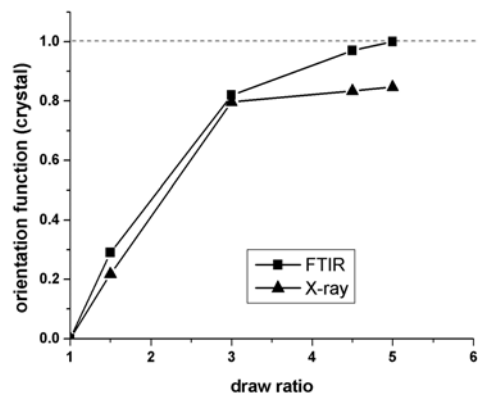
c. IPP-2% CB

**Figure V-15.** Compare the birefringence values measured by the waveguide methods and calculated from polarized FTIR results.

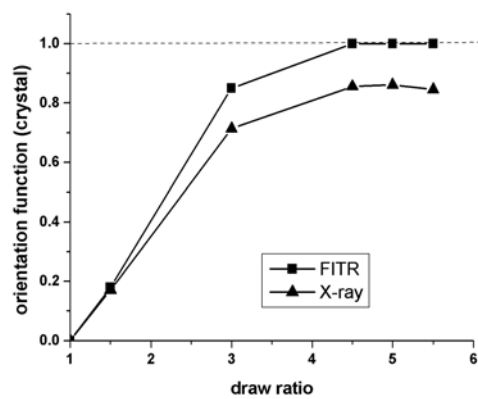
#### 5.4.2 Level II & Level III—Orientation Function Of the Crystalline Phase

The orientation function of crystalline phase is obtained from both FTIR (Table V-4) and X-ray (Table V-6). Figure V-14 plots them together. Similar with Figure V-13, they show same trends, but there is a gap between the curves by the two methods.

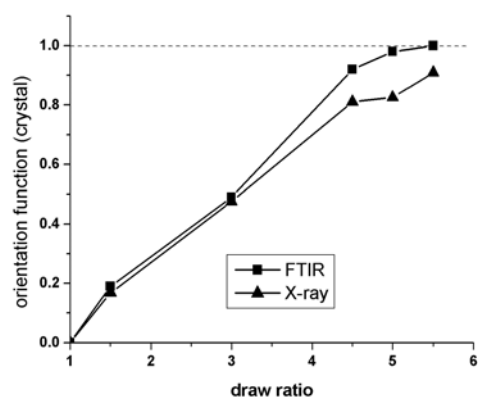
As mentioned in 5.2.3.1, the orientation function of the crystalline phase by FTIR is too high for highly drawn samples. Compared to the FTIR results, the X-ray results are more reasonable. Since in FTIR the orientation function of the crystalline phase was calculated from Eq. III-22, the intrinsic dichroism is very important for the calculation. Eq. III-22 also shows if the orientation function of crystalline phase can be obtained from another independent method, by fitting  $f_c$  vs.  $(D-1)/(D+2)$  of  $998\text{ cm}^{-1}$  band with a linear equation,  $y=ax$ , the slope will be  $(D_0+2)/(D_0-1)$ . Then  $D_0$  can be determined. X-ray diffraction is one of the independent methods for determining  $f_c$ . So in order to check  $D_0$ ,  $f_c$  from x-ray is plotted against  $(D-1)/(D+2)$  of  $998\text{ cm}^{-1}$  band from FTIR in Figure V-17. Eq. III-23 shows that  $D_0$  can be a value from 0 to infinity, therefore the value of the slope,  $(D_0+2)/(D_0-1)$ , could be a number from negative infinity to  $-2$  or  $1$  to infinity. In Figure V-14, the fitted slope is  $0.97 \pm 0.04$  with 99.9% confident limit. So the real slope should be  $1$ , for which  $D_0$  is infinity and the transition moment angle  $\alpha_v$  of  $998\text{ cm}^{-1}$  band is  $0^\circ$ . After the correction of the transition moment angle from  $15^\circ$  to  $0^\circ$ , the orientation function of each phase is plotted again in Figure V-18. All values are in the reasonable region. Instead of remaining a constant, the orientation function of noncrystalline phase of the IPP-2% CB sample increased from  $1.5X$  to  $4.5X$ . The shape of the trend doesn't change.



a. IPP

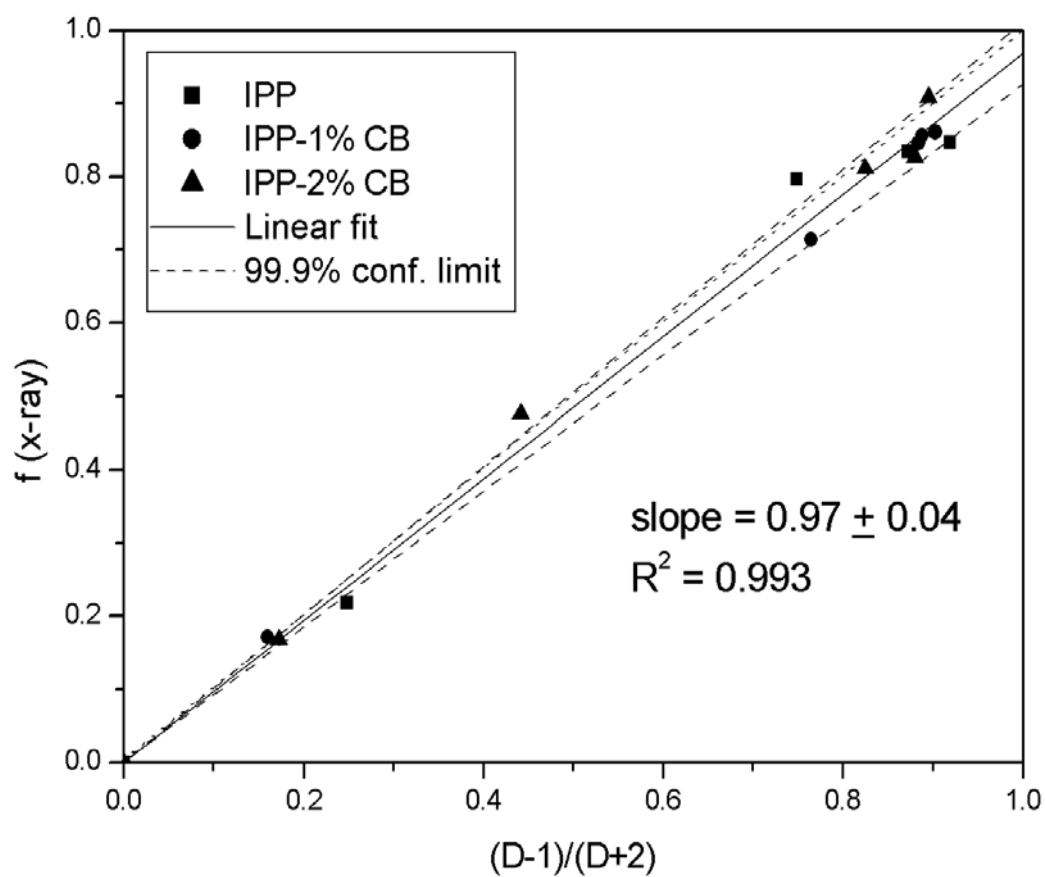


b. IPP-1% CB

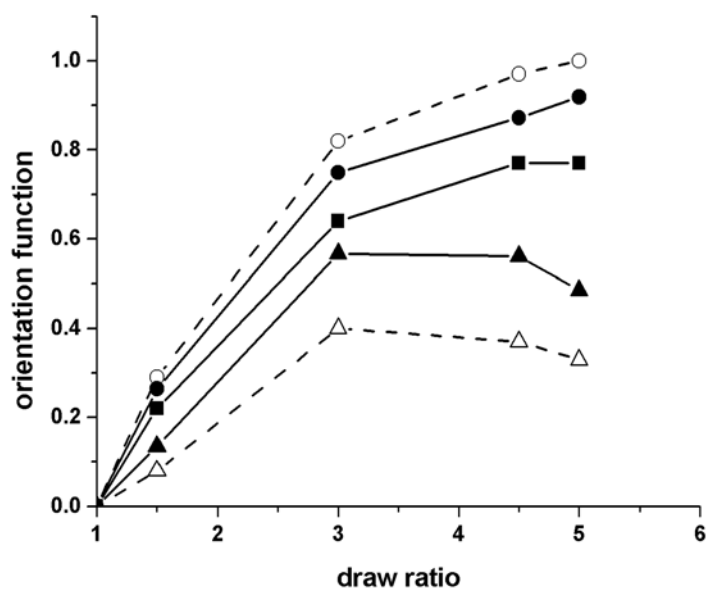


c. IPP-2% CB

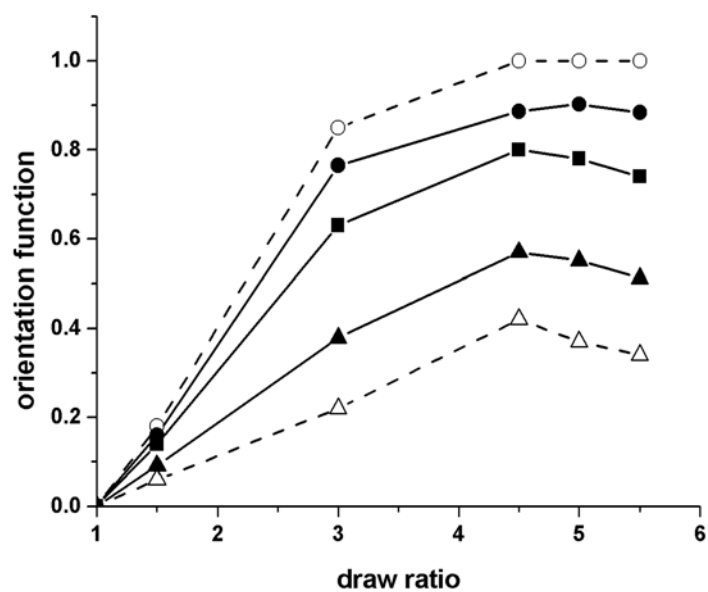
**Figure V-16.** The orientation function of crystalline phase of IPP measured by FTIR and X-ray diffraction



**Figure V-17.** The linear fit of the orientation function of crystalline phase from X-ray against  $(D-1)/(D+2)$

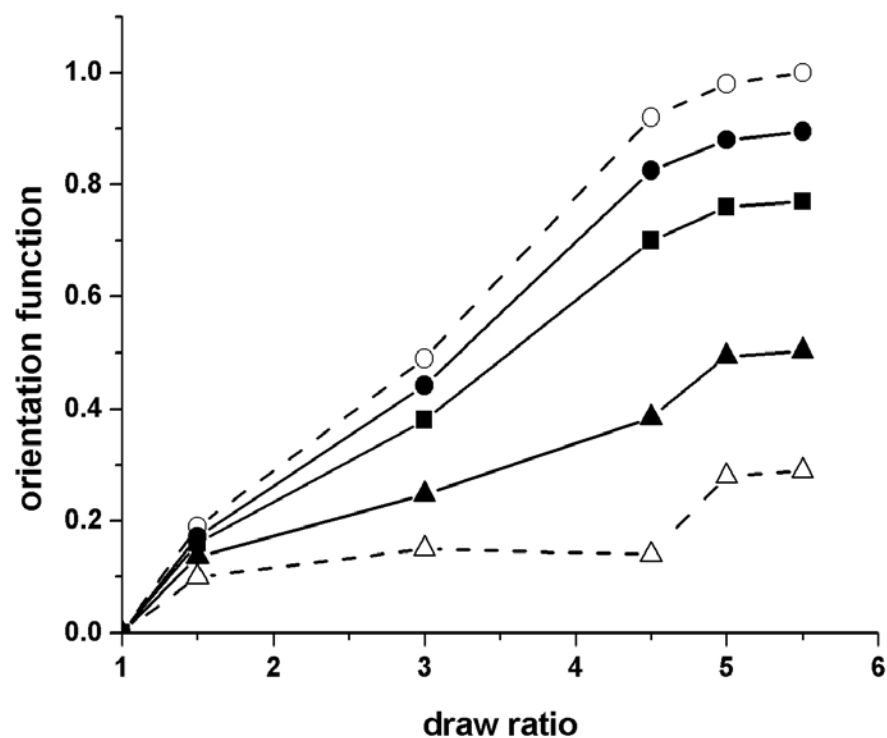


a. IPP



b. IPP-1% CB

**Figure V-18.** The orientation function of each phase before and after correction [ $\blacksquare$ - $f_{ave}$  with  $\alpha_v$  ( $973\text{cm}^{-1}$ ) =  $14^\circ$ ;  $\bullet$ - $\alpha_v$  ( $998\text{cm}^{-1}$ ) =  $0^\circ$ ;  $\blacktriangle$ - $f_{nc}$  with  $\alpha_v$  ( $998\text{cm}^{-1}$ ) =  $0^\circ$ ;  $\circ$ - $f_c$  with  $\alpha_v$  ( $998\text{cm}^{-1}$ ) =  $15^\circ$ ;  $\triangle$ - $f_{nc}$  with  $\alpha_v$  ( $998\text{cm}^{-1}$ ) =  $15^\circ$ ]



c. IPP-2%CB

**Figure V-18 (cont'd)** The orientation function of each phase before and after correction. [■- $f_{ave}$  with  $\alpha_v$  ( $973\text{cm}^{-1}$ ) =  $14^\circ$ ; ●- $\alpha_v$  ( $998\text{cm}^{-1}$ ) =  $0^\circ$ ; ▲- $f_{nc}$  with  $\alpha_v$  ( $998\text{cm}^{-1}$ ) =  $0^\circ$ ; ○- $f_c$  with  $\alpha_v$  ( $998\text{cm}^{-1}$ ) =  $15^\circ$ ; △- $f_{nc}$  with  $\alpha_v$  ( $998\text{cm}^{-1}$ ) =  $15^\circ$  ]

### 5.4.3 Overall

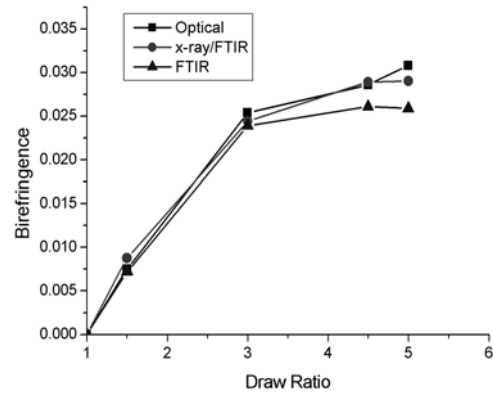
In order to check the correction on the transition moment angle, the birefringence was calculated again. During the correction, the orientation functions of the crystalline phase from the FTIR and the x-ray are treated equivalently. Therefore, instead of using the orientation function of the crystalline phase from the FTIR, we can use orientation function of crystalline phase from the x-ray combined with the orientation function of the average phase from FTIR to calculate the orientation function of the noncrystalline phase.

The in-plane birefringence was then recalculated using this new orientation function of the noncrystalline phase and orientation function of the crystalline phase from X-ray. This method is called the “X-ray/FTIR combined method”.

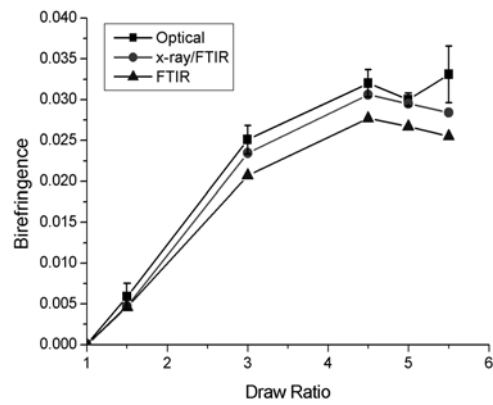
Figure V-19, the birefringences from the optical waveguide, the new combined method and the old FTIR results are compared. The new combined method (X-ray/FTIR) curve is much closer to the optical waveguide curve (Optical) than is the old FTIR (FTIR) curve. Almost all the points of the combined method are in the error bars of the waveguide results. This proves that the problems of the gap in Figure V-15 and Figure V-16 are all due to the intrinsic dichroism. On the other hand, by doing this, all methods were connected together, and the results inherently agree with each other.

The updated transition moment angle value of the  $998\text{cm}^{-1}$  crystalline band, 0 degree, matches the experimental results in this research and the results are listed in Table V-7, but in order to confirm the value, more independent data may be required.

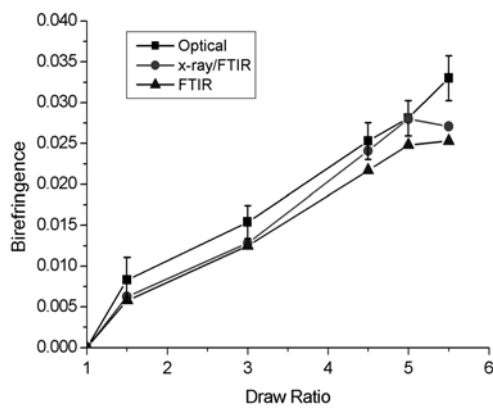




a. IPP



b. IPP-1% CB



c. IPP-2% CB

**Figure V-19.** The birefringence results from different method.

**Table V-7** Orientation functions of c-axis calculated from x-ray diffraction of IPP and IPP-CB samples after correction

[CB]	DR	$f_c$		$f_{nc}$		$\Delta_{zy}$		
		x-ray	998 (0°)	x-ray	998 (0°)	x-ray	998 (0°)	Waveguide
0	1X	0	0	0	0	0	0	0
	1.5X	0.218	0.264	0.225	0.135	0.0088	0.0078	0.0075
	3X	0.797	0.749	0.448	0.567	0.0244	0.0256	0.0254
	4.5X	0.834	0.872	0.635	0.561	0.0289	0.0281	0.0286
	5X	0.847	0.919	0.627	0.486	0.0290	0.0275	0.0308
1%	1X	0	0	0	0	0	0	0
	1.5X	0.171	0.160	0.070	0.092	0.0047	0.0049	0.0059±0.0016
	3X	0.714	0.765	0.471	0.379	0.0234	0.0224	0.0251±0.0018
	4.5X	0.856	0.887	0.619	0.570	0.0306	0.0293	0.0320±0.0017
	5X	0.861	0.903	0.629	0.552	0.0295	0.0287	0.0300±0.0008
	5.5X	0.846	0.884	0.570	0.512	0.0284	0.0277	0.0331±0.0035
2%	1X	0	0	0	0	0	0	0
	1.5X	0.168	0.172	0.142	0.136	0.0063	0.0062	0.0083±0.0028
	3X	0.476	0.442	0.180	0.248	0.0128	0.0135	0.0154±0.002
	4.5X	0.811	0.825	0.423	0.385	0.0241	0.0238	0.0253±0.0022
	5X	0.826	0.880	0.610	0.494	0.0280	0.0269	0.0281±0.0022
	5.5X	0.909	0.895	0.474	0.503	0.0271	0.0274	0.0330±0.0028

## CHAPTER VI

### CONCLUSIONS

The procedure for the optical characterization of anisotropic isotactic polypropylene with nano carbon black pigment system was successfully established.

The optical constants of the IPP-CB system were obtained by the knee method and IRIA method. The refractive indices of IPP and IPP-CB samples increase in the z direction with the draw ratios, but decrease in the other two principal directions. However the trends are different with various carbon black concentrations. During stretching, the straight IPP films are uniaxial, whereas by adding the carbon black, the films become biaxial, while the carbon black remains random. The 2% CB sample is much harder to orient. The crystallinity values calculated from the average refractive index shows the carbon black has no effect on the crystallinity of IPP in the IPP-CB system.

The unpolarized FTIR verified that the CB didn't change the crystallinity significantly. The orientation function of each phase at in the plane direction of the sample was calculated from the polarized FTIR dichroic ratios. It shows that the 2% CB samples are much harder to orient than the other two series. The result matched the optical measurement results.

The x-ray diffraction shows that the presence of the carbon black didn't change the

crystal form of the isotactic polypropylene. However, the addition of carbon black improves the crystal perfection when quenched at low temperature. The diffraction patterns show that the 2% CB sample is harder to orient, which agreed with the conclusions from the optical waveguide and FTIR measurements. The orientation function from x-ray was also used to correct the transition moment angle of the  $998\text{cm}^{-1}$  band in FTIR. After the correction the results of the three methods are better matched.

Overall, in the present CB-IPP system, the carbon black has little effect on crystallinity and the crystal form of polypropylene, but has some effect on the perfection of the crystal; by adding carbon black to the polypropylene, the film gets harder to orient and changes from uniaxial to biaxial.

## **PART B**

### **OPTICAL CHARACTERISTICS OF COMPRESSION MOLDED POLY (METHYL METHACRYLATE) WITH NANO INDIUM TIN OXIDE**

## CHAPTER VII

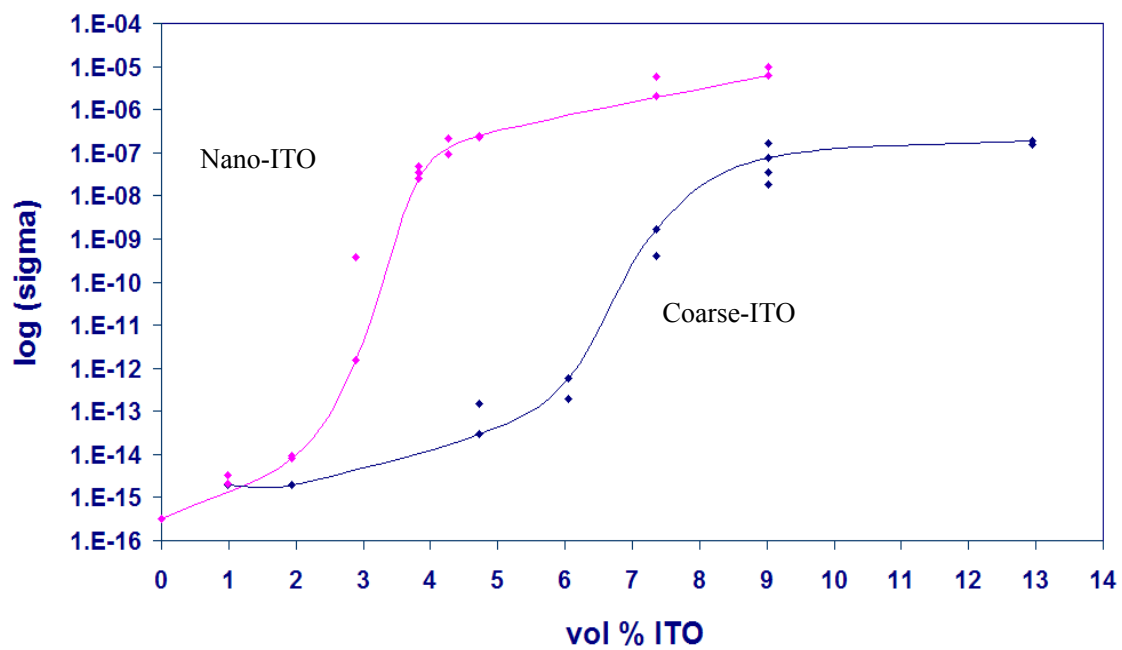
### LITERATURE REVIEW AND PROBLEM DESCRIPTION

In Part A, an oriented uniformly mixed polymer-nano particle system (IPP-CB) was studied. In this part of the research, the three-dimensional optical characterization of an unoriented and nonuniformly mixed polymer-nano particle composite system [Poly (methyl methacrylate) with nano-indium tin oxide (PMMA-ITO)] will be investigated.

#### 7.1 LITERATURE REVIEW OF PMMA-ITO (OR RELATED) SYSTEMS

##### 7.1.1 PMMA-ITO Composites

The poly (methyl methacrylate) with nano indium tin oxide (PMMA-ITO) composites which uses ITO as a filler is a new system. This present research is a joint project between Dr. Robert Samuels and Dr. Rosario Gerhardt (from School of Materials Science and Engineering of Georgia Tech). The percolation threshold value (see percolation threshold in 2.1.1.) was determined by Dr. Gerhardt's group<sup>98</sup>. In their study, ITO with two particle sizes, 31 nm and 3.5  $\mu\text{m}$ , were mixed with PMMA to fabricate composite samples. The percolation curves of the composites with both kinds of ITO particles are shown in Figure VII-1. Percolation was observed to occur when specimens contained 2-3% volume of nano-sized ITO. This threshold appeared significantly reduced compared to that of the specimens containing the coarse-sized (3.5  $\mu\text{m}$ ) ITO



**Figure II V-1.** Percolation curves of PMMA composites with nano-sized ITO (31 nm) and coarse ITO (3.5 μm)<sup>98</sup>

particles as filler when using an identical polymer matrix. In the present study, the optical characteristics of the same kind of PMMA-nano ITO composites used in the percolation investigation will be measured.

#### 7.1.2 ITO Filled Polymer Composites

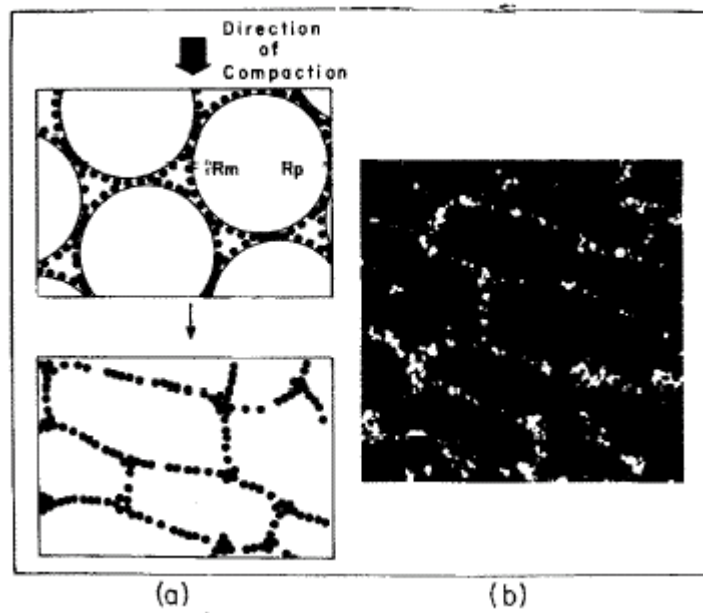
Miyazaki et al. did another study on polymer-ITO composites<sup>99</sup>. This is the only other study found which uses ITO as a filler in a polymer composite. In Miyazaki's research, urethane resin was chosen as a polymer matrix. Two different sizes of ITO particles were prepared, one was about 30nm and the other was about 10 microns. The composites were fabricated as follows: the polymer precursor and fillers were mixed and degassed; the precursor was placed between flat sheet glasses, and cured by UV and visible light irradiation. These composites were fabricated as films, and the thickness of each film was about 150 microns. The ITO concentration varied from 0.1 vol % - 1 vol %. As a result, the composites with a nano size ITO mixing ratio of 0.1-1% indicated an optically selective transparent property. Especially, in the case of the film that had 0.2% ITO mixed into composite, it was reflective in the IR region and transmitted over 80% in the visible region. This result suggested that an optically selective composite could be designed. However, the micron size ITO mixed composites didn't show this optically selective property<sup>99</sup>. The system studied in Miyazaki's research is very different from the composites investigated in the present research. Not only is the polymer various, but also the fabrication method is totally different. The composite films in Miyazaki's research are very thin and the ITO



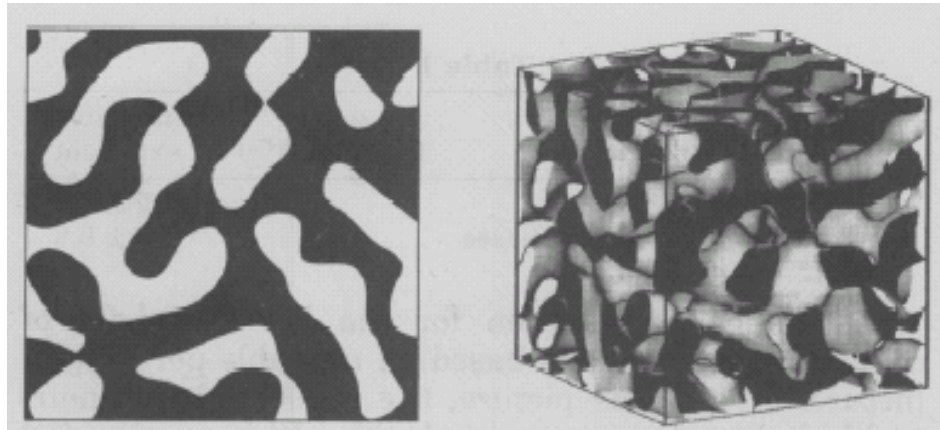
concentration is low. Therefore, it can't be easily compared with the present research.

### 7.1.3 Morphology of Polymer-Small Particle Composite

PMMA and ITO are immiscible (see 10.2). The immiscible system of polymer and filler contains large polymer particles and small filler particles. Malliaris, Cahn and Knackstedt et al. developed models to describe the morphologies for these kind of mixture<sup>100, 101, 102</sup> (Figure VII-2, Figure VII-3). They propose that the small particles just stay at the surface of the big particles. When the sample is compressed at high temperature, the shape of the big particles is changed by pressure and the small particles form a thin network at the interface.

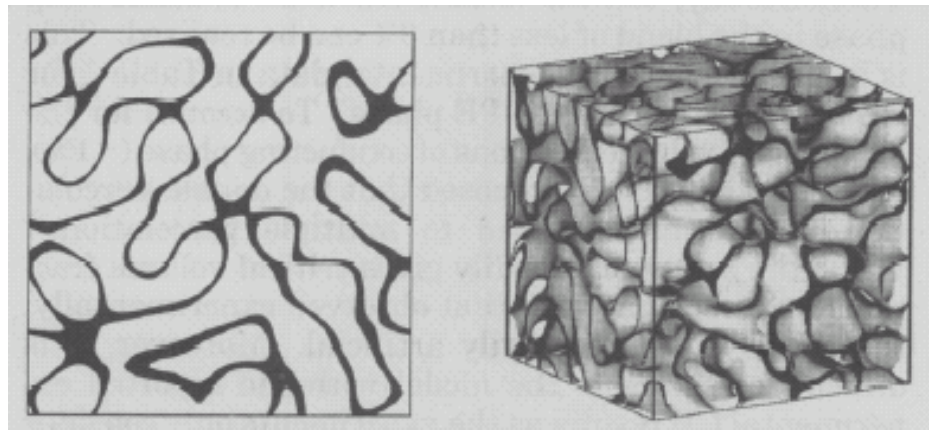


**Figure VII-2.** (a) Schematic showing compaction of polymeric particles with attendant smaller particles of metal. (b) Photo micrograph of 7 volume percent of nickel (4-7 $\mu$ ) in polyvinyl chloride (400X)<sup>100</sup>



a-1

a-2



b-1

b-2

**Figure VII-3.** (a) Model morphology given by Cahn's approach: a-1. Two-dimensional cut; a-2. Three-dimensional image. (b) Model morphology given by extending Cahn's approach: b-1. Two-dimensional cut; b-2. Three-dimensional image<sup>102</sup>.

## 7.2 PROBLEM DESCRIPTION

Since the PMMA-ITO composite is a new system, both the method used to investigate the characteristics and information about the properties of this system is limited. Some fundamental information on the process-property behavior, such as the optical characteristics and morphology, are needed. Therefore in the present study, methods for determining the three – dimensional optical constants and the morphology of compression molded PMMA-ITO composites are obtained.

## CHAPTER VIII

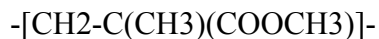
### OPTICAL CONSTANTS OF PMMA AND ITO

The main objective of this research is to obtain the optical constants of PMMA-ITO composites. Therefore, in this section, the optical constants of the two components, PMMA and ITO, are reviewed.

#### 8.1 OPTICAL CONSTANTS OF PMMA

##### 8.1.1 General Description of PMMA

The chemical structure of PMMA is:



The main optical properties of PMMA are<sup>103</sup>: Optically clear (92% transmission, theoretical limit for normal incidence, in the visible region) through the visible wavelength range; very little ultraviolet absorption until 260 nm. Because of this optical property, it is widely used as an optical plastic to replace glass in optical glass and optical fibers. PMMA can be used as one-component-deep UV, electron-beam, or ion-beam resists in the manufacture of microelectronics chips<sup>104, 105</sup>. PMMA has good mechanical properties (Tensile strength: 48-76 MPa<sup>104, 106, 107</sup>). Commercial grade materials generally have 50-70% syndiotactic, ~30% atactic, and <10% isotactic dyads<sup>108</sup>. PMMA also has high sensitivity to electron radiation.

### 8.1.2 Refractive Index of PMMA

The refractive index at the D line (589nm) is 1.49<sup>106, 109</sup>. The refractive index also changes with wavelength. In Figure VIII-1, the refractive index changing with wavelength from several references is plotted<sup>110, 111, 112, 113, 114</sup>. The results agree with one another very well. The refractive index changes with wavelength can be described by the Cauchy dispersion formula (Eq. VIII-1)<sup>115</sup>.

$$n = A + (B/\lambda^2) + (C/\lambda^4) \quad \text{Eq. VIII-1}$$

where  $n$  is the refractive index,  $\lambda$  is the wavelength, and  $A$ ,  $B$  and  $C$  are constants. The Cauchy dispersion formula gives reasonable agreement with experiment for many substances over limited regions of the spectrum. Sometimes only the first two terms are necessary.

The points in Figure VIII-1 come from different investigators. The fitted curve was using the first two terms of the Cauchy dispersion formula. As a result, the Cauchy dispersion formula for PMMA can be given by:

$$n_{\text{PMMA}} = 1.4776 + (4679.4/\lambda^2) \quad \text{Eq. VIII-2}$$

Thus the refractive indices of PMMA at 543nm and 1550nm are 1.493 and 1.478, respectively. In Figure VIII-1, the experimental results at 543nm are also about 1.493.

Since PMMA is optically transparent, the extinction coefficient,  $k$ , can be neglected.

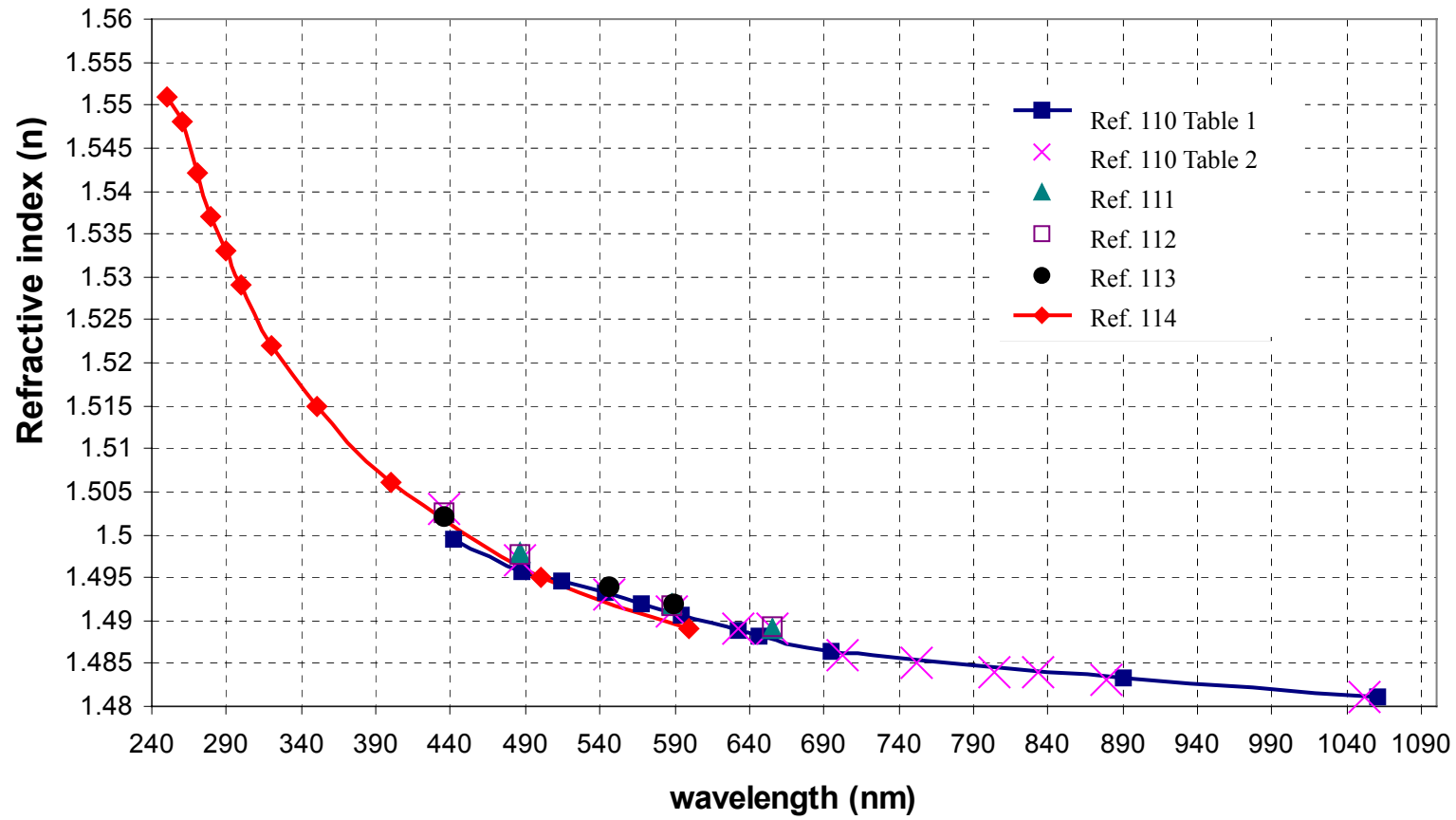


Figure VIII-1. Change in the refractive index of PMMA as a function of wavelength

## 8.2 OPTICAL CONSTANTS OF ITO

### 8.2.1 General Description of ITO

The chemical structure of Indium tin oxide (ITO) is  $\text{SnO}_2$  doped  $\text{In}_2\text{O}_3$  ( $\text{In}_2\text{O}_3:\text{Sn}$ ).

ITO is a transparent conductor, which is typically used as thin films. Generally, ITO transmits more than 90% of visible light and displays an electrical resistivity under  $4 \times 10^{-4} \, \Omega \, \text{cm}$ <sup>116</sup>. So far, the highest average transmission in the visible region is 96%<sup>117</sup>. A resistivity of  $\sim 1 \times 10^{-4} \, \Omega \, \text{cm}$  is often quoted as a number characterizing an optimized ITO film, even if lower resistivities have sometimes been claimed in the past<sup>118, 119</sup>. These interesting properties have led to a wide range of technical applications, in particular as energy-efficient windows<sup>121</sup> and as a contact or barrier in optoelectronic devices such as solar cells<sup>120</sup>.

The crystal structure and size of ITO depends strongly on the methods and conditions of preparation. This large variation in the crystal grain size affects some of the electrical properties such as electron mobility and consequently resistivity<sup>121</sup>.

Despite investigation of the dielectric and optical properties of ITO, a fundamental theoretical understanding of ITO has been limited. This is due to the complex chemical structure of  $\text{In}_2\text{O}_3$  and its changes after doping<sup>122</sup>.



### 8.2.2 Complex Refractive Index of ITO

The structure determines the properties. Thus the optical properties are different for different ITO's. Some of the literature values are listed in Table VIII-1. Since most of the optical constant results are reported as a plot that changes with wavelength, it is hard to obtain the exact experimental data from the figures. Therefore no numerical optical constants of ITO are shown in Table VIII-1.

In these references, the effect of deposition rate<sup>123</sup>, environment<sup>124</sup>, time<sup>125, 126</sup>, temperature<sup>127</sup> and substrate<sup>132</sup> are discussed. On the other hand, various models were used by the different investigations, which may also be a factor in the observed difference of the results. The problems of ellipsometry and KK transform based spectrophotometer have been discussed in 3.2.1. Therefore many factors can have an effect on the real and experimentally measured optical constants of ITO.

All of the above references are measurements of ITO thin films. No report deals with ITO thick films or bulk. Due to the variation of the reported data, the optical constants in the literature cannot be used in this study.

**Table VIII-1** Literatures on optical constants of ITO

<b>Sample fabrication</b>	<b>Wavelength region</b>	<b>Measurement method</b>	<b>Ref.</b>	<b>Figure # in ref.</b>	<b>Calculation model</b>
Plasma ion-assisted evaporation 90% indium oxide 10% tin oxide	200-2000 nm	Perkin-Elmer lambda 19 spectrometer and FTS 175 FTIR	123	7	Hamberg- Granqvist model <sup>128</sup>
a. The ITO film was sputtered in an atmosphere of 1.67% oxygen and then subjected to a postdeposition anneal at 250°C for 80 min; b. The ITO film was sputtered in an atmosphere of 4.17% oxygen and then subjected to a postdeposition anneal at 200°C for 120 min;	190-1100 nm	n & k Analyzer 1280	124	a. 1 b. 2	Forouhi-Bloomer dispersion equations <sup>129</sup>
DC-magnetron reactive sputtering. 90% indium oxide 10% tin oxide	300-3000 nm	UV-Vis-NIR spectrophotometer (Shimadzu UV 3101PC)	125	5 (Trans. spectra)	N/A
Sputtering and e-gun evaporation	1.5-5 ev	Phase-modulated spectroscopic ellipsometer (UVISEL Jobin-Yvon)	126	2	Bruggeman effective medium approximation <sup>130</sup>
Screen printing	200-1220 nm	Beckman UV 5240 spectrophotometer	127	9	Drude theoretical model <sup>131</sup>
Spray –pyrolysis technique	200-2000 nm	Hitachi UV-Vis-NIR double beam spectrophotometer	132	2	From ref. 133

## CHAPTER IX

### EXPERIMENTS

#### 9.1 SAMPLE FABRICATION

Circular PMMA- nano ITO composites were fabricated by compression molding to form disks. The disks formed were ~31 mm in diameter by 2 mm thick. The ITO concentration varied between 1 and 10 PHR. The sample at low concentration was translucent. The samples became increasingly opaque with increasing concentration and hence difficult to measure optically. For comparison, a pure PMMA ( $M_n=85,000$ ;  $M_w=115,000$ ) sample was fabricated under the same conditions.

#### 9.2 OPTICAL MEASUREMENTS

Since the samples are compression molded composites, the materials are random at the in-plane directions. Therefore the TE and TM measurement position of the PMMA-ITO composite sample is selected randomly in the plane of the sample. The measurement was done at 543 nm (green laser) using the IRIA setup and at 1550 nm (near infrared) by the knee method both at room temperature (24-25 °C).

For the knee method (see knee method in 3.2.1.2.2) measurement in the near infrared region, the intensity of the reflected beam was recorded by the Metricon control card every 0.015°. The incident intensity was assumed constant and the effect of the airgap

between the prism and the sample was ignored. The Metricon control software located the knee position at the biggest intensity drop (slope) automatically<sup>50</sup>. Two points on each sample were chosen randomly to measure both the in-plane and through-plane directions. Each measurement was repeated three times to get the average value and error bars.

In the visible region (543 nm) the incident and reflected intensity was recorded with the setup for the IRIA method (see IRIA method in 3.2.1.2.3): the intensities were recorded by the multimeters every 0.15°; the samples were measured with 300-400 different incident angles covering the total reflection to transmission regions.

Since the pure PMMA sample was optically transparent, it was measured by the both IRIA method and the knee method in the visible and near infrared regions.

### 9.3 MICROSCOPY STUDY

Pictures of the PMMA-ITO composite microstructure were taken in transmission with a LEICA DMRX optical microscope at room temperature with unpolarized light. The magnification was 10X.

The structure of the PMMA-ITO composite was also observed using a LEO 1530 Thermally-Assisted FEG Scanning Electron Microscope (SEM). They were fractured at room temperature and then coated with gold.

## CHAPTER X

### RESULTS AND DISCUSSIONS

#### 10.1 OPTICAL CHARACTERIZATION

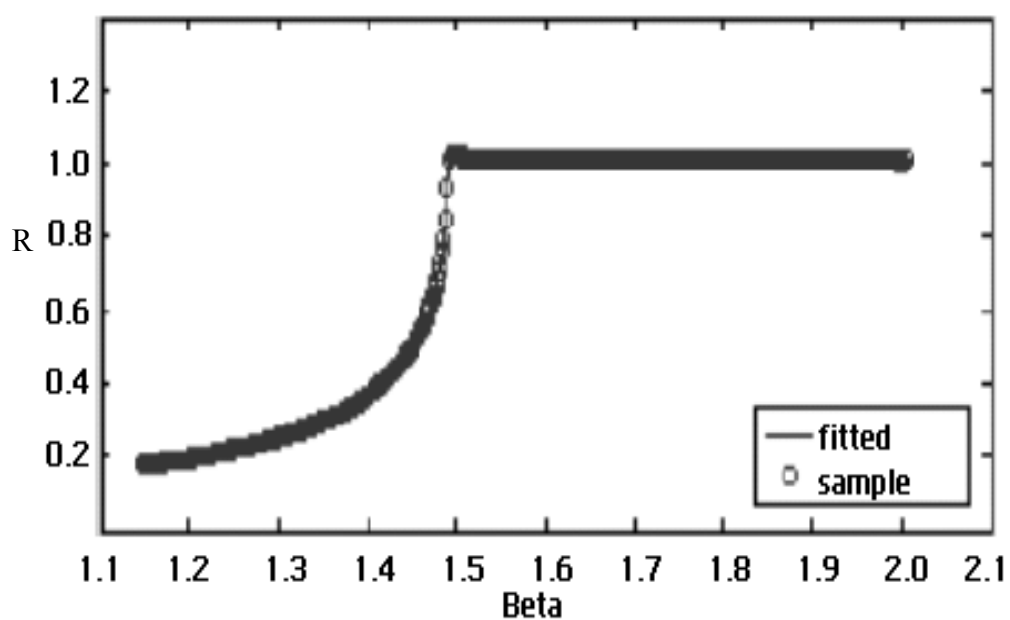
##### 10.1.1 Refractive Index of PMMA

In the present research, pure PMMA sample was measured by both the knee method (Table X-1) and the IRIA method (Figure X-1). In Figure X-1, it shows that the PMMA reflectance curve fit the IRIA model very well and the extinction coefficient,  $k$ , is zero. Table X-1 lists the refractive index measured by the knee method and calculated by Eq. VIII-2 at 543 and 1550 nm. The results are the same for the in-plane and the through-plane directions, so the sample is randomly oriented.

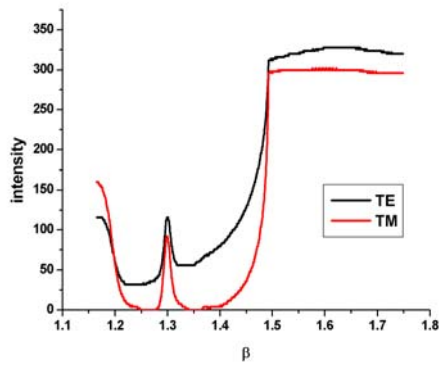
Compared to the system error of the knee method (see 3.2.1.2.2) and the IRIA method (see 12.1), the difference between the experimental results in the present research and from Eq. VIII-2 are negligible. On the other hand, the reflected intensity curves of PMMA show unusual behavior. In the transmission region, there are some irregular humps, depending on the position of the sample (Figure X-2). Figure X-2 shows the intensity curves of the same PMMA sample obtained at different sample locations. The hump position doesn't change with polarization. The reason for the humps is not clear yet. One of the possibilities will be discussed in section 10.3.

**Table X-1** Refractive index of PMMA

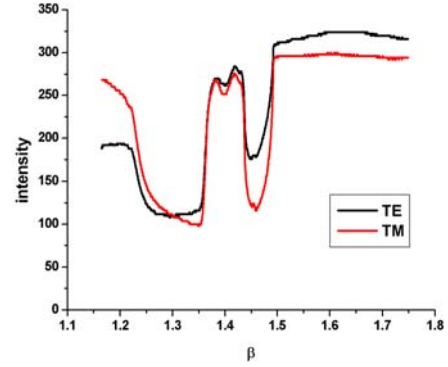
Wavelength (nm)		543	1550
n	By knee method	1.493	1.480
	By IRIA method	1.490	--
	By Eq. VIII-2	1.493	1.478



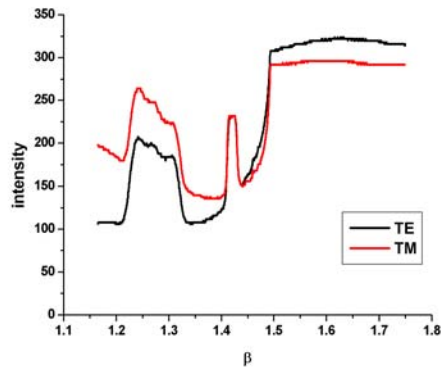
**Figure X-1.** IRIA fitting (TE) of the pure PMMA sample (fitted results:  $n=1.490$ ;  $k=0$ )



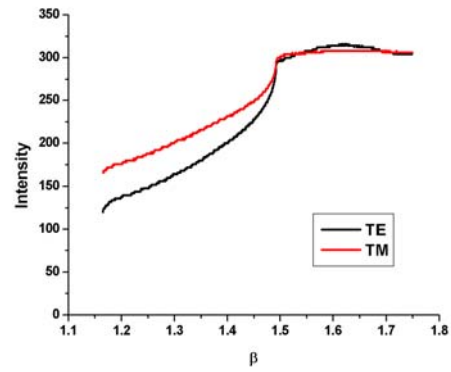
a. Point a



b. Point b



c. Point c



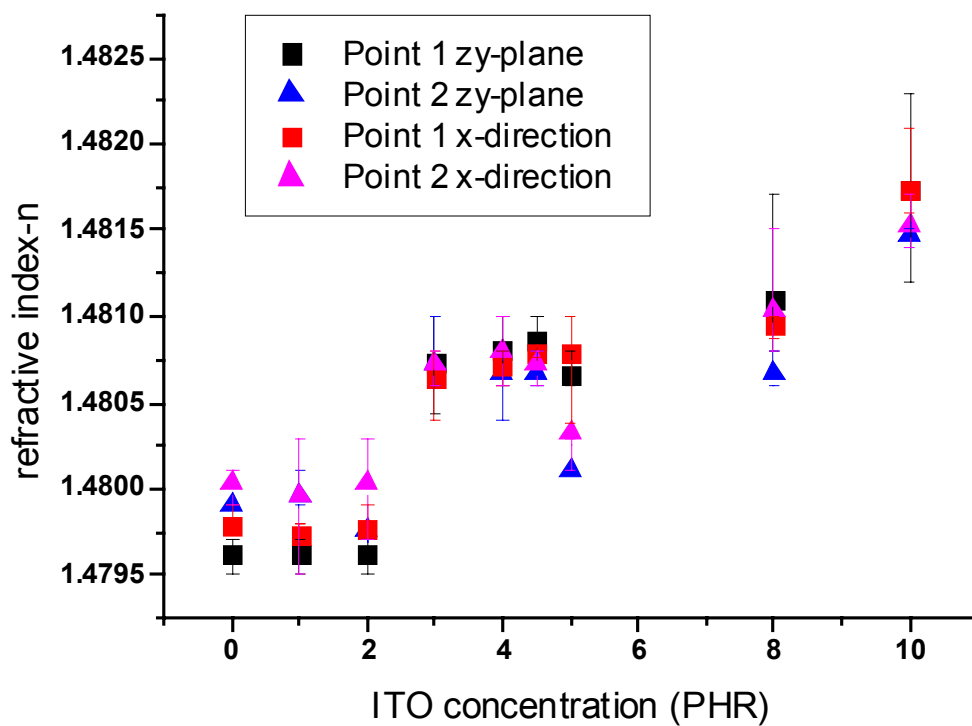
d. Point d

**Figure X-2.** The reflected intensity curves obtained at different examination points of the PMMA sample at 543nm

### 10.1.2 PMMA-ITO at 1550nm

The samples are transparent at 1550 nm (near infra red), so the knee method can be used to analyze the curve. The refractive indices of both the in-plane and through-plane directions at two measurement points are shown in Figure X-3. Since there is no difference between the refractive indices of both the two points and the in-plane and through-plane directions for the same ITO concentration sample, the samples are determined to be 3-D random. The refractive index increases very slightly with ITO concentration. Since the change is in the third place after the decimal point (0.002), which is in the same order as the error of the knee method, this increase can be ignored. The results show that the ITO has little effect on the composite refractive index at 1550 nm, even though the ITO concentration is as high as 10 PHR. For the insignificant change of the refractive indices and ignorable extinction coefficients of the composites in the near infrared, a possible explanation could be the similar refractive indices of ITO and PMMA at 1550 nm and both ITO and PMMA are optically transparent at 1550nm. The specific refractive index values for ITO at 1550nm are various in literatures ( $n \approx 1.4$  in ref. 123 and  $n \approx 1.2$  in ref. 132), depending on the fabrication method. Thus these values cannot be used to discuss the results in the present research.





**Figure X-3.** Refractive index of PMMA - nano ITO samples at 1550 nm as a function of ITO concentration

### 10.1.3 PMMA-ITO at 543nm

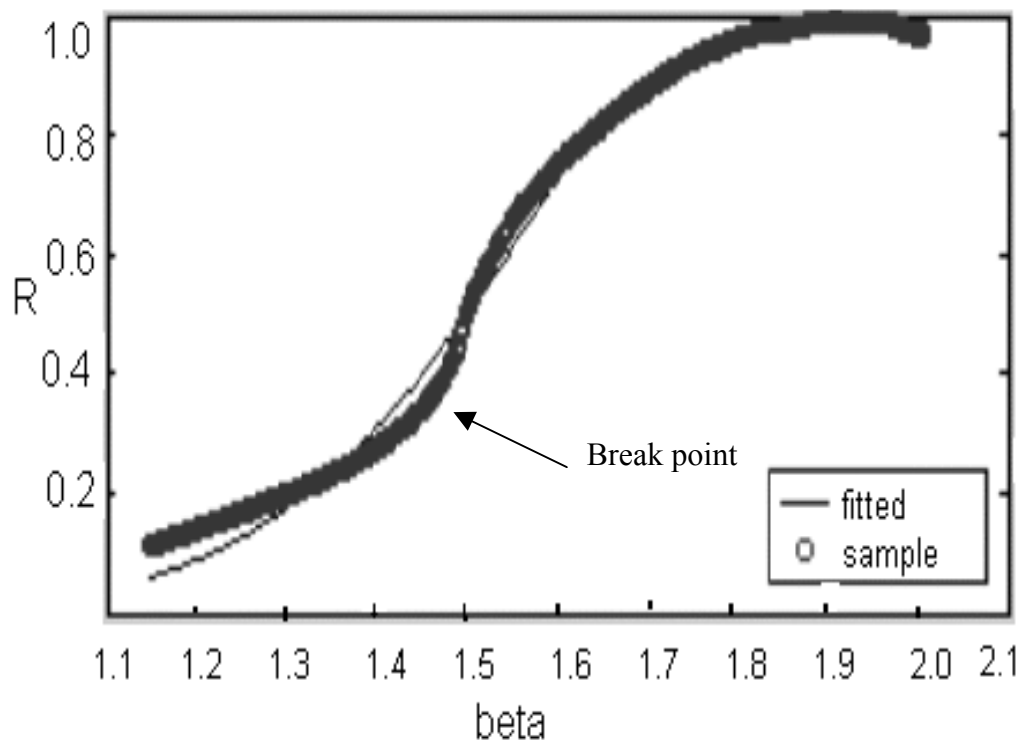
Initially, the IRIA model was used to fit the intensity data. However, the results show that none of the composite samples fit the model. In Figure X-4 the PMMA-10 PHR ITO composite TE measurement is used as an example to show the lack of fit of the IRIA model. Curves for the composite samples show a break point in the curve which prohibits use of the model. This kind of break point was observed with all composite samples for both in-plane and through-plane measurements (Figure X-5). The higher the ITO concentration, the more noticeable the break point.

Even though the data can't be fitted by the IRIA method, the curve still includes refractive index and the extinction coefficient information. Compared to the transparency of the composites in the near infrared (see 10.1.2), this break point in the visible region may be caused by scattering due to the presence of the ITO particles in the sample. This occurs because the scattering effect increases with decreasing wavelength. Since the scattering effect is different for transmitted light and the evanescent field for total reflectance, the break point can indicate the critical angle which can be used to calculate the refractive index of the sample. It has been observed that the curvature has a sharp change at the break point, therefore by finding the peak position of the slope of the curve, the critical angle can be determined (Figure X-6).

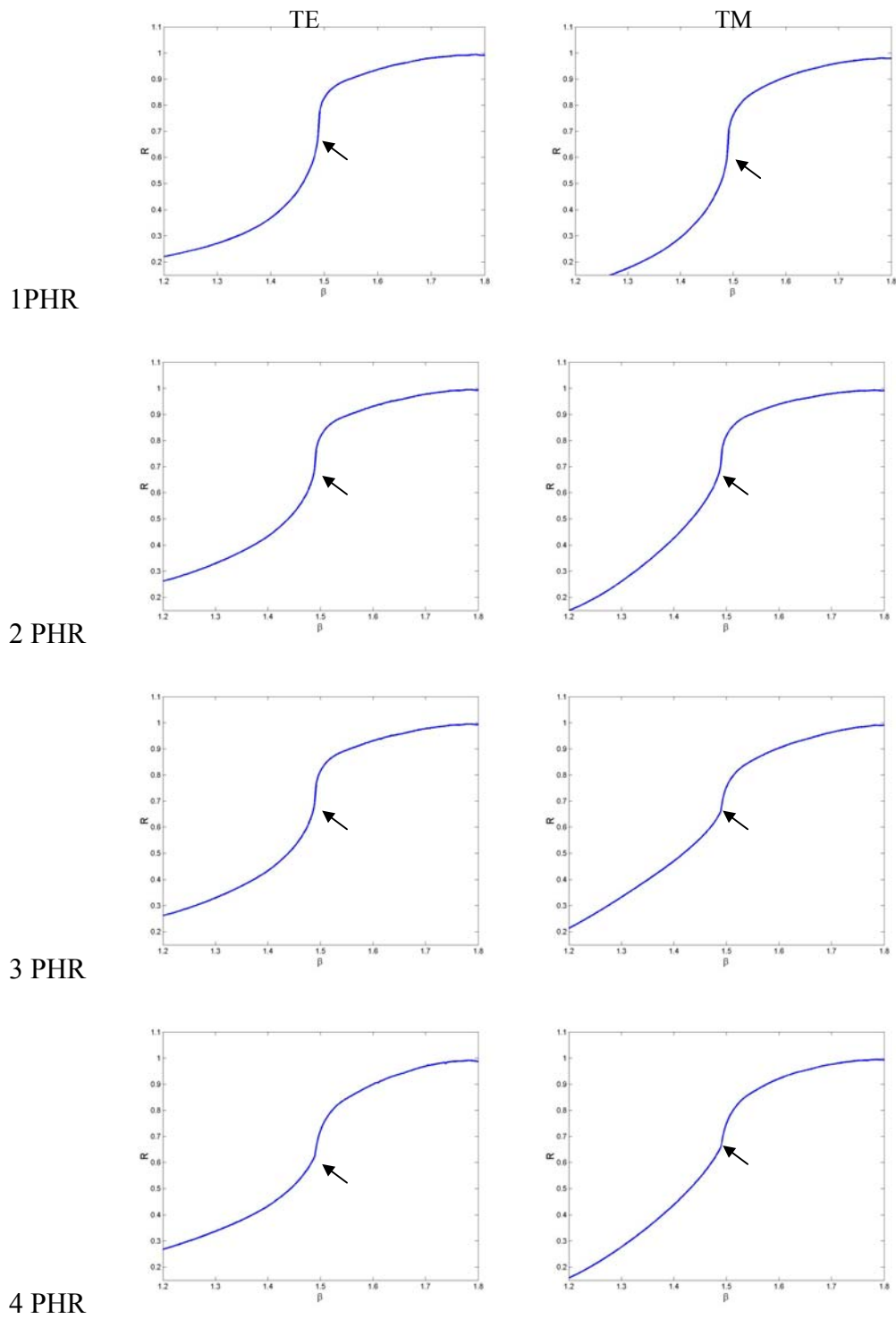
In Figure X-6 the slope of each point was calculated by

$$D_i(R) = (R_{i+1} - R_i) / (\beta_{i+1} - \beta_i) \quad \text{Eq. X-1}$$

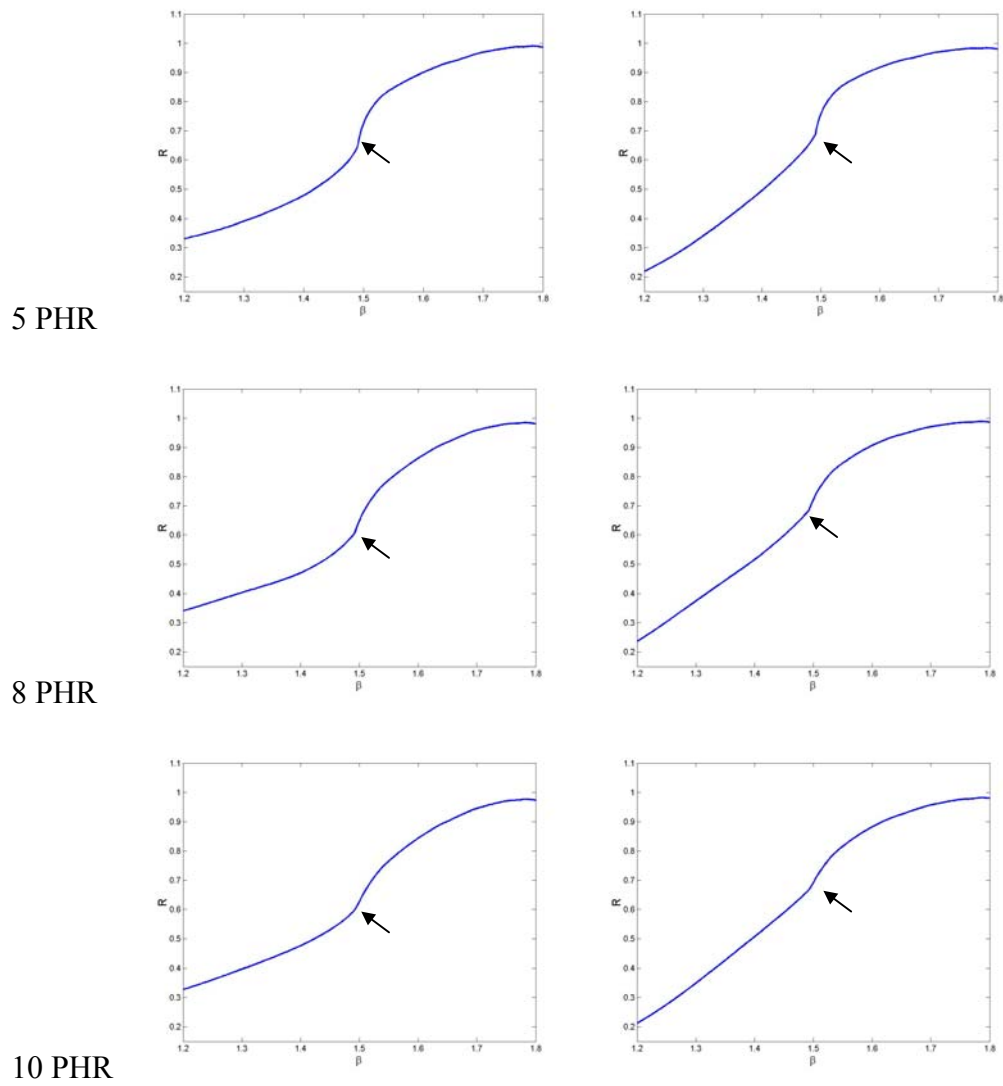
Where  $R_i$ ,  $D_i$  and  $\beta_i$  are the reflectance, the slope (the differential reflectance) and the  $n_{\text{prism}} \sin(\theta_i)$  at the  $i$ th point.



**Figure X-4.** IRIA fitting of the PMMA-10PHR ITO sample for TE polarization



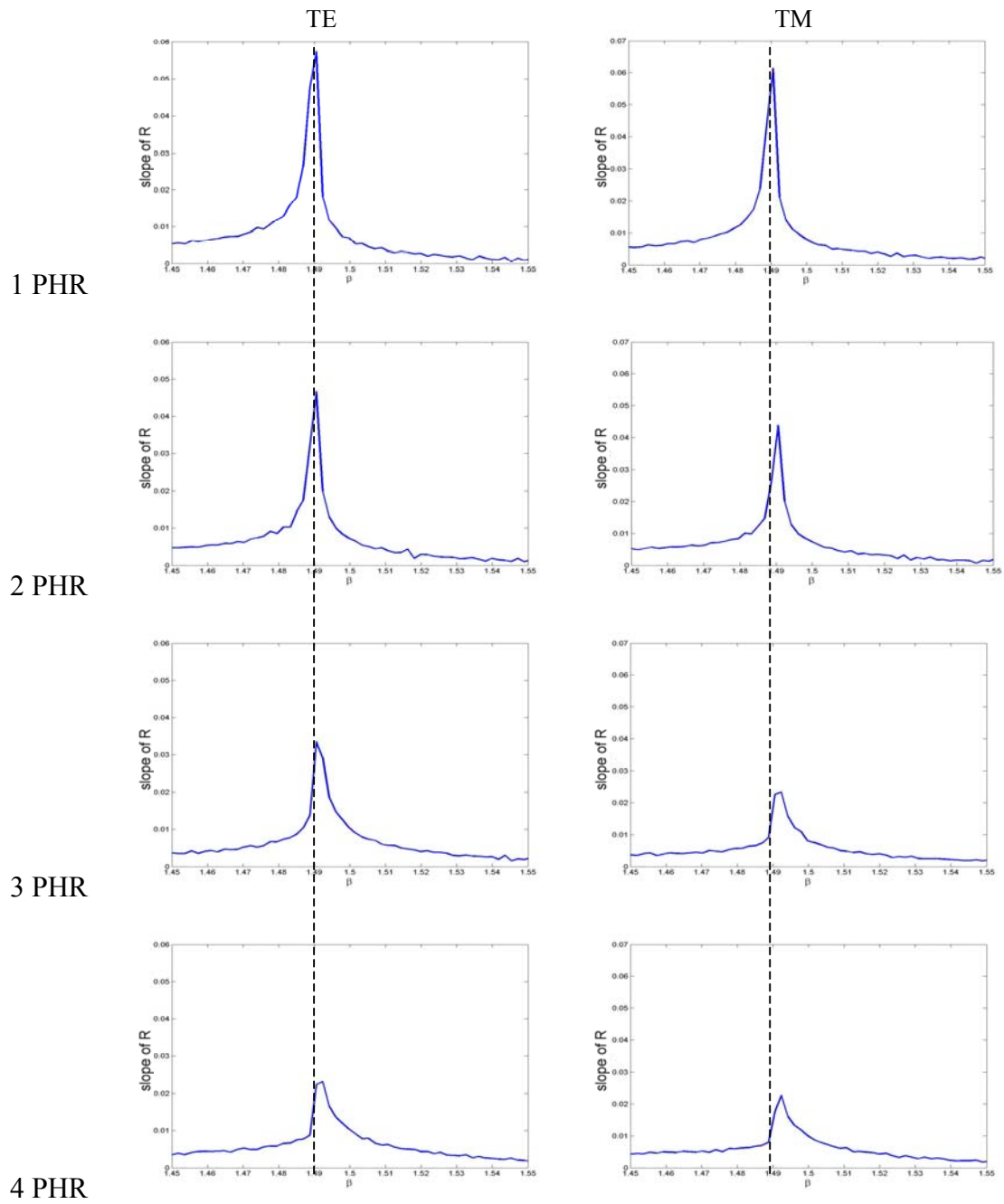
**Figure X-5.** The reflectance curves of PMMA-ITO samples. ( $\rightarrow$ : brake point)



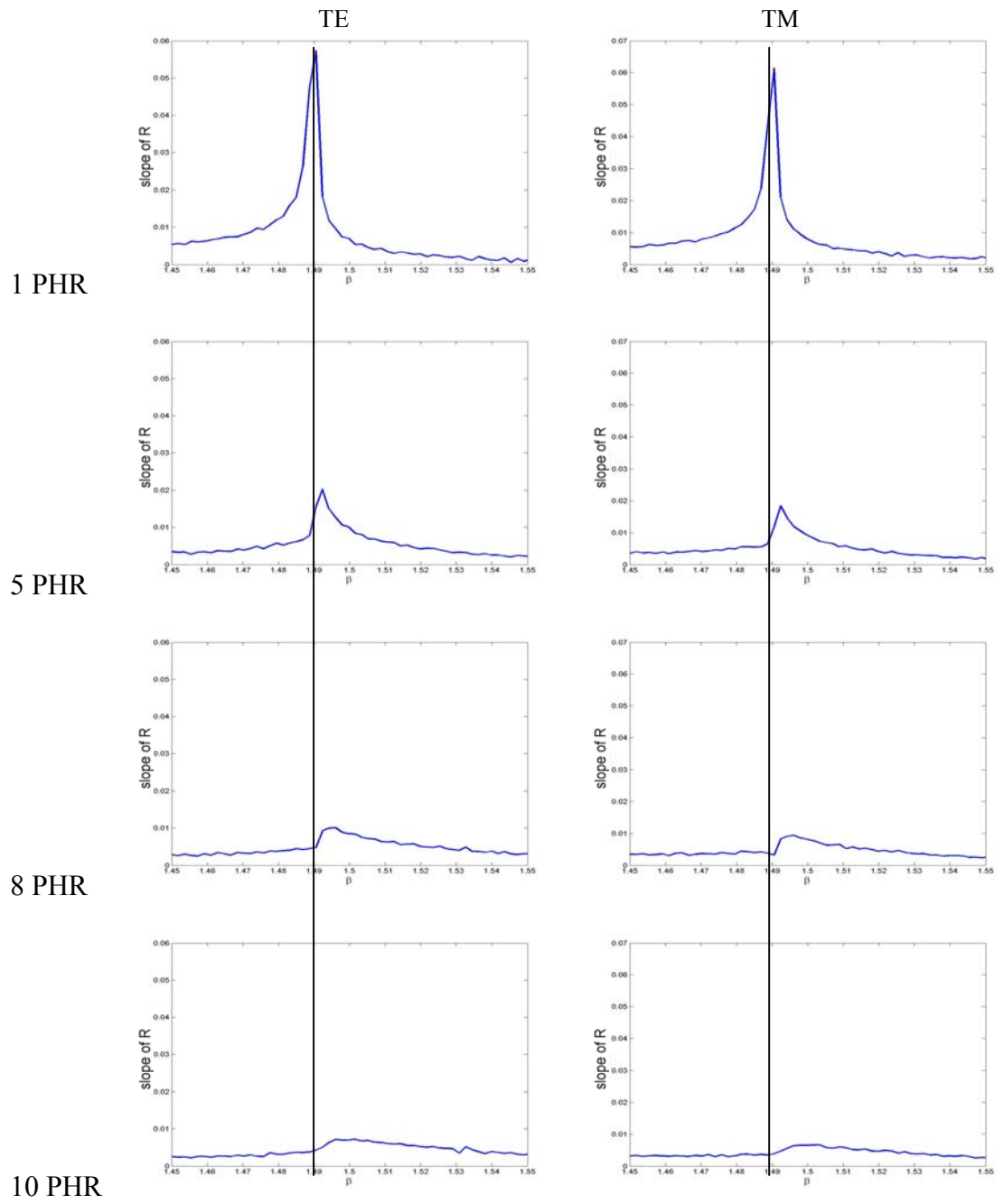
**Figure X-5 (cont'd)** The reflectance curves of PMMA-ITO samples. ( $\rightarrow$ : brake point)

From Figure X-6, it is noticed that the peak position shifts slightly to the higher  $\beta$  value with increasing ITO concentration. The  $\beta$  values next to the peaks provide the refractive indices. The refractive indices change with ITO concentrations curve are shown in Figure X-7. The error bar,  $\pm 0.01$ , in Figure X-7, indicates the system error with a 0.15 degree resolution. The refractive index of PMMA is taken by the average results of the knee method and the IRIA method in Table X-1. And the error bar of PMMA indicates the difference of the refractive index from the two methods.

Since the TE measurement is related to the in-plane direction refractive index and the TM measurement is related to the through-plane direction refractive index, the overlapped refractive index curves of the two polarizations suggests that the PMMA-ITO composites are three-dimensionally random. This result shown in Figure X-7 is consistent with the near infrared region measurement (see 10.1.2). The trend of the curve indicates that the refractive index increases slightly at low ITO concentrations, but then increases rapidly after a concentration of 5 PHR. The magnitude of the concentration rate change is significantly greater than that observed for the near infrared region (see 10.1.2).

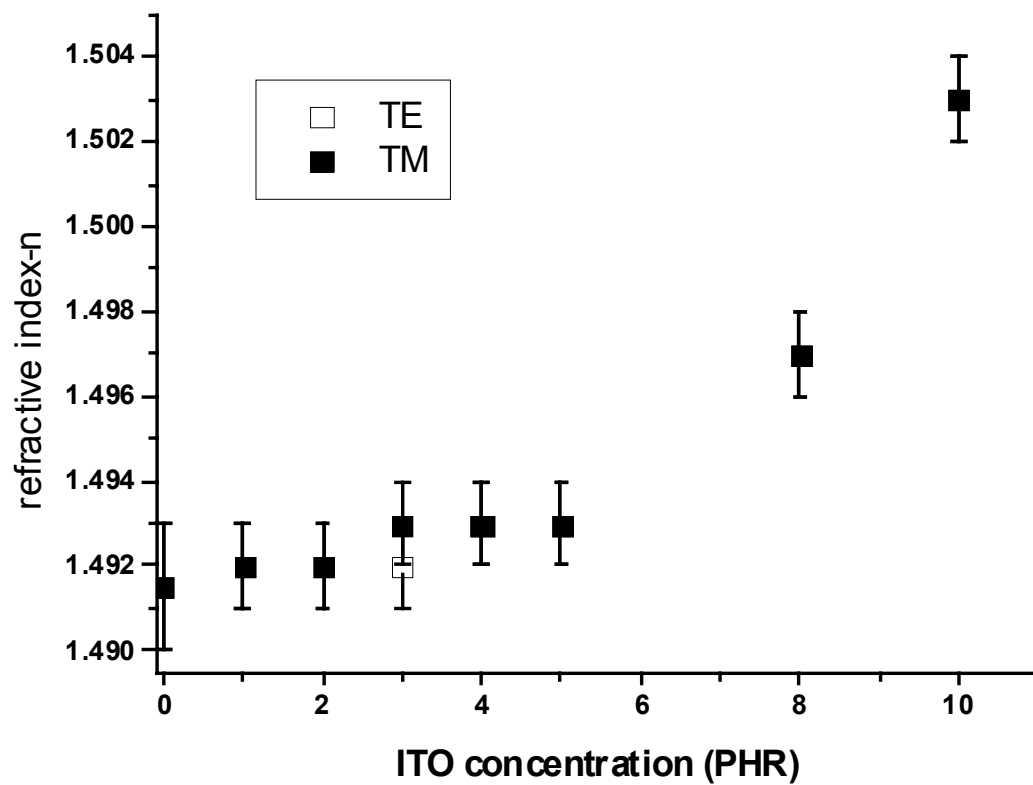


**Figure X-6.** The slope of the reflectance curves (dashed line:  $\beta$  at peak of 1 PHR)



**Figure X-6 (cont'd).** The slope of the reflectance curves (dashed line:  $\beta$  at peak of 1 PHR)





**Figure X-7.** The change in the refractive indices of the PMMA-ITO samples as a function of ITO concentrations.

The other information provided by the slope of the curve (Figure X-6) is the height of the peak. It clearly shows that the height decreases with increasing ITO concentration. The height of the peak contains the extinction coefficient information. The method used to explore the extinction coefficient is based on the IRIA model equations. In the IRIA model, each curve includes three unknowns: the refractive index, the extinction coefficient of the sample and the thickness of the airgap between the prism and the sample. Since the refractive index of the sample is already known from the peak position, some assumptions of the airgap are required in order to get the extinction coefficient. The thickness of airgap was assumed to be 0.03-0.05 micron. This region was decided on by referencing the IRIA fitting of the PMMA and the PMMA-ITO samples. This is also an empirically reasonable airgap thickness for good contact between the sample and the prism. In order to use the height of the slope peak to get the extinction coefficient information, another assumption was made: At the break point and the point just before the break point, the “scattering” effect is the same. The purpose of this assumption is to cancel the “scattering” effect at the break point, therefore the slope of the PMMA-ITO sample at this point will be used to calculate an equivalent sample IRIA curve with the three parameter model using the given refractive index and the thickness of airgap and the slope at the break point the same as the IRIA model.

The process for finding the extinction coefficient is:

- a. Plot the differential  $R$  vs.  $k$  curve for both the 0.03micron and 0.05micron airgap, based on the IRIA model. Do this for both the in-plane and through- plane directions.

- b. Draw a line with the height of the experimental differential R in the differential R vs. k plots.
- c. Find the intersection of the line with the two airgap curves, which is the possible extinction coefficient region of the given polarization. Do this for both the in-plane and through- plane directions. The intersection will give the region of the k value of the sample.

The PMMA-5PHR ITO sample is used here as an example to explain the above method step by step. First, from the refractive index analysis, the refractive index of the 5 PHR PMMA-ITO samples was determined to be 1.493. Series TE polarized IRIA model curves with fixed refractive index=1.493 and airgap=0.03 micron were plotted (Figure X-8). The only variable in this figure is the extinction coefficient. With increasing extinction coefficient, the sharp knee becomes smooth. The vertical line in the figure indicates the refractive index position. It shows that the position changes from the sharp turn of the curve to the tail. It was noticed that the break point is located at the place, so that the method for obtaining the refractive index from the break point is a reasonable method.

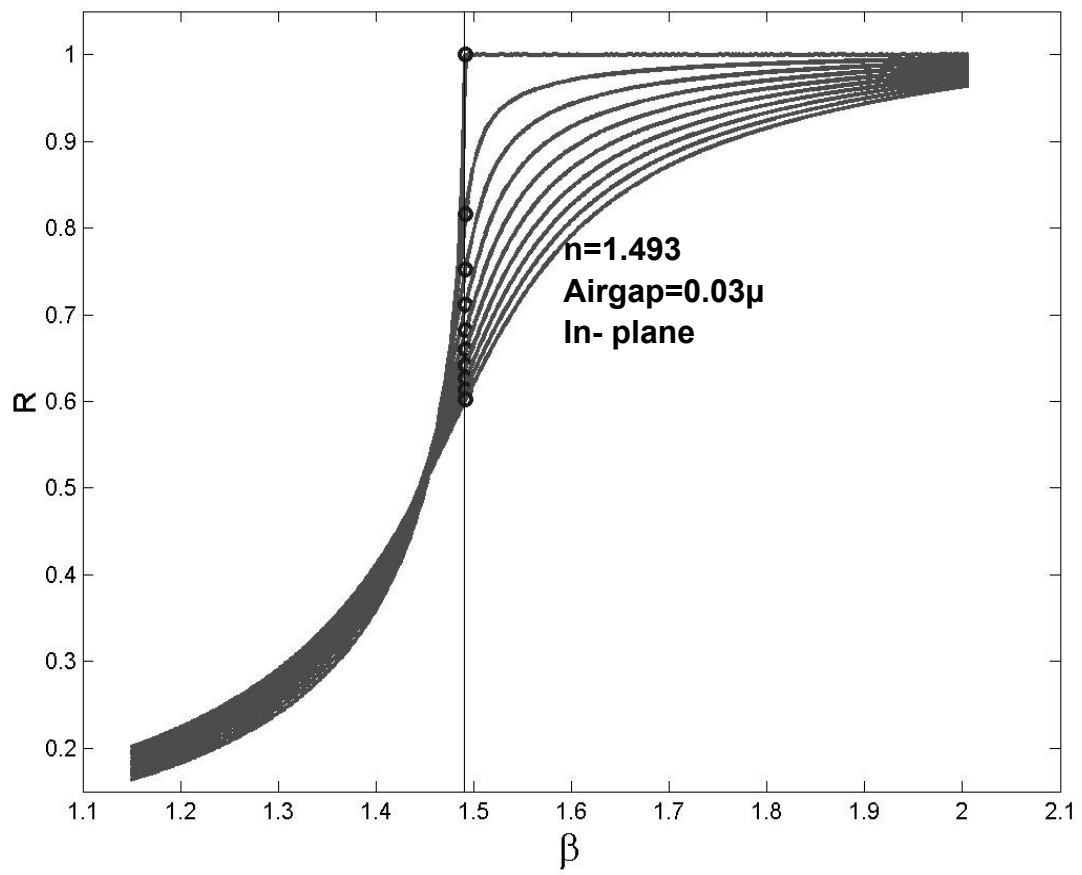
The slope at  $\beta = n$  of each single curve (circled in Figure X-8) was calculated, and the slope is plotted against the extinction coefficient in Figure X-9 (the lower dashed line). Changing the airgap to 0.05 and doing exactly the same thing one can obtain the upper bound of the in-plane value (the higher dashed line). Then read the slope peak height, 0.02, from Figure X-6 (5 PHR TE), and draw a straight line at slope equals 0.02 in Figure X-9. The extinction coefficient, k, value at the two intersection points

of the upper and lower bound lines, defines the  $k$  region for the TE model (0.005-0.008). Do the same thing for the TM model, to determine the TM  $k$  region (0.001-0.009). Since the sample is 3-D random, the intersection of the TE and the TM models will provide the region of the extinction coefficient. For the 5 PHR PMMA-ITO composite, shown in Figure X-9 the  $k$  value given by this method is 0.005-0.008.

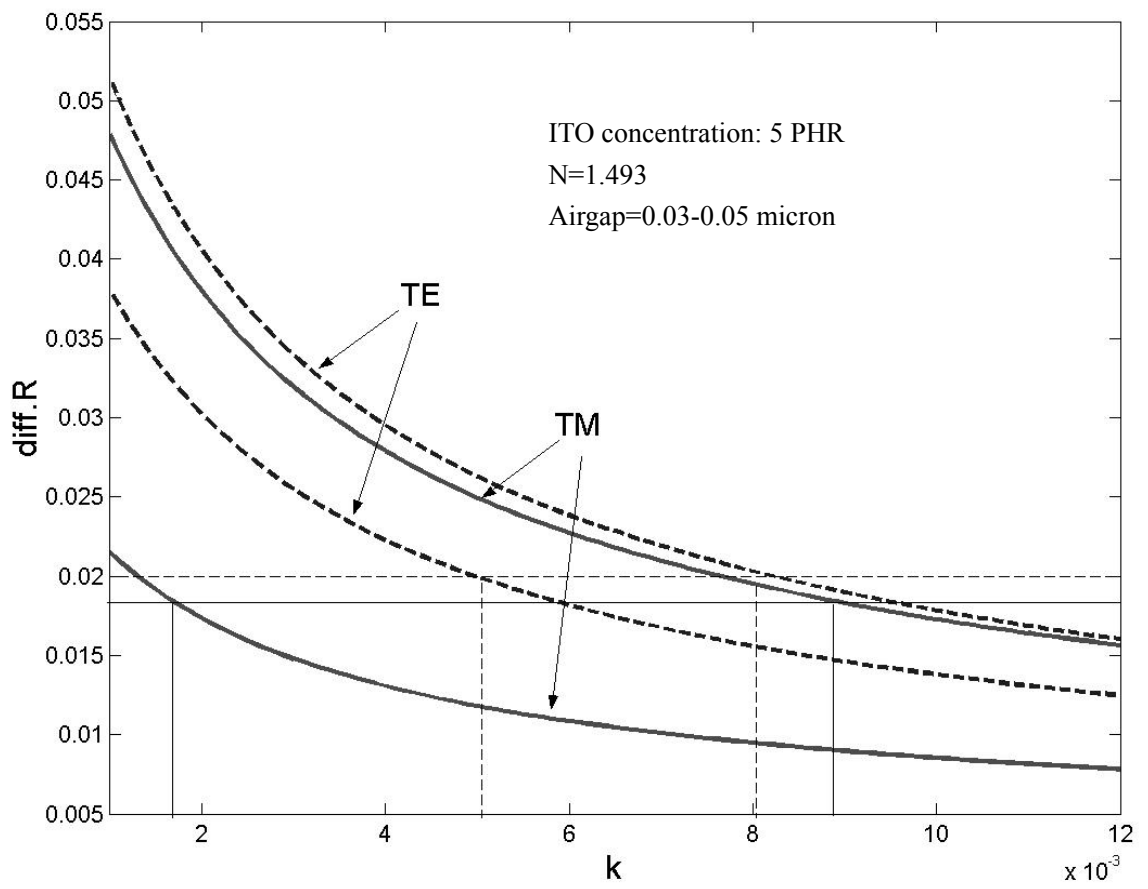
In Figure X-10, the extinction coefficients obtained by this method are plotted against the ITO concentration. As was indicated, the extinction coefficient has a similar trend as the refractive index, which increased slightly at low ITO concentrations, but then increased rapidly after a concentration of 5 PHR.

The overall results of the refractive indices and the extinction coefficients as a function of ITO concentration are listed in Table X-2.

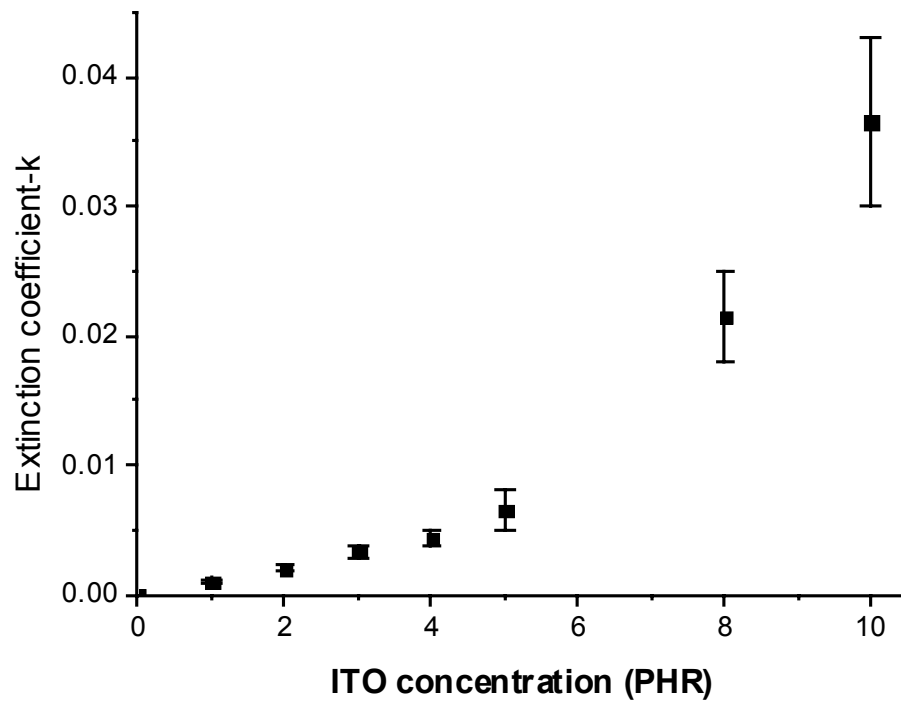
This method cannot provide exact values of the extinction coefficient. However, it provides a unique way to explore the relationship of  $k$  with ITO concentration which cannot be obtained by any other method. The trend is clear and results are reasonable.



**Figure X-8.** The curves of TE modeling calculation with  $n=1.493$  airgap  $=0.03$  micron at 543 nm.



**Figure X-9.** An example of finding  $k$  using a modified IRIA method (The Example is for PMMA-5PHR ITO sample.)



**Figure X-10.** The extinction coefficient of PMMA- ITO samples as a function of ITO concentration found by modified IRIA method

**Table X-2** The refractive index and the extinction coefficients of PMMA-ITO samples as a function of ITO concentration

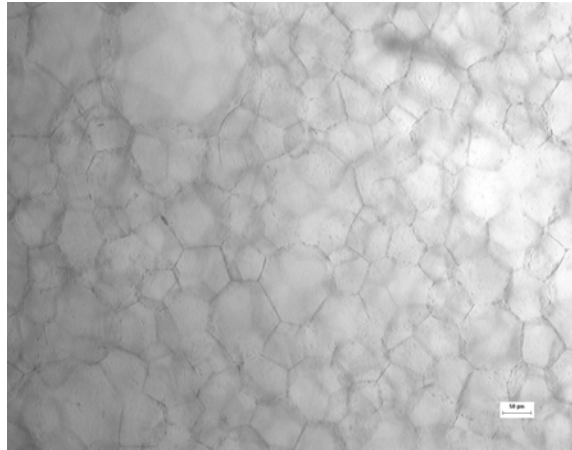
[ITO] (PHR)	n		k	
	Value	Uncertainty	Upper bound	Lower bound
0	1.4915	0.0015	0	0
1	1.492	0.001	0.0009	0.0011
2	1.492	0.001	0.0018	0.0022
3	1.4925	0.0015	0.0029	0.0038
4	1.493	0.001	0.004	0.005
5	1.493	0.001	0.005	0.008
8	1.497	0.001	0.018	0.025
10	1.503	0.001	0.030	0.043

## 10.2 MORPHOLOGY STUDY

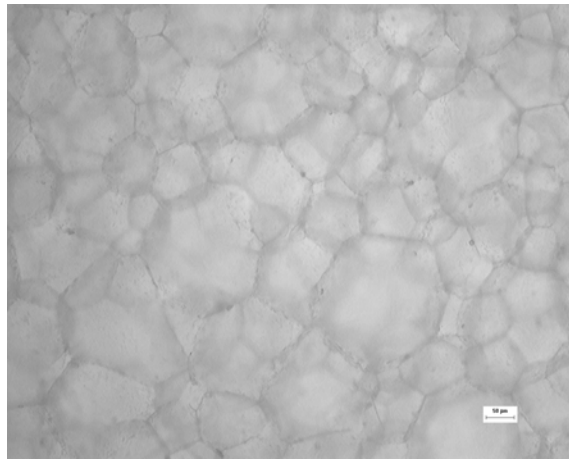
The morphological study of the PMMA-ITO composite samples indicates that the primary difficulty of fitting the IRIA curves from the PMMA-ITO composites came from the heterogeneous structure of the sample. In Figure X-11 and Figure X-12, the optical microscopy and SEM pictures clearly shows the grain structure. This kind of structure was caused by the immiscibility of the polymer matrix and the small size inorganic filler (see 7.1.4). Figure X-12 for example shows the SEM images of the PMMA-10 PHR ITO composite. In the images, the white flakes are ITO and the big grains are PMMA. The nano ITO agglomerated together into micron size. The PMMA-10 PHR ITO is electrically conducting (see 6.1.1), so the discontinued distribution of ITO in the PMMA grain surface shows the tunneling effect. The size of the grain is ~100 micron. Compared to the wavelength of the green light 543nm, these composites are nonuniformly mixed, thus the scattering effect is notable.

The humps shown in the reflected intensity curves in Figure X-2 may also be due to the same discontinuous phase structure shown in Figure X-11 and Figure X-12. Figure X-13 schematically shows how the high reflected intensity humps in Figure X-2 might be caused by the reflectance at the interface between the grains.

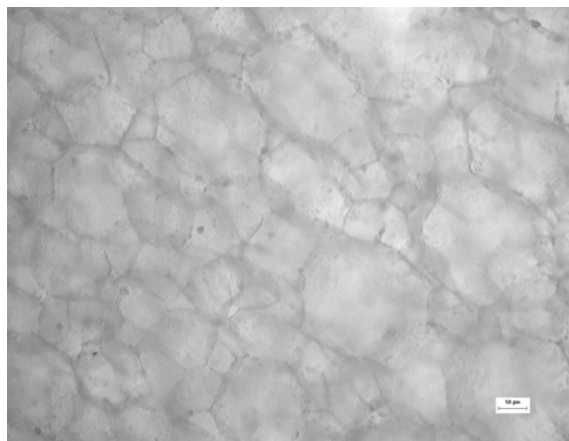




a. 1 PHR

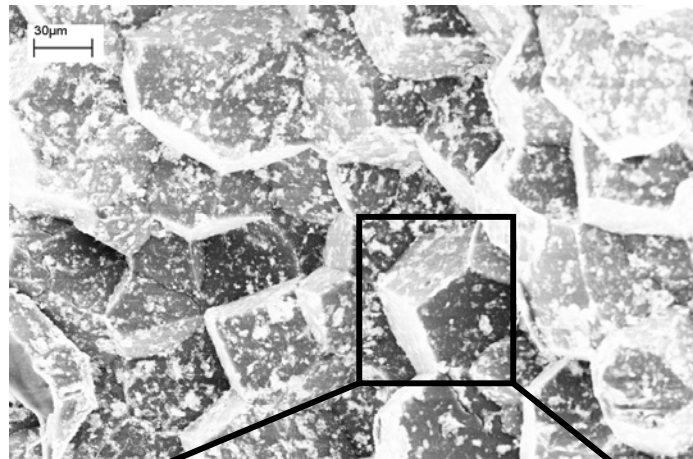


b. 5 PHR



c. 10 PHR

**Figure X-11** the optical microscopy pictures of PMMA-ITO samples (10X) (scale bar = 50 microns)

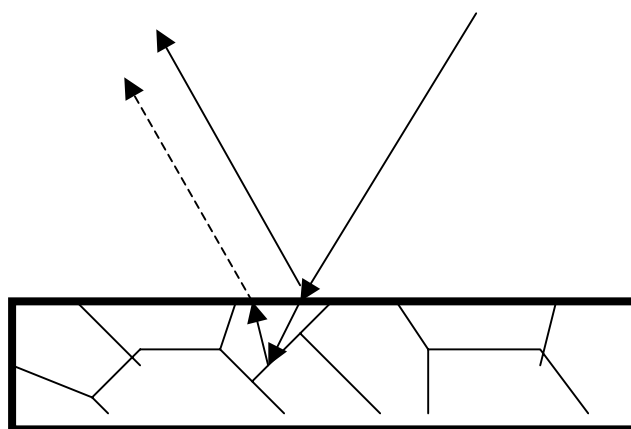


a. 300X

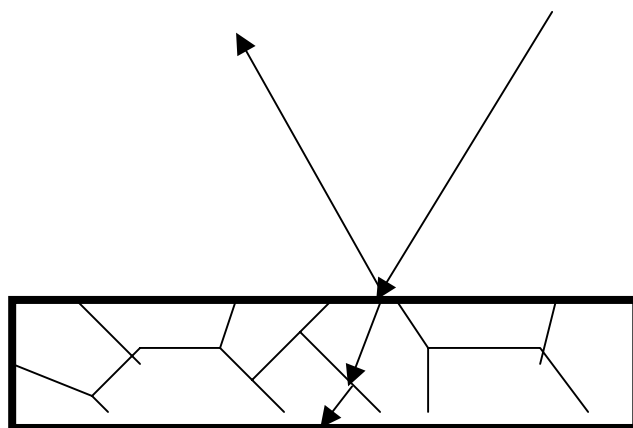


b. 1200X

**Figure X-12** The SEM pictures of 10 PHR PMMA-ITO samples (the bright regions are ITO and the dark regions are PMMA)



a. hump observed



b. no hump observed

**Figure X-13.** Schematic drawing of how the possible structure of PMMA could possibly cause the humps in the reflected intensity curves shown in Figure X-2.

## CHAPTER XI

### CONCLUSIONS

The PMMA-ITO composites are optically transparent at 1550 nm but absorbing in the visible region. This research proposed a unique method to obtain the optical properties of nonuniformly distributed heterogeneous absorbing samples in the visible region. A modified IRIA method was used to determine the optical characteristics of compression molded PMMA- ITO samples. The break point in the intensity curve was used to obtain the refractive index value. Based on the refractive index results and some assumptions, an estimate region of the extinction coefficient was obtained by analyzing the IRIA model equations. The results show that the samples are three-dimensionally random and are absorbing at 543 nm (green light). Both the refractive index and the extinction coefficient increased slightly at low ITO concentrations, but then increased rapidly after a concentration of 5 PHR.

As suggested by the optical results, the microscope images confirm that the samples are not uniform. Though this type of structure has been known for more than 30 years, this is the first time the optical constants of composites which contain large size grains has been measured.

PART C

SYSTEM OPERATIONS

## CHAPTER XII

### SYSTEM OPERATION

The IRIA method has been demonstrated to be a powerful way to measure the optical characteristics of uniformly optical absorbing samples<sup>8, 51, 53</sup>. However, during the experiments, some problems were found. First, it is hard to know the experimental uncertainty. Second, since in the IRIA model, three unknowns ( $n$ ,  $k$  and the airgap) need to be fitted from one set of data, the error of each factor, especially the airgap, has a big effect on the accuracy of the fitted results. Therefore in this part of the thesis, the Bootstrap method is introduced to the IRIA method to estimate the experimental uncertainties. Also the Big Area Method and the Two-Line method are proposed to increase the accuracy of the IRIA measurement. Finally, based on the IRIA model, the Modified Knee Method was developed, which can substitute for the conventional Knee method to provide very accurate refractive index values when the extinction coefficients are less than 0.01. At last, the four methods can be integrated together, to update the current waveguide method.

#### 12.1 EXPERIMENTAL UNCERTAINTY ANALYSIS: BOOTSTRAP IN IRIA

##### 12.1.1 History and Background of Bootstrap

As a statistical method, the Bootstrap method was introduced by Dr. B. Efron in

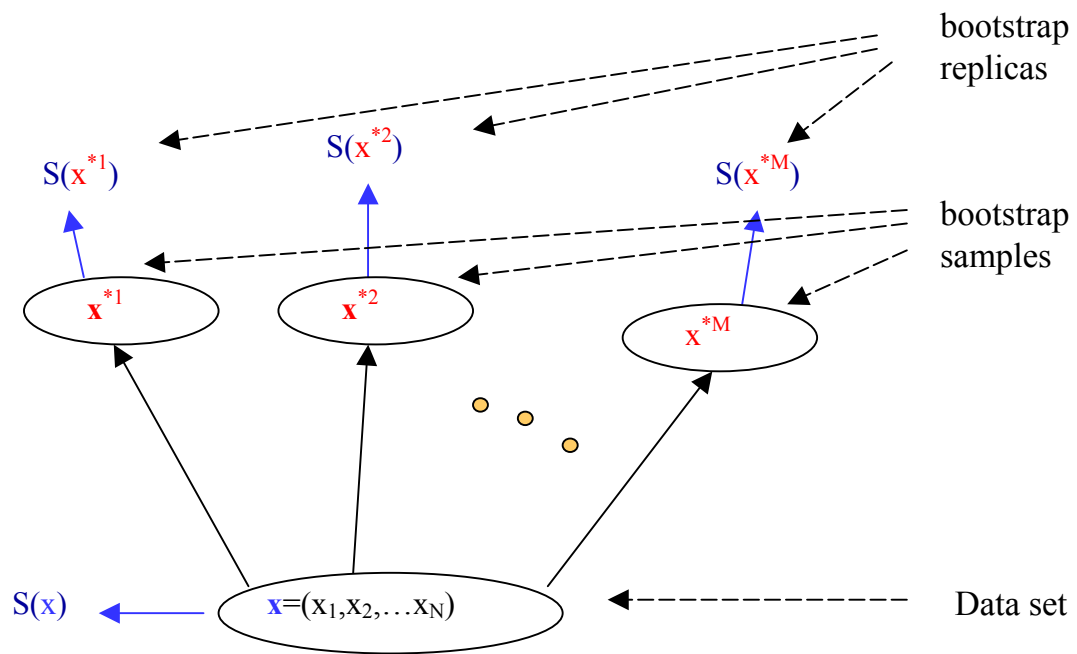
1979<sup>134, 135, 136</sup>. The name of “Bootstrap” came from the adage “Lifting oneself by one’s own bootstrap”. The biggest advantage of this method is that it can estimate the uncertainty within only one set of experimental data.

Figure XII-1 schematically shows the Bootstrap procedure. The Bootstrap is a procedure that involves choosing random samples,  $x^{1*}, x^{2*}, \dots, x^{m*}$ , with replacement from a data set,  $x$ , and analyzing each sample the same way. Sampling with replacement means that every sample is returned to the data set after sampling. So a particular data point from the original data set could appear multiple times in a given bootstrap sample. The number of elements in each bootstrap sample equals the number of elements in the original data set. In particular, the mean and standard deviation of each parameter’s distribution are the measured parameter and the error bar, respectively. The range of sample estimates,  $S(x^{1*}), S(x^{2*}), \dots, S(x^{m*})$ , allows people to establish the uncertainty of the quantity they are estimating<sup>137</sup>.

The Bootstrap Method requires independent and identically distributed (or *iid*) data points<sup>138</sup>. It means there are three assumptions in this method:

- a) The experimental data are independent of each other;
- b) All experimental data have the same weight in the model;
- c) All experimental data have the same error distribution.

This method can be quite computation-intensive; however, by using a modern computer, it’s not prohibitive. For the IRIA measurement, each experimental curve typically includes 300-500 data points. The Bootstrap results with hundreds of times resampling can be obtained in tens of minutes by a personal computer.



**Figure XII-1.** A schematic drawing of the Bootstrap procedure<sup>134</sup>



### 12.1.2 Bootstrap in IRIA

In order to apply the bootstrap method into IRIA, the three assumptions were checked at first. For the first assumption, the IRIA measurement procedure indicates that the intensity obtained at each different angle is tested independently. Since the Least Square Method was used to fit the curve, the weight of the data in the model is the same, which agrees with the second assumption. It is expected that the main source of the error is from the instability of the laser. The short-term (time during one measurement) intensity drift of the laser is random. Therefore, the uncertainty of the reflectance, which is used to fit the results, is in a random distribution. From the analyses above, we see the Bootstrap method can be used in the IRIA method.

The error analysis operations by the Bootstrap in the IRIA method are:

- a) Measurement: Record the intensities of the sample and air at different incident angles by the IRIA system, and calculate the reflectance;
- b) Bootstrap sampling: Do Bootstrap sampling, and get new Bootstrap samples. (see Bootstrap sample in 12.1.1) The samples are chosen by a random matrix which is generated by the computer. For example, if the experimental data set,  $x=[x(1), x(2), \dots, x(n)]$ , has  $n$  samples, first a matrix with  $n$  random numbers is made as  $[r_1, r_2, \dots, r_n]$ , for which the value of some elements may be the same; then, the new sample set is chosen as  $[x(r_1), x(r_2), \dots, x(r_n)]$ . Do this sampling 100-300 times;
- c) Fit the Bootstrap samples: Load each of the Bootstrap samples to the IRIA model and fit the curve.

- d) Error analysis: Plot the bootstrap results into a histogram and fit the distribution with a Normal distribution. The means ( $\mu$ 's) of the refractive index and of the extinction coefficient yield the measured optical properties. The standard deviation ( $\delta$ ) is used to calculate the error bars with different confidence limits. For a 95% confident limit, the system error is  $\pm 2\delta$ ; for a 99% confident limit, the system error is  $\pm 3\delta$ .

### 12.1.3 Experimental Results and Discussions:

As mentioned in Part A, the Bootstrap method was successfully used in the uncertainty analysis of the IPP-CB samples. (See Chapter V)

For the IPP-CB samples, Table V-1 shows that the experimental uncertainty is in the third place after the decimal point. The uncertainty analysis also helped to confirm the conclusions of crystallinity and axially. The crystallinities of the IPP-CB films with different carbon black concentrations are the same within the error bars (Figure V-4). And the difference between the refractive indices in the y and x directions of the carbon black filled isotactic polypropylene samples are significant, even after adding the error bars (Figure V-3). So the IPP-CB films are biaxial.

### 12.1.4 Limitation of Bootstrap

Since only one set of experimental data is used in the Bootstrap method, the accuracy of Bootstrap depends highly on the error distribution of the data. There are many discussions on this limitation<sup>134</sup>. Regardless of the complicated statistics theory, the

author of the present research suggests to run the IRIA measurement three times and use the data set which gives the middle refractive index and/or extinction coefficient results to do Bootstrap, so that the means from the bootstrapping are more accurate and the coverage of the error bar will be closer to the real uncertainty region.

The other limitation is caused by the IRIA measurement procedure. Since in the IRIA measurement, the ratios of intensities of the sample and air are taken as the reflectance, there are two kinds of errors in the reflectance data set: absolute error and relative error. The absolute error is defined as if the difference between the measured or inferred value of a quantity,  $x_0$ , and its actual value  $x$ , which is by

$$\Delta x \equiv x_0 - x \quad \text{Eq. XII-1}$$

the difference is called the absolute error. In contrast, the relative error is defined by

$$\delta x = \frac{\Delta x}{x} = \frac{x_0 - x}{x} = \frac{x_0}{x} - 1, \quad \text{Eq. XII-2}$$

where  $\Delta x$  is the absolute error<sup>139</sup>. So in the IRIA measurement, the short term (during one measurement) drift causes the absolute error and the long term (between two the measurements of air and sample) drift leads to the relative error. Because in the IRIA, the calculation of reflectance is done before the Bootstrap sampling, the Bootstrap can't deal with the relative error, but only the absolutely error. So the Bootstrap analysis can only provide part of the whole error.

Here are some simple theoretical modeling calculations that give some basic discussion of the relatively error. The model was setup as:

- a) The refractive index of sample,  $n=1.5$ , and the extinction coefficient,  $k=0.05$ ;

- b) Airgap=0.05micron;
- c) Wavelength = 543nm;
- d) Prism parameters: the same as prism 6614 ( $n=2.184 @ 543\text{nm}$ )
- e) The drift during air measurement is 0%,  $\pm 0.1\%$ ,  $\pm 0.5\%$  and  $\pm 1\%$  (“+” means the intensity is bigger than the reference; “-” means the intensity is smaller than reference); No drift during sample measurement (no relative error in sample measurement).
- f) No short term drift (no absolute error) during both air and sample measurements

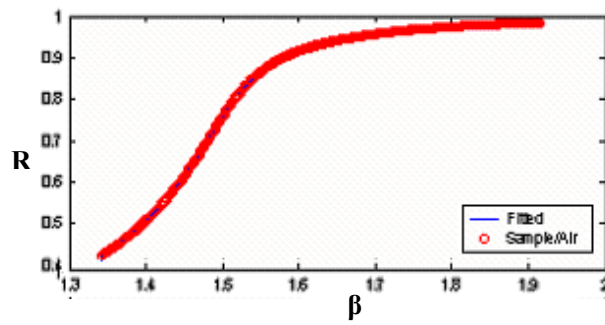
The fitted curves results are listed in Table XII-1. The no drift and  $\pm 1\%$  drift fitted curves are shown in Figure XII-2. From Figure XII-2, all three curves look like they fitted the model beautifully (the experimental curve and fitted curve are overlapping each other), but the errors on results are clearly shown in Table XII-1. Within  $\pm 1\%$  drift, the errors on the refractive index and the extinction coefficient are  $< 0.007$  for both  $n$  and  $k$ . This analysis indicates, even for nicely fitted curves, the error bars may not be very small.

However, the real experimental condition is more complicated than this model, so these calculations can only be used to provide the order of the relative error. On the other hand, the absolute error and the relative error cannot be separated very clearly in the experimental data, so the real error bar of the IRIA method is still hard to know.

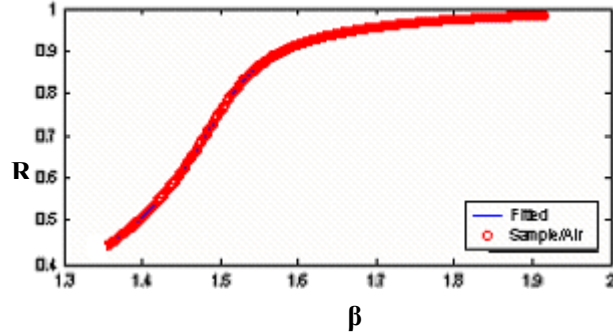
Though there are some limitations of the Bootstrap method, in most cases, it still can help us to identify the measurement uncertainty and confirm the results.

**Table XII-1.** The fitted results of the model by IRIA method

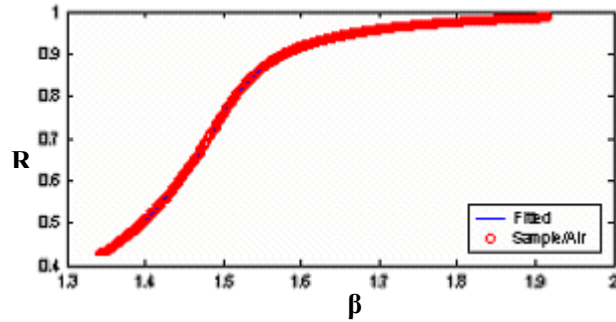
drift	0	+0.1%	-0.1%	+0.5%	-0.5%	+1%	-1%
n	1.5	1.49943	1.50055	1.49707	1.50269	1.49392	1.50514
k	0.05	0.05062	0.04937	0.05310	0.04686	0.05614	0.04372
Airgap (micron)	0.05	0.04971	0.05029	0.04852	0.05143	0.04700	0.05282



a. No drift



b. +1% drift



c. -1% drift

**Figure XII-2.** The fitted curves of the model with relative error

## 12.2 THE TWO-LINE METHOD

### 12.2.1 The Two-Line Method Model

For every IRIA curve fitting, three unknowns need to be fitted, which are the refractive index, the extinction coefficient of the sample and the thickness of the airgap. The refractive index and the extinction coefficient are the sample properties one expects to get, but the airgap is only a factor of the experiment. However, the airgap has a big effect on the shape of the curve, so one of the key issues to improve the accuracy of the measurement is to give the thickness of the airgap or to cancel the effect of the airgap. Actually, it is almost impossible to really measure the thickness of the airgap, so the only practical way is to cancel the effect of the airgap.

Here, the two-line method was proposed to improve the accuracy of the measurement via eliminating the effect of the airgap. In the two-line method, instead of using one set of reflectance curves, two reflectance curves of the same sample with different airgaps are used to fit one set of the refractive index and the extinction coefficient and the thicknesses of the two airgaps. Apparently, it increases the workload and adds one more unknown into the fitting model, but indeed, since there are two curves and obtains the same  $n$  and  $k$ , the effect of the airgaps, which are immeasurable, are eliminated. Therefore the accuracy of the measurement is increased. The process of the two-line method is:

- a) Record the intensities at different incident angles of sample with *Airgap1* (at lower pressure) at both TE and TM polarizations;
- b) Record the intensities at different incident angles without sample (air only) at both TE and TM polarizations

- c) Record the intensities at different incident angles of sample with *Airgap2* (at higher pressure) at both TE and TM polarizations
- d) Use the air curve to normalize both of the sample curves, and get *Reflectance curve 1* and *Reflectance curve 2* for both TE and TM.
- e) Load both of the reflectance curves into the IRIA model and fit one set of the refractive index and the extinction coefficient, and thickness of two airgaps.

#### 12.2.2 Modeling Calculation

Figure XII-3 shows the demonstration of the Two-Line method. In this demonstration, a thick film sample with  $n=1.5$  and  $k=0.05$  at 543nm was assumed, and the thickness of the airgaps was 0.05 and 0.01 micron, respectively. The fitted curves are overlapped with the demonstrated experimental curves. The fitting results are  $n=1.49992$ ,  $k=0.050025$ ,  $airgap_1=0.050005$ ,  $airgap_2=0.010003$ , which are same as the assumptions, so this method is theoretically correct.

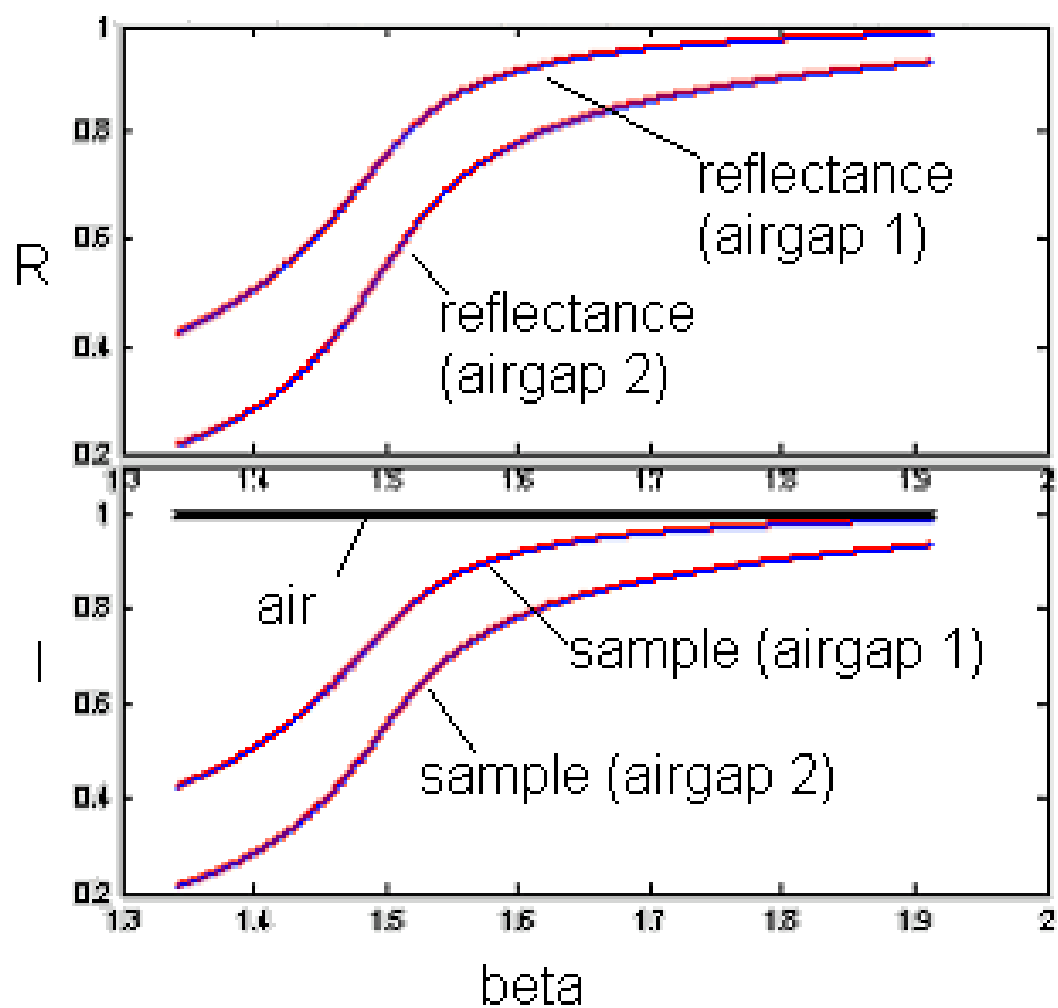


Figure XII-3. Modeling testing of Two-Line method



### 12.2.3 Experimental Testing Results and Discussions

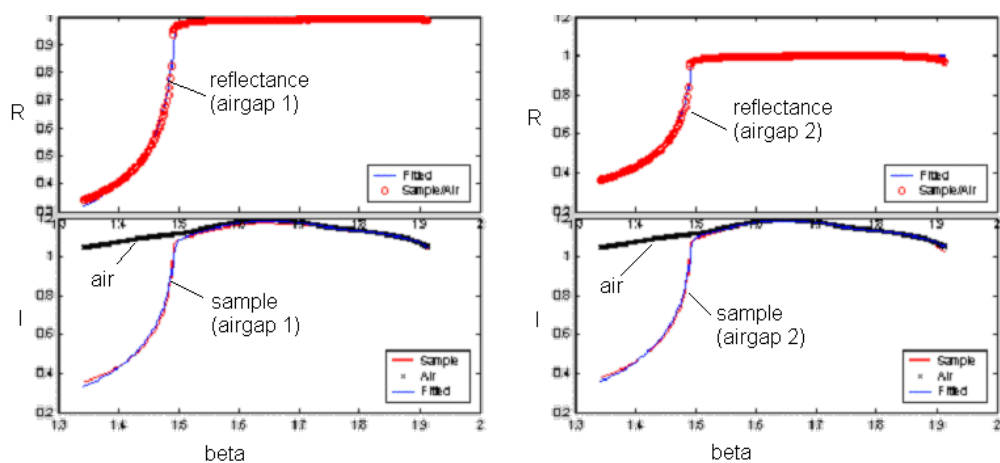
Figure XII-4 shows one of the Two-Line measurements. The sample is PMMA-0.1 PHR ITO sample. The sample was measured at 543nm with TE polarization. In Table XII-2, the results from conventional IRIA and the Two-Line method are compared. It shows the Two-Line method can effectively eliminate the effect of the airgap in the conventional IRIA method.

**Table XII-2.** The fitting results of PMMA-0.1 PHR ITO samples by the conventional IRIA method and the Two-Line Method

Method		n	k	Airgap 1	Airgap 2
IRIA	Airgap 1	1.4913	0.0024	0.0376	----
	Airgap 2	1.4914	0.0015	----	0.0424
Two-line	Airgap 1 & 2	1.4914	0.0018	0.0375	0.0426

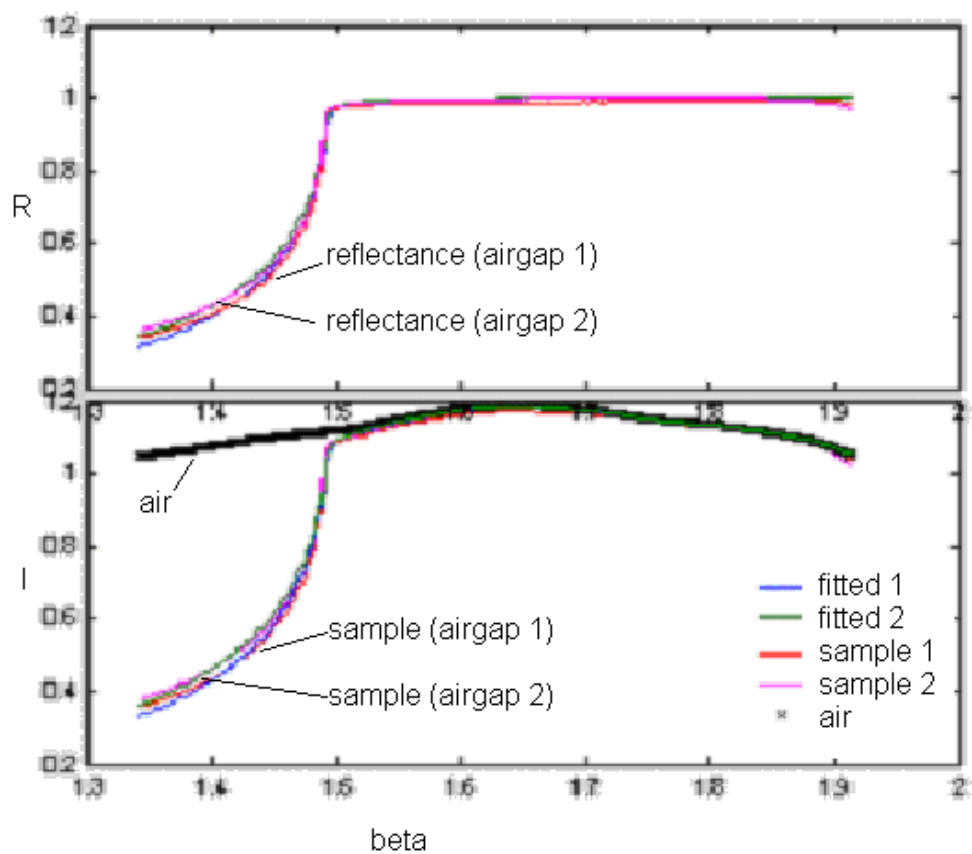
### 12.2.4 Limitation of the Two-Line method

However, some problems were found during the experiment. First, it is hard to adjust the pressure to get two separate curves. Typically, for a given sample, the region of the airgap, which can provide good contact, is small, so that the two curves are very close to each other. For example, in Figure XII-4, these two lines are very close. But this is one of the best separations obtained in the measurements. Second, since the laser has a long-term drift, when the air curve is used to normalize the sample, the error of the two curves caused by the drift may be different. Therefore, the error will be a factor of the fitting.



a-1. IRIA of airgap 1

a-2. IRIA of airgap 2



b. Two-Line method of airgap 1 and 2

**Figure XII-4.** The experimental fitting curves of PMMA-0.1 phr ITO with the conventional IRIA method and the Two-Line method

## 12.3 THE BIG-AREA METHOD

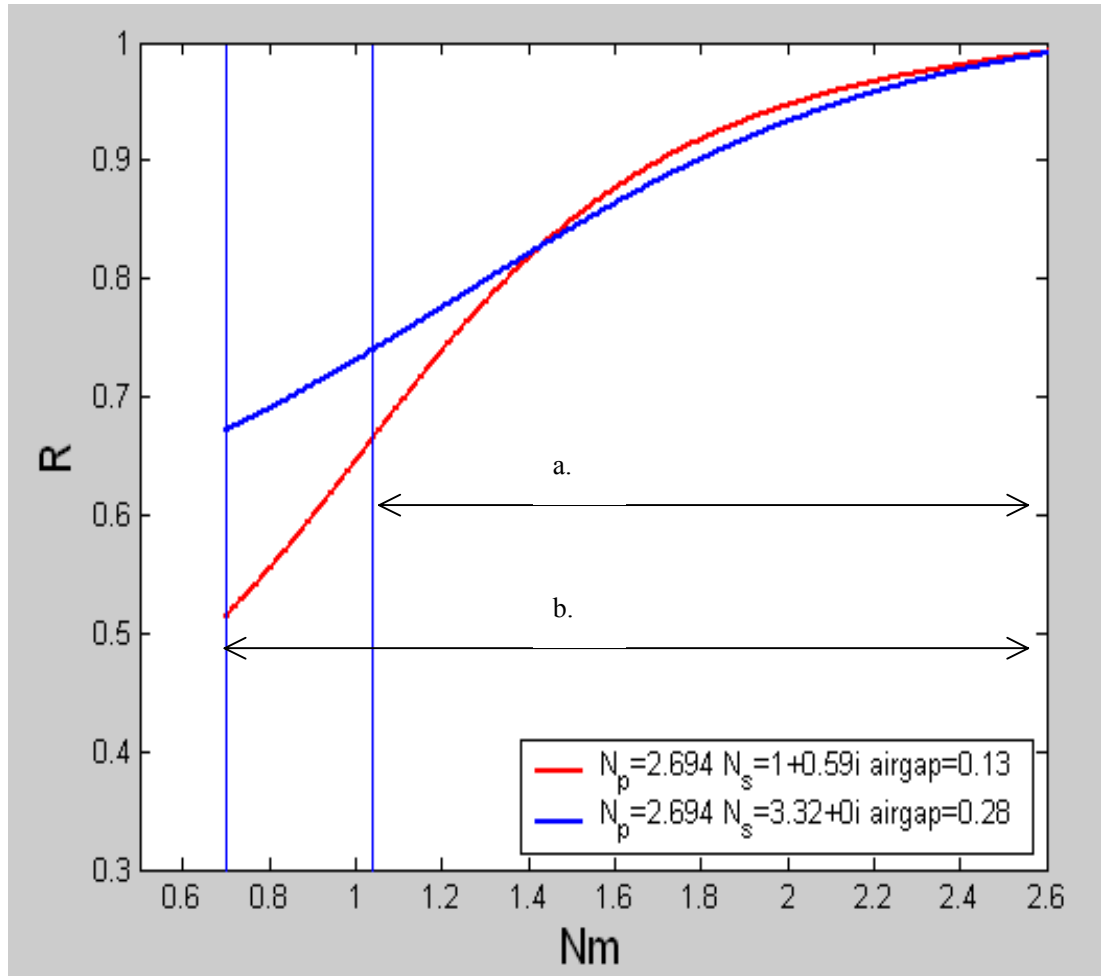
### 12.3.1 The Big-Area Method Model

When the hemi-cylindrical prism is used, the measurement stops at the position of total reflection of the air measurement. This part of the total reflection curve is used to normalize the sample intensity curve by Equation III-17<sup>8, 51, 53</sup>.

$$R = \frac{I_{R, \text{sample}} / I_{O, \text{sample}}^r}{I_{R, \text{air}} / I_{O, \text{air}}^r} \quad \text{Eq. III-17}$$

where the subscript  $R$  and  $O$  indicate the reflected and incident laser beams, respectively; the subscript *sample* and *air* are the measurement of the sample and air, respectively; the superscript  $r$  means the reflected beam of the incident light from the beam splitter.

The reflectance curve is finally used to fit the IRIA model. In some cases, especially for highly optical absorbing samples, the fitted results of the experimental curves don't make sense. However, it is also found that such a curve is very close to the curve with the actual value of the sample at the experimental table position region. In Figure XII-5, a Poly-3,4-Ethylenedioxythiophene (PEDOT) film is used as an example to show this kind of phenomenon. The red curve is calculated with reference values ( $n^*=1+0.59i$ ) and the blue line is the fitted curve by the IRIA measurement ( $n^*=3.32+0i$ ). The region “a” is the conventional IRIA measurement region. In this region these two curves are very close to each other. Since the experimental uncertainties (both relative and absolute errors) included in the measurement data and the degree of freedom of the fitting model is high, the fitted results yield the wrong trend (blue curve).



**Figure XII-5** The PEDOT IRIA fitted curve (blue) and IRIA modeling calculated curve with reference complex refractive index value.

On the other hand, it is also noticed that if the measurement region can be extended to region “b”, these two curves show a big difference. Therefore, one of the ways to improve the accuracy is to enlarge the experimental region. The upper limit of the table position already reached the highest value at the edge of the prism. So the only way is to exceed the lower limit which was the table position of the total reflection of air measurement.

This method is simply achieved by using the theoretical reflectance of the air to normalize the whole curve of the air, not only the totally reflecting region but also the transmission region. So:

$$R = \frac{I_{R,\text{sample}} / I_{O,\text{sample}}^r}{I_{R,\text{air}} / I_{O,\text{air}}^r} \times R_a \quad \text{Eq. XII-4}$$

where  $R_a$  is the reflectance of air.

In Equation XII-4, when the measurement region is only the total reflected region,  $R_a = 1$ , so the equation yields the conventional IRIA method (Equation III-17). But in the transmission region, the  $R_a$  will be used to normalize the air intensity ratio as reference 1, so that the whole curve can be fitted by the IRIA model.

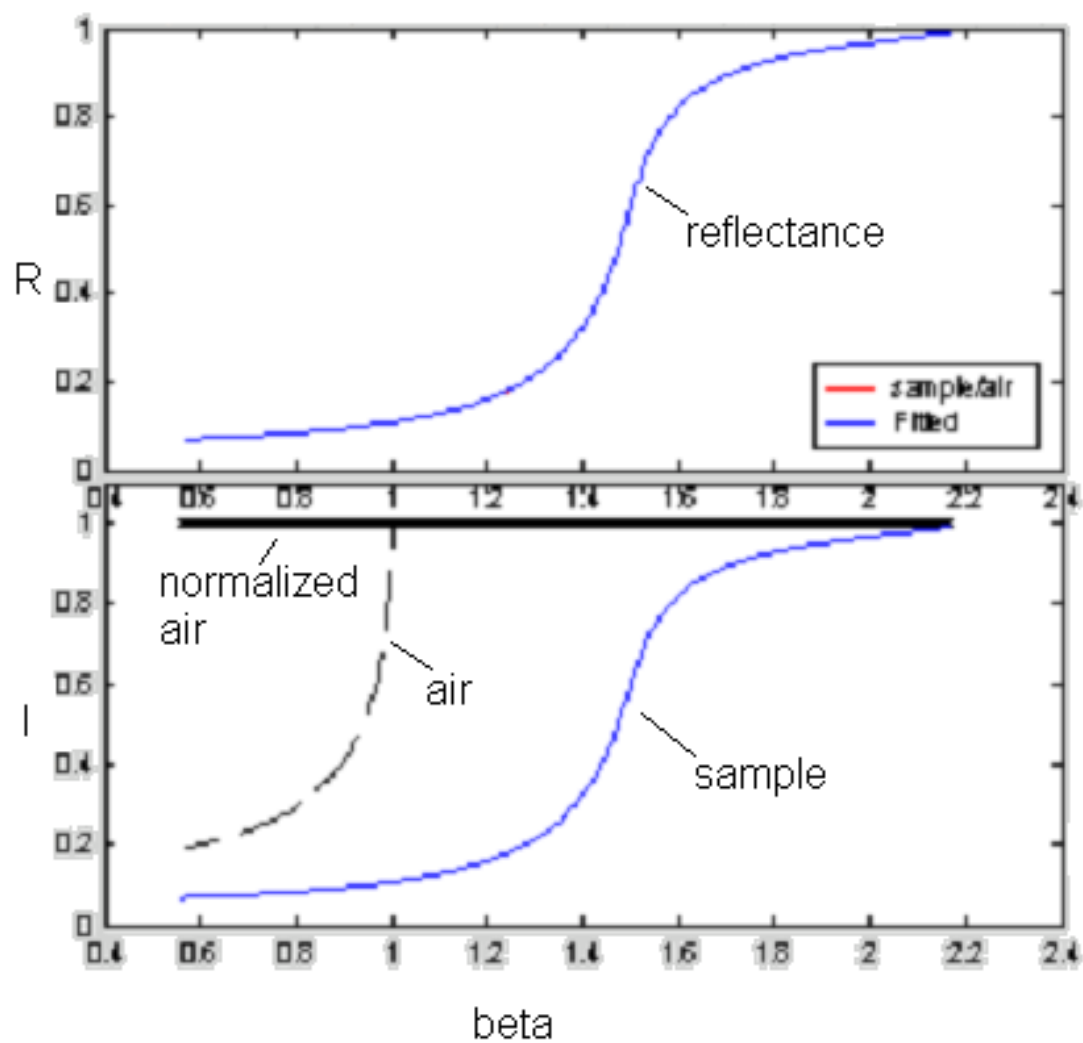
The procedure of the Big-Area method is

- a) Measure the curve of intensity changing with incident angle of both the sample and air over a large angular region, respectively;
- b) Calculate the theoretical reflectance of air,  $R_a$ , at the given wavelength ( by function “Reflect3\_TE.m” for TE and “Reflect3\_TM.m” for TM in the IRIA software package; see the code in ref. 51);
- c) Use the  $R_a$  to normalize the air intensity curve, and use this normalized curve

as the air curve;

- d) The sample reflectance is calculated by dividing sample intensities to the normalized air intensities.
- e) Fit the sample reflectance by the IRIA model.

This process is very similar with the conventional IRIA method. There is also no change on the core calculation part. Figure XII-6 is a modeling calculation of the Big-Area method. The model is setup as: the refractive index of sample is 1.5; the extinction coefficient of sample is 0.05; airgap = 0.02 micron; wavelength = 543 nm; refractive index of prism = 2.184; polarization = TE. The dashed line in the figure is the simulation of air intensity changing with angle and the dark solid line is the normalized air curve. The fitting results are  $n=1.50000$ ,  $k=0.04999$  and  $\text{airgap}=0.01999$ , which match the model very well.



**Figure XII-6.** Modeling test of the Big-Area Method

### 12.3.2 Experimental Results and Discussions

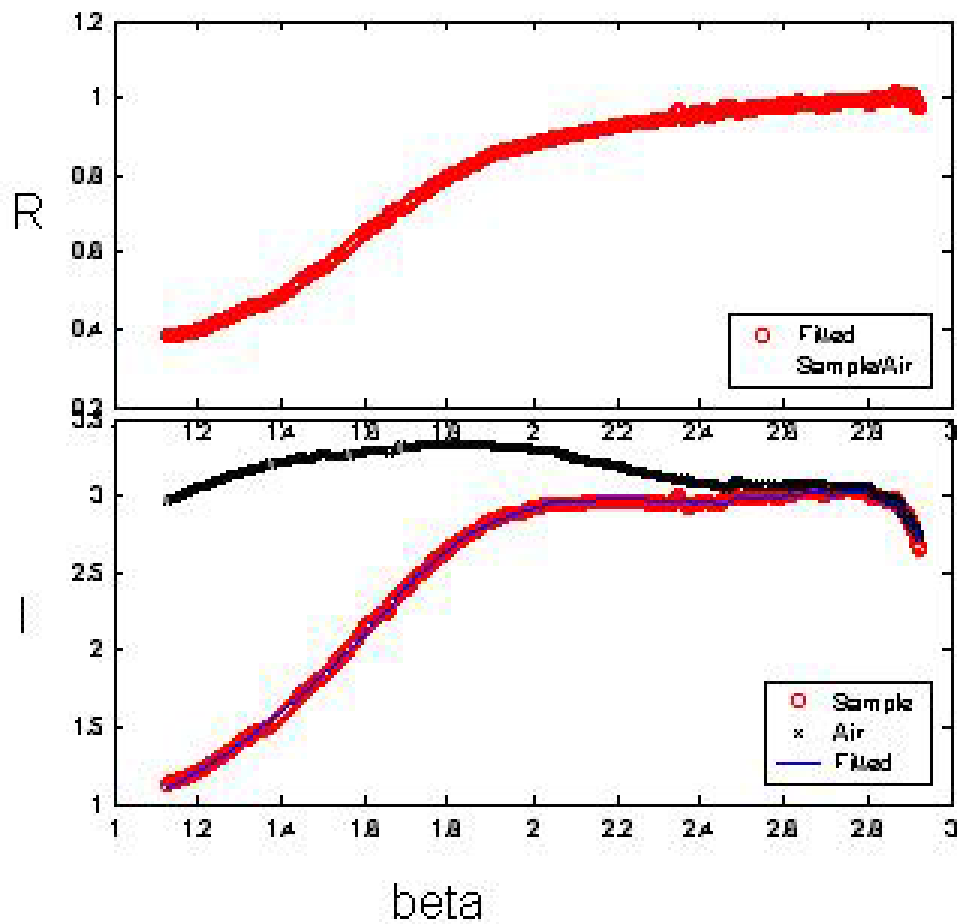
Figure XII-7 is an example of the Big-Area Method measurement. The sample is poly-acrylonitrile - single wall carbon nanotube (PAN-SWNT) (60/40) cast film. Figure XII-7 (a) and (b) used the same set of data. However, in Figure XII-7 (a), the curve is cut short for the total reflection region only, so it is the conventional IRIA method. Both curves fit the IRIA model very well and the fitted results are compared at Table XII- 3. The results show that the Big- Area method is correct and easy to use. There is a “hump” around the  $\beta=1$ . This is because the knee of the experimental air curve is not as sharp as the theoretical reflectance curve. Once the experimental curve is normalized by the theoretical curve, the “hump” is shown. But this “hump” has little effect on the fitting.

### 12.3.3 Limitation of the Big-Area Method

Though the initial target of this method is to measure some high extinction coefficient samples which are difficult for the conventional IRIA method, in the real experiment, it was found that the big-area method still had some problems for highly absorbing samples: Once the measurement region is enlarged, the true curve might be close to another unreasonable curve (similar to Figure XII-15). Therefore, this method didn't really solve the problem of highly absorbing samples.

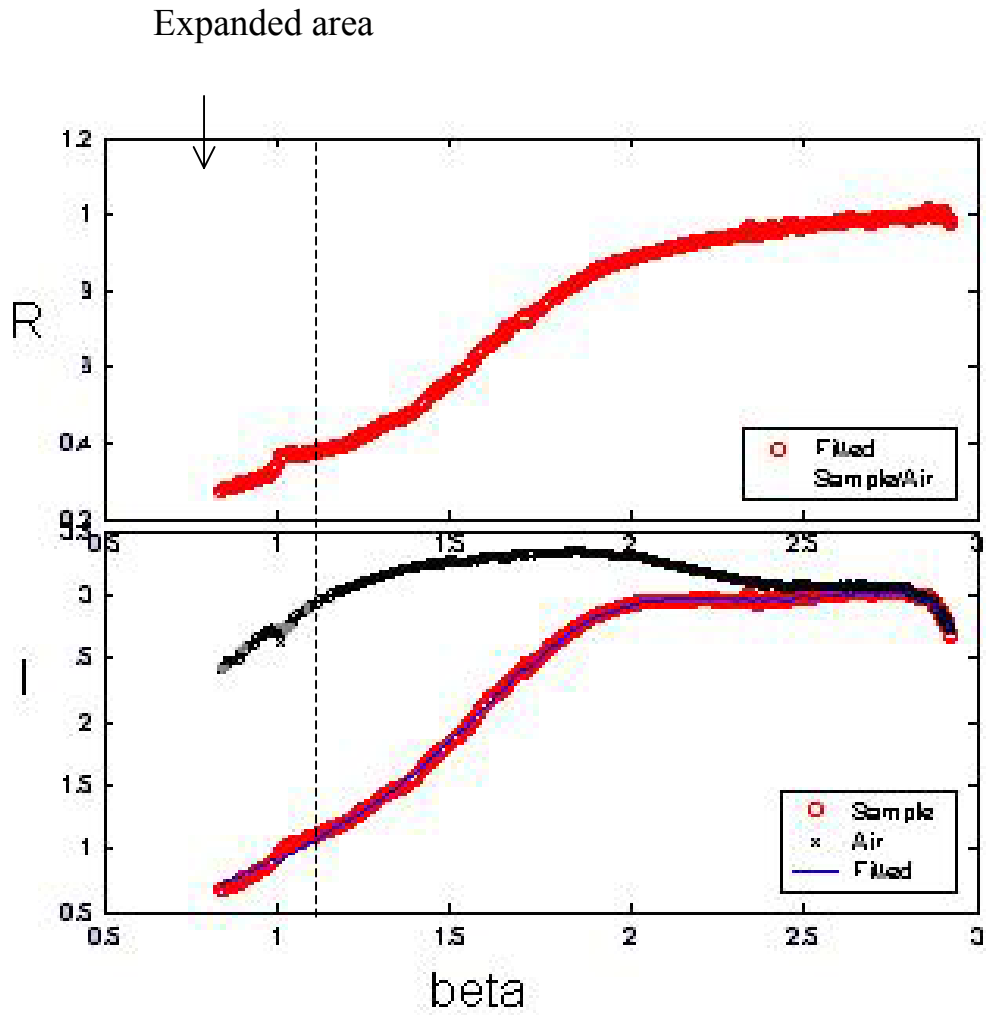
However, it is a good way to improve the accuracy of the IRIA method of regular samples.





a. conventional IRIA method

**Figure XII-7** The fitted curves of PAN-SWNT (60/40) cast film by conventional and Big-Area IRIA methods.(a. conventional IRIA method; b. Big-Area method)



b. Big-Area IRIA

**Figure XII-7** (cont'd) The fitted curves of PAN-SWNT (60/40) cast film by conventional and Big-Area IRIA methods. (a. conventional IRIA method; b. Big-Area method)

**Table XII-3** The fitted results of PAN-SWNT (60/40) cast film by conventional and Big-Area IRIA methods

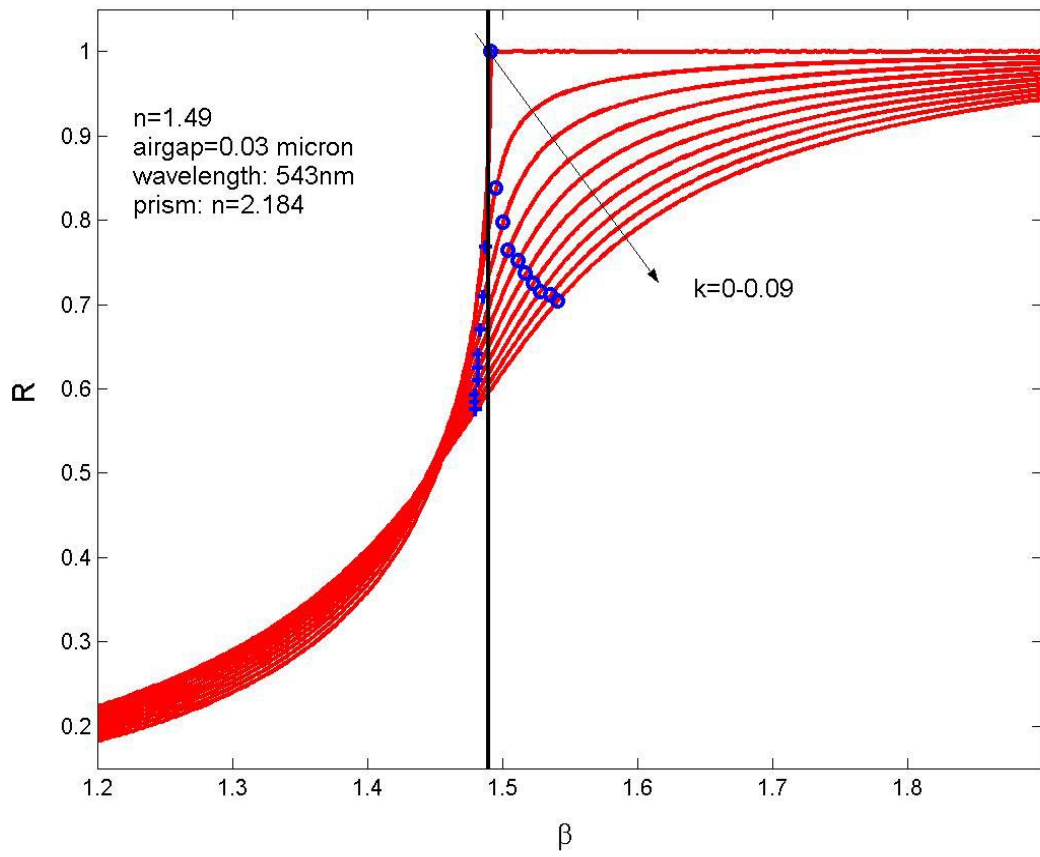
Method	n	k	airgap
IRIA	1.6648	0.274	0.0387
Big -Area	1.6646	0.276	0.0387

## 12.4 THE MODIFIED KNEE METHOD

### 12.4.1 The Modified Knee Method Modeling Calculation

The concept of the knee method is very simple. The critical angle is defined at the sharpest drop of the intensity (the 1st order differential intensity) of the reflected beam<sup>140</sup>. However, this method is only good for transparent samples<sup>141,142</sup>. For absorbing samples, the knee can't be found easily. On the other hand, the sharpest drop no longer provides the critical angle position. For example, a set of modeling calculations is shown in Figure XII-8. The model is:  $n = 1.49$ ,  $k$  has various values,  $\text{airgap} = 0.03\text{micron}$ ,  $\text{wavelength} = 543\text{nm}$ ,  $\text{polarization} = \text{TE}$ ,  $\text{refractive index of the prism} = 2.184$  (Prism 6614). In Figure XII-8, the crosses label the position of the sharpest drops (knees). The vertical line refers to the actual value of the refractive index. It shows that at the high extinction coefficient, the error is large for the conventional knee method.

In the updated Metricon software, there is also another way to calculate the knee position, which called the “intersecting line method”. In this method, the user chooses two points on the intensity pattern to the left of the knee which are used to define the nearly horizontal intensity pattern slope before the knee. Then the user chooses two more points to the right of the knee which are used to define a straight line approximation to the intensity pattern slope after the knee. After the four points are chosen, the intersection point for the two lines is calculated automatically and the index displayed<sup>146</sup>. However, in Figure XII-8 the arrow indicates the position of the refractive index from this method, which is even worse than the knee method<sup>147, 148</sup>.



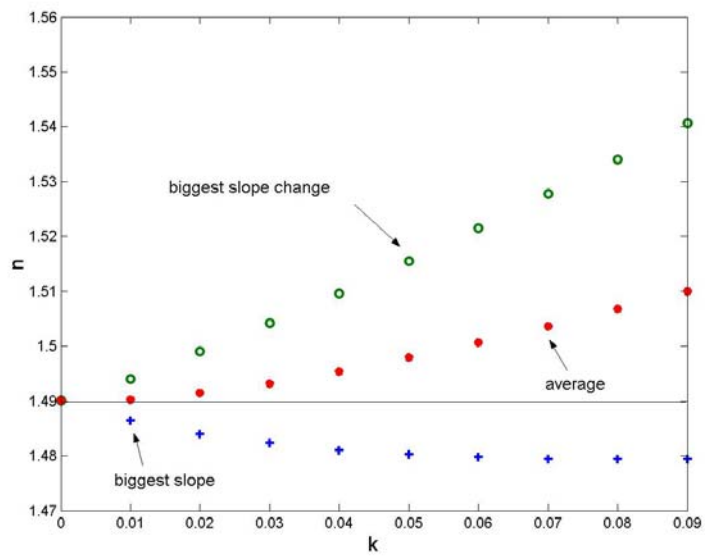
**Figure XII-8.** The modeling calculation of the knee positions and biggest slope change positions with different extinction coefficients

In the meantime, the biggest slope change (the 2<sup>nd</sup> order differential intensity) of the curve is also calculated, and labeled as “o” in Figure XII-8. It was found that the biggest slope position is worse than the knee method. However it was noticed that the directions of departure of the biggest drop (knee method) and the biggest slope change to the critical angle position are opposite to each other. So the average position of the sharpest drop and the biggest slope change was calculated and tried to minimize the error of knee method.

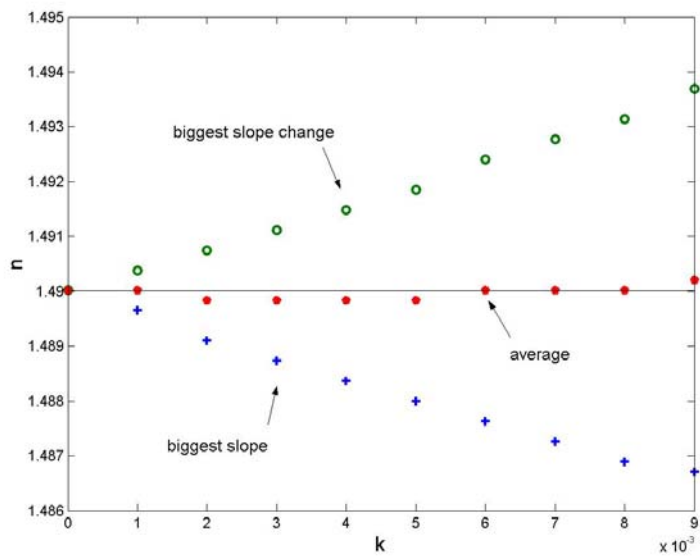
It was found numerically that when the extinction coefficient is less than 0.01, the average  $\beta$  value of the position of the sharpest drop and the biggest slope change is very close to the actual refractive index [Figure XII-9 (a) (b)]. A low and a high refractive index values, 1.2 and 1.8, respectively, were also used to test this TE measurement. Both of them work very well [Figure XII-9(c) and (d)].

However, the TM measurement is different. For a moderate refractive index, like 1.49, it works well [Figure XII-10 (a)]. For high and low refractive indices, it's not perfect, but the error is less than either of the sharpest drop (knee) or the biggest slope change method [Figure XII-10 (b) and (c)]. The absolutely error is less than 0.002 which is smaller than the IRIA method.

This method was also tested for different airgaps and different shapes of the prism. These two factors have little effect on the results.

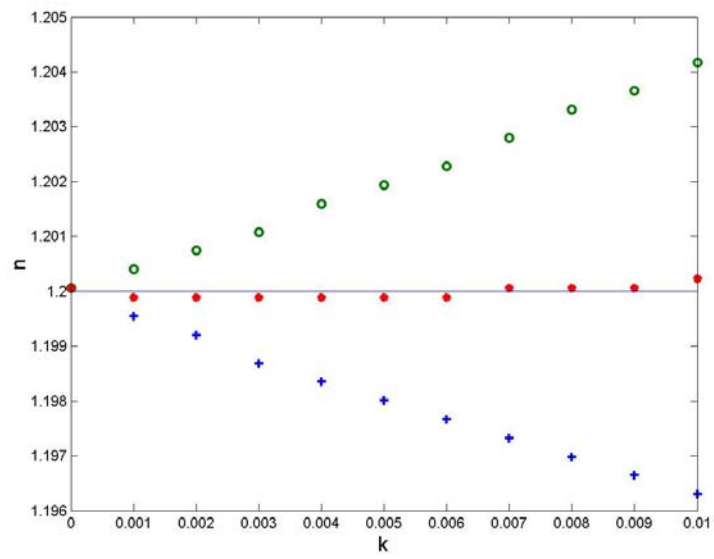


a.  $n=1.49$ ,  $k=0-0.09$ , TE

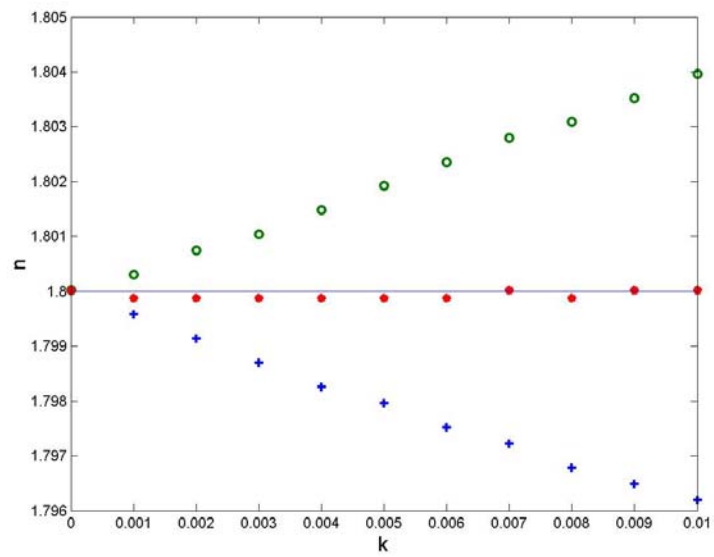


b.  $n=1.49$ ,  $k=0-0.01$ , TE

**Figure XII-9.** The TE modeling calculation of the modified knee method

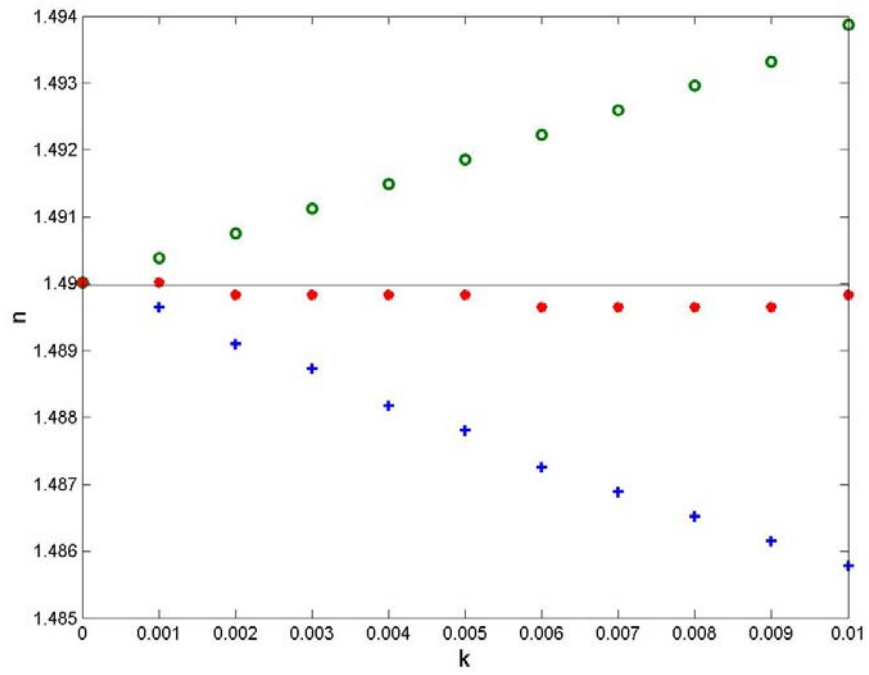


c.  $n=1.2$ ,  $k=0-0.01$ , TE

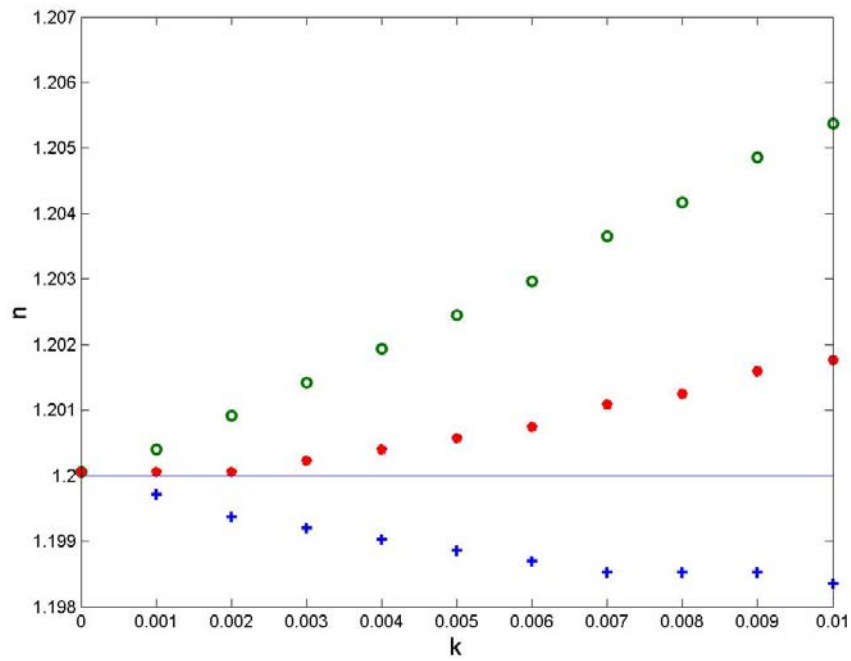


d.  $n=1.8$ ,  $k=0-0.01$ , TE

**Figure XII-9 (cont'd).** The TE modeling calculation of the modified knee method



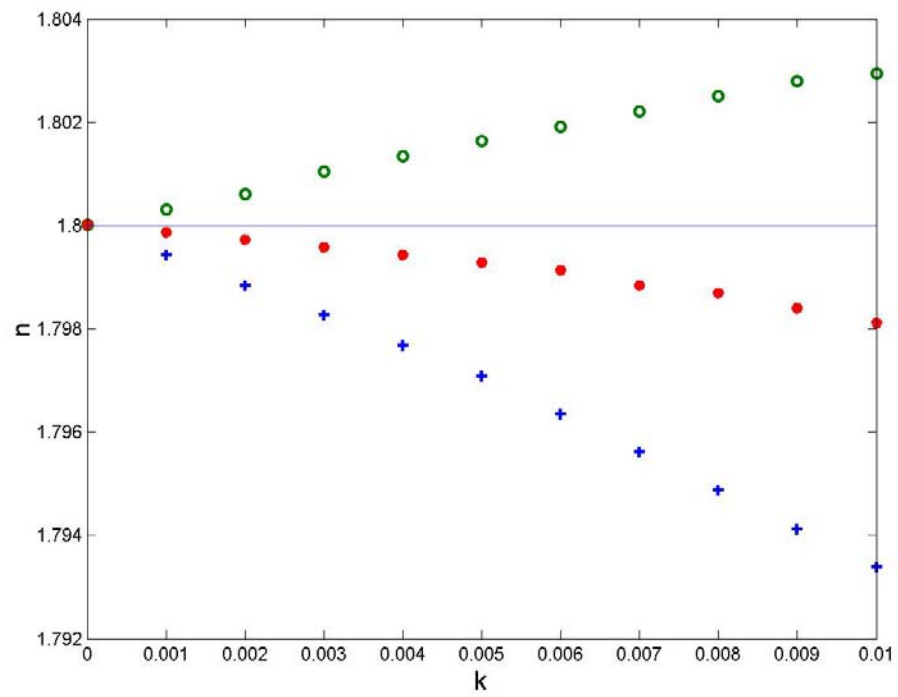
a.  $n=1.49$ ,  $k=0-0.01$ , TM



b.  $n=1.2$ ,  $k=0-0.01$ , TM

**Figure XII-10.** The TM modeling calculation of the modified knee method





c.  $n=1.8$ ,  $k=0-0.01$ , TM

**Figure XII-10 (cont'd).** The TM modeling calculation of the modified knee method

So this method is a very convenient way to get high accuracy refractive index values of moderately absorbing samples. The results can be directly used to discuss the axially, crystallinity and orientation, etc. The other advantage of this method is that it is not sensitive to long-term laser drift, which is a significant problem for IRIA. On the other hand, once the refractive index can be obtained from the modified knee method, the value can be substituted into the IRIA fitting model to decrease the degree of freedom. If this kind of method is combined with the two-line method, the accuracy of  $k$  is expected to increase.

#### 12.4.2 Experimental Results and Discussions

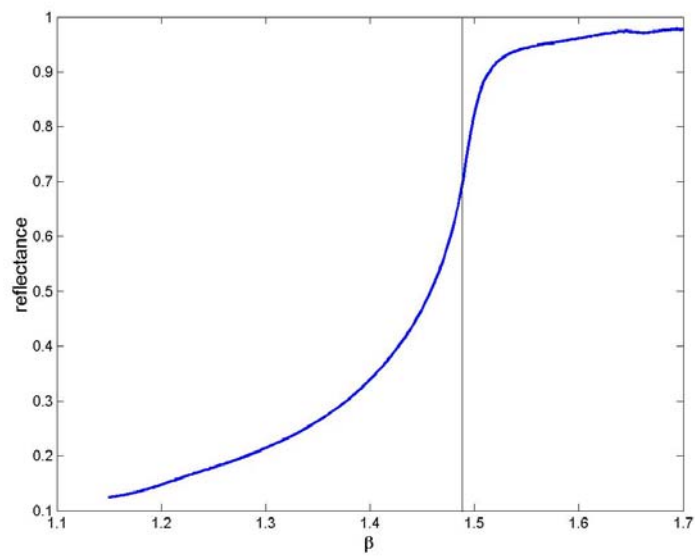
The extinction coefficient of the IPP-CB samples is about 0.006, 0.012 for the 1% CB and 2% CB, respectively. So it is a good example to test the Modified Knee Method.

In Figure XII-11, IPP-2% CB unstretched sample was used as an example of calculation by the modified knee method. Figure XII-11 (a) and (b) show how the slope and the differential slope changes with  $\beta$ , respectively. These data are exactly what was used in the IRIA fitting, so the resolution is 10 steps/point ( $0.15^\circ/\text{point}$ ).

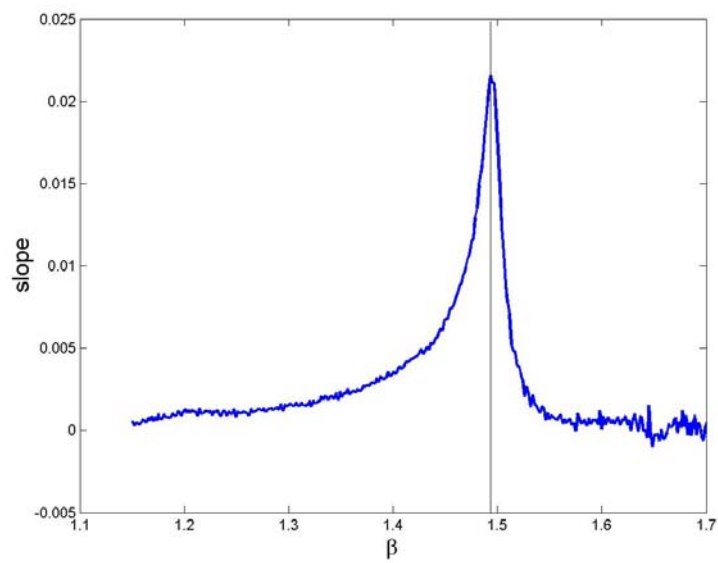
In Table XII-4, the results by the different methods are compared. Though the exact actual values of the refractive indices of these samples are unknown, it shows that the modified knee method results are in the right region. On the other hand, the accuracy is also limited by the resolution of the IRIA method which is  $0.15^\circ/\text{point}$ . If the intensity was recorded by  $0.015^\circ/\text{point}$ , the modified knee method would be a very easy way to get high accurate refractive index values from samples with moderate  $k$ .

**Table XII-4** the refractive indices of unstretched IPP-CB samples by different methods

[CB]	Polarization	Knee	Diff. slope	IRIA	Modified knee
2.5%	TE	1.4933	1.4952	1.4935	1.4933
	TM	1.4933	1.4952	1.4957	1.4933
5%	TE	1.4933	1.4988	1.4939	1.4952
	TM	1.4970	1.5025	1.4987	1.4988

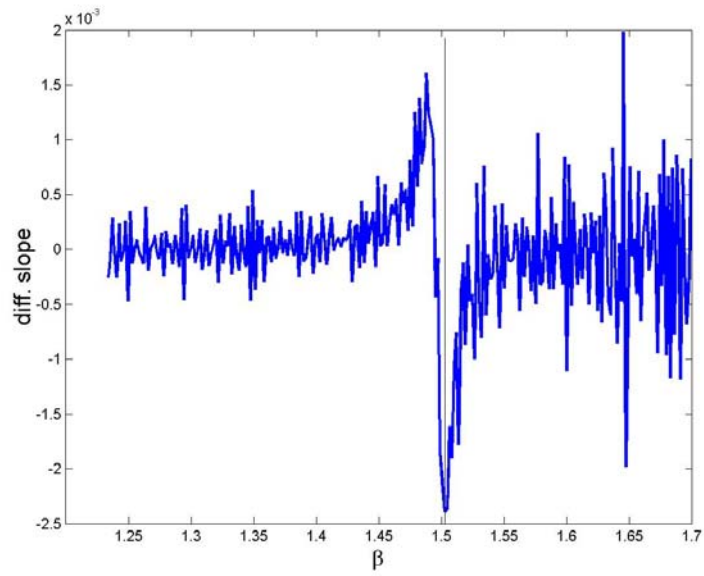


a. reflectance vs.  $\beta$



b. Slope vs.  $\beta$

**Figure XII-11** The intensity, slope and differential slope changing with  $\beta$  of IPP-2% CB TE intensity



c. Differential slope vs.  $\beta$

**Figure XII-11 (cont'd)** the intensity, slope and differential slope changes with  $\beta$  of IPP-2% CB TE intensity

### 12.4.3 The Limitation and Expectation of the Modified Knee Method

This method is limited by the quality of the equipment. In order to use this method, the value of the slope and the differential slope need to be very accurate. So the intensity of the laser must be stable during the measurement and the experimental step needs to be small. Therefore, it needs a stable laser and high-resolution detectors. This may be overcome by smoothing the curve.

Since the modified knee method prefers a high-resolution rotating table, a large memory multimeter is needed to record more intensity data than IRIA. The current IRIA system looks OK for  $0.15^\circ$  /point resolution, but may not be good for higher resolution, like  $0.015^\circ$  /point. So the more sophisticated instruments, such as detectors and multimeters, may be necessary for this method to obtain better accuracy for absorbing samples. With the development of new instruments, the prices of such equipments could be decreased and because of the simple calculation and setup, the modified knee system could be very easy to be integrated, so it will be a very promising way to get refractive index information quickly and accurately.

## 12.5 FUTURE MAP

The methods proposed above can be integrated together to improve the waveguide methods. The future map is shown in Figure XII-12.

The modified knee method can give very accurate refractive index values. From the refractive index, the axiality, crystallinity, birefringence and orientation (single phase system) can be known (see 3.2.1.1.2). If the refractive index result is substituted in the Big Area method, and the Two-Line method is used to eliminate the effect of the airgap, a very accurate result on the extinction coefficient will be obtained. At the same time, the fitted refractive index can be fed back into the modified knee method. Then continue iterating with both values, until constant  $n$  and  $k$  are obtained. This way more information, such as optical polarizability ( $2nk$ ) and conductivity ( $n^2+k^2$ ), may be able to be evaluated. Finally, the bootstrap method can give the experimental uncertainty. So there is a bright future for the waveguide methods.

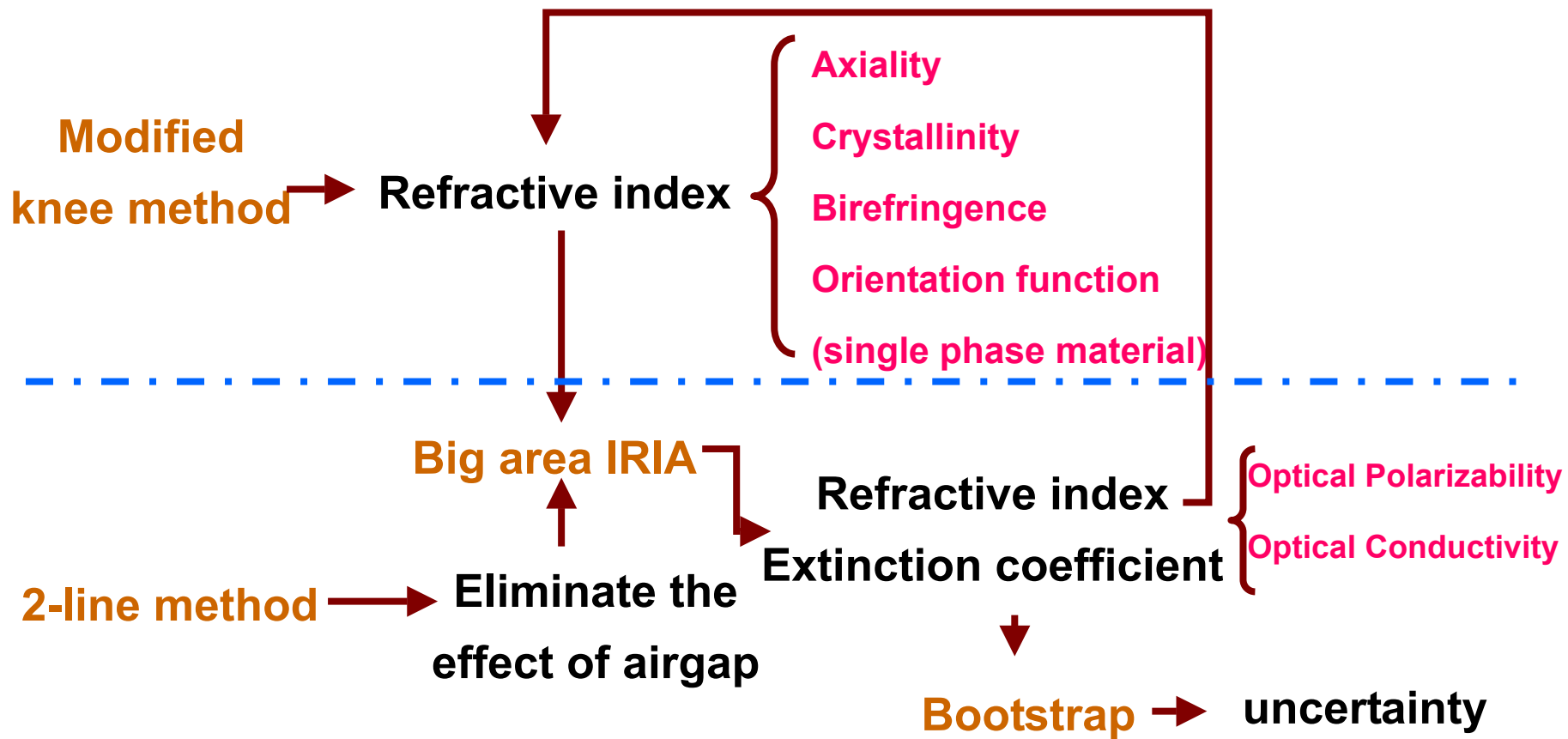


Figure XII-12 Future map of the IRIA method



## CHAPTER XIII

### OVERALL CONCLUSIONS

This present research has developed methods for measuring the optical characteristics of nanoparticle filled heterogeneous polymer systems. Isotactic polypropylene with nano carbon black (IPP-CB) films and poly (methylmethacrylate) mixed with nano size indium tin oxide (PMMA-ITO) composites have been studied as the model uniformly distributed and nonuniformly distributed systems, respectively. Further, several ways to improve the current waveguide methods were introduced.

#### Uniformly distributed nano composite model —IPP-CB

IPP-CB is an oriented uniformly distributed system. This system is also a multiphase and optical absorbing system. These are the main challenges for the optical characterization of the IPP-CB system. In order to overcome these problems, three nondestructive optical techniques: waveguide coupler, FTIR and x-ray diffraction were used to investigate the effect of carbon black on the orientation, the crystallinity and the crystal form of IPP. It was found that, the carbon black has a significant effect on the IPP orientation behavior, but little effect on the crystallinity and the crystal form of IPP. The multilevel structural characterization procedure developed in this study can lead to new fundamental nano-particle composite process-structure information and improved fabrication procedures.

### Nonuniformly distributed nano composite model —PMMA-ITO

PMMA-ITO composite is an unoriented nonuniformly distributed system. A grain structure was found by optical and electron microscopies. This structure limits the application of the conventional IRIA method. Therefore a unique break point method was developed for the waveguide to study the refractive index and the extinction coefficient from grain structures. It was found that both the refractive index and the extinction coefficient of the PMMA-ITO composites increase with ITO concentration.

### System operation improvement

Finally, several improvements in the system operations on waveguide methods were developed including: the Bootstrap method which can be used to estimate the experimental uncertainty; the Two-Line method can effectively eliminate the affect of the airgap in IRIA fitting; the Big-Area method can improve the accuracy of the fitted results by enlarging the measurement angular region; and the Modified Knee method can be used to obtain the refractive index of a moderately optical absorbing sample. Lastly, by combining these four methods, the accuracy of the waveguide measurements is expected to have a significant improvement.

Overall, this research overcame many difficulties on optical characterization of the complicated nano-particle filled polymer systems and developed several methods to improve the new IRIA technique. It has filled a blank in the field of the nondestructive structure characterization of heterogeneous polymer systems.

## REFERENCES

1. S. K. Bhattacharya, A. C. D. Chaklader, Polym. Plast. Technol. Eng., 19 (1), 21, 1982
2. E. K. Sichel, Carbon Black- Polymer Composites, The Physics of Electrically Conducting Composites, Marcel Dekker, Inc, 1982, New York
3. R. Strumpler, J. Glatz-Reichenbach, Journal of Electroceramics, 3 (4), 329, 1999
4. A. R. Horrocks, J. Mwila, M. MirafTAB, J Mater Sci 34 (17), 4333 1999
5. A. Y. Malkin, Advances in Polymer Science, 96, 69, 1990
6. S. Ramakrishna, J. Mayer, E. Wintermantel, K. W. Leong, Composites Science And Technology 61 (9), 1189, 2001
7. R. J. Morgan, E. E. Shin, J. Lincoln, J. Zhou, Sampe Journal 37 (2), 102, 2001
8. T. Liu, R. J. Samuels, J. Polymer Science, Part B: Polymer Physics, 39, 2481, 2001
9. J.-C. Huang, Advances on Polymer Technology, 21 (4), 299, 2002
10. R. Tchoudakov, O. Breuer, M. Narkis, A. Siegmman, Polymer Engineering and Science, 36, 1336, 1996
11. R. Tchoudakov, O. Breuer, M. Narkis, A. Siegmman, Polymer Networks Blends, 6, 1, 1996
12. H. Zois, L. Apekis, M. Omastova, Macromol. Symp. 170, 249, 2001
13. F. Hernandez-Sanchez, P. J. Herrera-Franco, Polymer Bulletin, 45, 509, 2001
14. J. C. Huang, C. L. Wu, S. J. Grossman, Journal of Polymer Engineering, 20(3), 213, 2000
15. J. Koszkuł, Journal Of Polymer Engineering, 18 (4), 249, 1998
16. C. -L. Wu. Doctoral Thesis; Plastics Engineering Department, University Of Massachusetts, Lowell, MA, 1996
17. J. Feng, J. Li, C.-M. Chan, Journal of Applied Polymer Science, 85, 358, 2002

18. J. X. Li, W. L. Cheng *J. Appl Polym Sci*, 72, 1529, 1999
19. J. X. Li, N. J. Ness, W. L. Cheung, *J. Appl. Polym. Sci.*, 59, 1733, 1996
20. B. Wunderlich, *Thermal Analysis*, Academic Press Inc., New York, 1990
21. B. Ke, *Newer Methods of Polymer Characterization*, Wiley Interscience, New York, 1964
22. R. L. Miller, *J. Polym. Sci.* 57, 975, 1962
23. M. Mucha, J. Marszalek, A. Fidrych, *Polymer*, 41, 4137, 2000
24. M. Mucha, Z. Krolkowski, *Journal of Thermal Analysis and Calorimetry*, 74, 549, 2003
25. R. J. Samuels, *J. Polym. Sci.*, 13, 1417, 1975
26. A. R. Bhattacharyya, Et al., *Polymer*, 44, 2373, 2003
27. J. Broda, *Polymer*, 44, 6943, 2003
28. J. Broda, *J. Appl. Polym. Sic.*, 89, 3364, 2003
29. J. Broda, *Polymer*, 44, 1619-1629, 2003
30. P. H. Hermans, *Contributions to The Physics of Cellulose Fibers*, Elsevier Science Publishing Co., Inc., New York, 1946
31. R. J. Samuels, *Structured Polymer Properties*, John Wiley & Sons, New York, 1974
32. M. Born, E. Wolf, *Principals of Optics* 6th Ed., Oxford: Pergamon, 1980
33. E. Hecht, *Optics*, 3rd Edition, Addison-Wesley Longman, Inc, 1998
34. K. J. Botton, *Infrared and Millimeter Waves*, Vol. 13, Academic Press, Inc. 1985
35. M. R. Bockstaller, E. L. Thomas, *J. Phys. Chem. B*, 107, 10017, 2003
36. R. Simon, P. Ulrich, *Colloid Polymer Science*, 277, 2, 1999
37. D. Smith, L. Snow, L. Sibille, E. Lgnont, *J. Non-Cryst. Solids*, 285, 256, 2001
38. R. J. Samuels, *J. Polymer Sci.*, A3, 1741, 1965

39. R. J. Samuels, J. Polym. Sci. Polym. Phys. Ed. 12, 1417, 1974
40. R. J. Samuels, J. Polym. Sci. Polym., 26, 1383, 1981
41. R. E. Pepper, M.S. Thesis, Georgia Institute of Technology, Atlanta, Ga., 1986
42. K. C. Smyth, C. R. Shaddix, Combustion and Flame 107, 314, 1996
43. B. J. Stagg, T. T Charalempopoulos, Combustion and Flame, 94, 381, 1993
44. A. Borghesi, G. Guizzetti, Graphite (C), Handbook of Optical Constants of Solids II., 1991
45. Refractive Index And Extinction Coefficient of Materials, Filmetrics Corporation Of San Diego, California, 2002
46. H. Chang, T. T. Charalampopoulos, Proceedings: Mathematical and Physical Sciences, 430(1880), 577, 1990
47. I. Colbeck, E. J. Hardman, et al.. Journal of Aerosol Science 20(7), 765, 1989
48. M. W. Urban, Attenuated Total Reflectance Spectroscopy of Polymers, American Chemical Society, Washington, DC, 1996
49. G. Amdermann, A. Caron, D. Dows, Journal of The Optical Society of America, 55, 1210, 1965
50. Metricon PC-2010 Prism Coupler, Manufacturer's Bulletin, Metricon Corp., Pennington, NJ, 1990
51. T. Liu, Ph.D. Thesis, Georgia Institute of Technology, Atlanta, Ga., 2001
52. J. D. Jackson, Classical Electrodynamics, 3rd Edition, John Wiley & Sons, New York, 1998
53. T. Liu; R. J. Samuels, Journal of Polymer Science Part B: Polymer Physics, 2003,41,842-855, 2003
54. R. J. Samuels, Refractometry, Encyclopedia of Polymer Science and Engineering, Volume 14, Second Edition, John Wiley & Sons, 1988
55. C. Cha, R. J. Samuels, J. Polym. Sci, Part B, 33, 259, 1995
56. B. L. Van Horn, H. Henning Winter, Macromolecules, 36, 8513, 2003
57. A. A. Hamza, T. Z. N. Sokkar, K. A. El-Farahaty, H. M. El-Dessouky, Polymer Testing, 23, 203, 2004

58. P. Yeh, *Optical Waves in Layered Media*, Wiley, New York, 1988
59. R. M. A. Azzam, N. M. Bashara, *Ellipsometry and Polarized Light*, North-Holland Publishing Company, 1977
60. G. Jungk, *Thin Solid Films*, 234, 428, 1993
61. X. Wu, Master Thesis, Georgia Institute of Technology, Atlanta, Ga., 1987
62. D. C. Postethwait, Master Thesis, Georgia Institute of Technology, Atlanta, Ga., 1984
63. R. J. Samuels, *Die Makromol. Chem. Suppl.* 4, 241, 1981
64. B. Jasse, J. L. Koenig, *J. Macromol. Sci.-Rev. Macromol. Chem. C* 17(1), 61, 1979
65. S. Krimm, *Fortschr. Hochpolymer-Forsch.*, 2, 51, 1960
66. J. E. Huber, Master Thesis, Georgia Institute of Technology, Atlanta, Ga., 1981
67. R. J. Samuels, *J. Polymer Sci.*, A3, 1741, 1965
68. K. Abe, K. Kanagisawa, *Journal of Polymer Science*, 36 (130), 536, 1959
69. J. P. Loungo, *Journal of Applied Polymer Science*, 3 (9), 302, 1960
70. W. Heinen, *Journal of Polymer Science*, 18, 545, 1959
71. R. G. Quynn, J. L. Riley, D. A. Young, H. D. Noether, *Journal of Applied Polymer Science*, 2, 166, 1959
72. G. Natta, *J. Polymer Sci*, 16, 143, 1955
73. F. Rodriguez, *Principals of Polymer Systems*, McGraw-Hill Book Company, 1970
74. Y. Song, K. Nitta, N. Nemoto, *Macromolecules*, 36, 8066, 2003
75. R. D. B. Fraser, In *Analytical Methods of Protein Chemistry*, Vol. 2, P. Alexander And R. J. Block, Eds., Pergamon, New York, 1960, Chap. 9.
76. R. E. Pepper, Ph.D Thesis, Georgia Institute of Technology, Atlanta, Ga.1993
77. F. M. Mirabella., Jr. *J. Polym. Sci. Part A-2*, 22, 1293, 1984
78. R. E. Pepper, R. J. Samuels, *Polymer Characterization*, C.D. Craver and T.

- Provder Eds., ACS Publishers, Washington, D. C., Chapter 18, 1990
79. K. Kirov, H. Assender, *Macromolecules*, 37, 894, 2004
  80. N. Everall, D. Mackerron, D. Winter, *Polymer*, 43, 4217, 2002
  81. K.-J. Eichhorn, I. Hopfe, P. Pötschke, P Schmidt, *Journal of Applied Polymer Science*, 75, 1194, 2000
  82. A. L. Smith, *Applied Infrared Spectroscopy*, John Wiley & Sons, New York, 1979
  83. FTIR Instruction Set, No. 269-706800, Nicolet Corporation, Madison, WI.
  84. H. P. Klug, L. E. Alexander, *X-Ray Diffraction Procedures*, Wiley, New York, 1954
  85. P. H. Geil, *Polymer Single Crystal*, John Wiley & Sons, Inc. 1963
  86. G. Natta, P. Corradini, M. Cesari, *Atti Accad. Naz. Lincei*, 21, 365, 1956
  87. G. Natta and P. Corradini, *Nuovo Cimento*, 15, Suppl. 1, 40, 1960
  88. R. L. Miller, unpublished results
  89. Z. W. Wilchinsky, *J. Appl. Phys.*, 3, 1969, 1960
  90. Z. Mencik, *Chem. Prumysl.* 10, 377, 1960
  91. R. J. Samuels, *Class Notes of Process-Property Control Though Structure*, 1986
  92. H. Sobue, Y. Tabata, *Journal of Polymer Science*, 39, 427, 1959
  93. Y. Miyamoto, K. Fukao, T. Yoshida, N. Tsurutani, H. Miyaji, *Journal of The Physical Society Of Japan*, 69 (6), 1735, 2000
  94. L. E. Alexander, *X-Ray Diffraction Methods in Polymer Science*, John Wiley & Sons, New York, 1969
  95. M. Polanyi, *Z. Physik*, 7, 149, 1921
  96. Z. W. Wilchinsky, *J. Appl. Phys.*, 30, 792, 1959
  97. R. J. Samuels, *Norelco Reporter*, 10, 101, 1963
  98. C. J. Capozzi, S. Shackelford, R. Ou, R. A. Gerhardt, *Mat. Res. Symp. Proc.*

848, in press, 2004

99. H. Miyazaki, T. Ota, I. Yasui, *Solar Energy Materials & Solar Cells* 79, 51, 2003
100. A. Malliaris, D. T. Turner, *Journal of Applied Physics*, 42 (2), 614, 1971
101. J. W. Cahn, *J. Chem. Phys.* 42, 93, 1965
102. M. A. Knackstedt, A. P. Roberts, *Macromolecules*, 29, 1369, 1996
103. J. E. Mark *Polymer Data Handbook*, Oxford University Press 1999
104. L. F. Thompson, C. G. Willson, J. M. J. Frechet., Eds. *Materials for Microlithography: Radiation-Sensitive Polymers*. American Chemical Society, Washington, D.C., vol. 266, 1984
105. M. S., Htooed. *Microelectronic Polymers*. Marcel Dekker, New York, 1989.
106. F. W. J. Billmeyer, *Textbook of Polymer Science*. John Wiley and Sons, New York, 1984
107. <http://www.atofinchemicals.com/atoglas/pdfs/atg-5>
108. J. C. Salamone, Ed. *Polymeric Materials Encyclopedia*. CRC Press, New York, 1996.
109. W. Wunderlich, Ed. *Physical Constants of Poly(methyl methacrylate)*, 2nd Ed. John Wiley and Sons, New York, 1975.
110. I. D. Nilolov, Christo D. Ivanov, *Applied Optics*, 39(13), 2000
111. [http://www.ocli.com/products/pop\\_tech\\_info\\_articles\\_tribastone.html](http://www.ocli.com/products/pop_tech_info_articles_tribastone.html)
112. <http://optical1.myetang.com/cidian/glass.htm>
113. J. Brandrup, E. H. Immergut, *Polymer Handbook*, 2<sup>nd</sup> Edition, Wiley, New York (1974)
114. M. Ispirian, S. Karabekyan, R. Eckmann, "Measurements of Transmission of Plastic", 1997
115. H. J. Gray, A. Isaacs, *Dictionary of Physics*, Longman, 1991
116. K. L. Chopra, D. K. Pandya, *Thin Solid Films*, 12, 1, 1983
117. M. Clement, J. Santanmaria, E. Iborra, G. Gonzalez-Diaz, *Vacuum*, 3, 447, 1987



118. T. Ninami, MRS Bull. 25(8), 45,2000
119. P. Nath, R.F. Bunshah, B.M. Basol, O.M. Staffsud, Thin Solid Films, 72, 463, 1980
120. I. Hamberg, C. G. Granqvist, J. Appl. Phys, 60, R123, 1986
121. B. Bessais, H. Ezzaouiz, R. Bennaceur, Semicon. Sci. Technol., 8, 1671, 1993
122. C.G. Granqvist, A. Hultaker, Thin Solid Films, 411, 1, 2002
123. S. Laux, N. Kaiser, A. Zoller, R. Gotzelmann, H. Lauth, H. Bernitzki, Thin Solid Films, 335, 1, 1998
124. K. Zhang, A. R. Forouhi, I. Bloomer, J. Vac. Sci. Technol. A 17 (4), 1999
125. H.-N. Cui, V. Teixeira, A. Monteriro, Vacuum, 67, 589, 2002
126. M. Losurdo, M. Giangregorio, et al. J. Vac. Sci. Technol. A 20 (1) 37, 2002
127. K. S. Ramaiah, V. S. Raja, et al. Semicond. Sci. Technol. 15, 676, 2000
128. I. Hamberg, C.G. Granqvist, Sol. Energy Mater. 14, 241, 1986
129. G. Kortum, Reflectance Spectroscopy, Springer-Verlag, NY, 1969
130. D. A. G. Bruggemann, Ann. Phys. (Leipzig) 24, 636, 1965
131. P. Drude, Z. Phys, 1-161, 1900
132. K. S. Ramaiah, V. S. Raja, et al. Semicond. Sci. Technol. 15, 676, 2000
133. C. M. Wolfe, N. Holonyak, G. E. Stillman (ed) Physical Properties of Semiconductors, Prentice-Hall, Eaglewood Cliffs, NJ, 1989
134. B. Efron, R. Tibshirani, An Introduction to the Bootstrap, CHAMPMAN & HALL, 1993
135. A. Davison, D. Hinkley, Bootstrap Methods and their Application, CAMBRIDGE University PRESS, 1997
136. B. Efron, Ann. Statist. 7, 1, 1979
137. MatLab® 6.5 help file
138. H. William, et al.. Numerical Recipes in C, 2nd Edition, CAMBRIDGE University PRESS, p.691,1992

- 139. M. Abramowitz, and I.A. Stegun, Eds. Handbook of Mathematical Functions with Formulas, Graphs, and Mathematical Tables, 9th printing. New York: Dover, p.14, 1972.
- 140. Metricon PC 2010 Instruction, 2003
- 141. G. Meeten, North An, J Phys E Sci. Instrum. 17 (8), 642, 1984
- 142. G. Meeten, Meas. Sci. Technol. 8 (7), 728, 1997